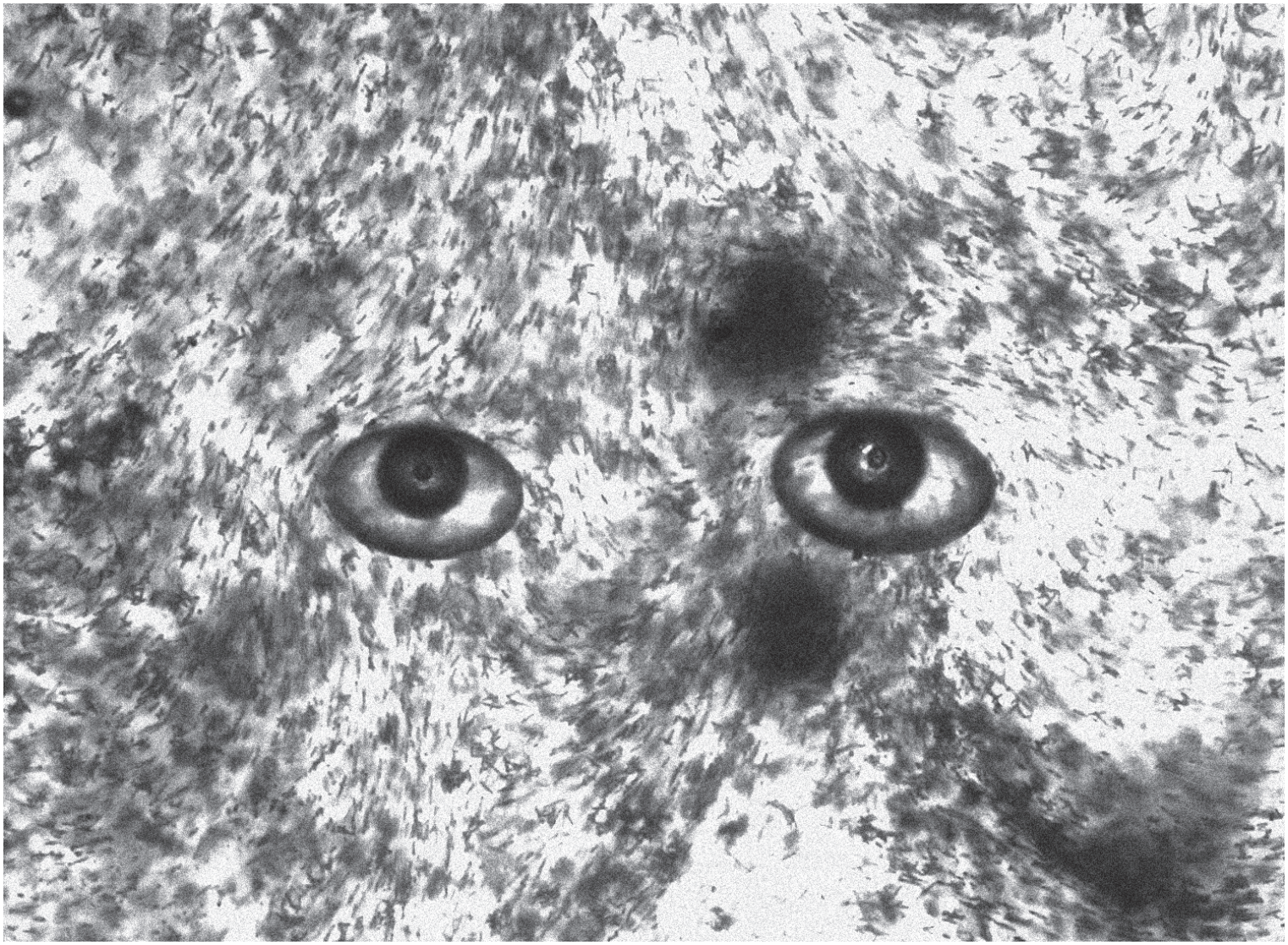

2015 ANNUAL REPORT

HP-HT laboratory

EXPERIMENTAL VOLCANOLOGY AND GEOPHYSICS

laboratory

NEW TECHNOLOGIES

Department of Seismology and Tectonophysics
Istituto Nazionale di Geofisica e Vulcanologia

Via di Vigna Murata 605 | 00143 Roma - Italia | Tel +39-0651860437 | Fax +39-0651860507
www.ingv.it

About the cover
Sulphur rich fluid inclusions with crystals of pure sulphur at the center, within a silicate glass.
Credits: M. Masotta

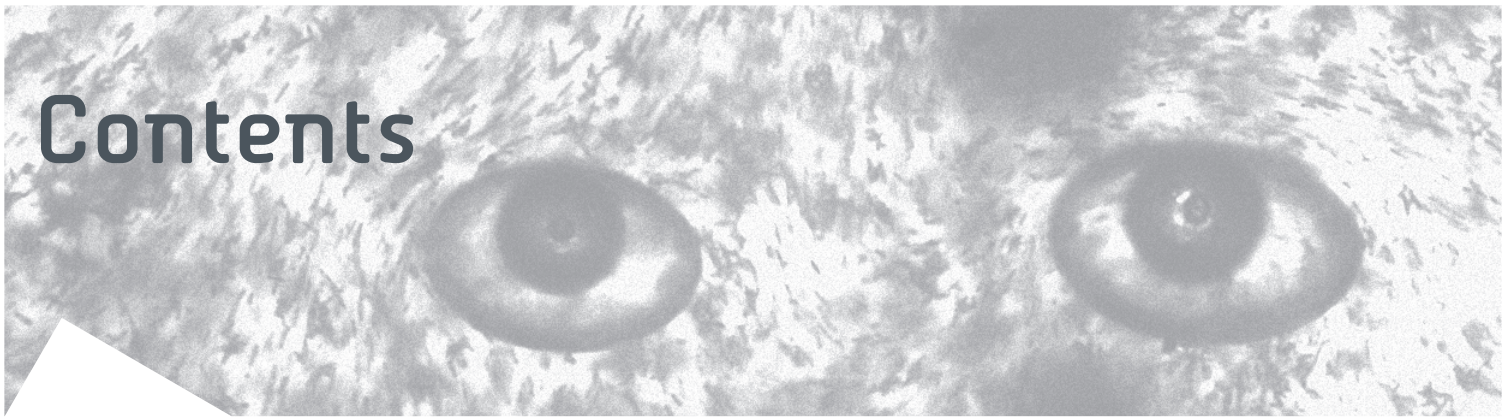

Contents

HP-HT Laboratory of Experimental Volcanology and Geophysics

LNT Laboratory of New Technologies

2015 Annual Report

1| ABSTRACT

This report summarizes the facilities, activities, collaborations, and scientific and technological products of the High Pressure High Temperature Laboratory of Experimental Volcanology and Geophysics and of the Laboratory of New Technologies updated to the year 2015. In this year the lab hosted 26 full-time researchers, 8 associated researchers, 19 PhD/Master students, and 7 visiting scientists. 12 national- to international-level projects were active, and the partner institutions collaborating with the lab personnel amounted to 14.

In 2015 the HPHT Lab continued its activities under ongoing projects, GLASS (InteGrated Laboratories to investigate the mechanics of ASeismic vs. Seismic faulting), NOFEAR (New Outlook on seismic faults: From EARthquake nucleation to arrest) and the VERTIGO (Volcanic ash: fiEld, expeRimenTal and numerIcal investiGations of prOcesses during its lifecycle) in primis. New collaborations opened with USGS for the study of basaltic explosive activity, including 3-D reconstruction of volcanic bomb trajectory. The reviving of the multianvil apparatus started in 2015 and will continue in the next years, together with implementations of the Quickpress piston cylinder apparatus. The BRAVA apparatus is now hosting an improved ultrasonic waves measurement system, and studies on the role of volatiles in the seismic cycle has been extended by implementations of the SHIVA rotary apparatus. Finally, an investigation on the rheological behaviour of clay- to sand-sized sediments under different conditions has now started both in the landslide and in the mud explosions areas of research.

The LNTS operates in the field of scientific instruments for Earth science investigation. The control electronics of the BRAVA machine was produced by LNTS as well as a series of airborne payloads for the LUSILAB ERC project and a series of sensor for use in volcanic areas. The Lab personnel successfully performed a third explorative mission using a drone over LUSI (Sidoarjo, east Java), where the LNTS airborne instruments have been flown and tested on the field. Moreover the LNTS supplies assistance to the Roma1 UF2 to maintain the geochemical station designed by LNTS. An instrument and a method for evaluate the performance of the high resolution AD converter used in seismometry is actually under development.

2I PERSONNEL

HPHT Laboratory

Piergiorgio Scarlato I Senior Researcher, Responsible of the HP-HT group

Carmela (Lilli) Freda I Senior Researcher, Responsible of the Experimental Laboratory

Brett Carpenter I Contract Researcher

Andrea Cavallo I Technologist

Gianfilippo De Astis I Researcher

Elisabetta Del Bello I Contract Researcher

Pierdomenico Del Gaudio I Technologist

Fabio Di Felice I Engineer Technologist

Damien Gaudin I Contract Researcher

Valeria Misiti I Technologist

Silvio Mollo I Researcher

Manuela Nazzari I Researcher

Tullio Ricci I Researcher

Elena Spagnuolo I Contract Researcher

Jacopo Taddeucci I Researcher

Telemaco Tesei I Contract Researcher

Pierre Yves Tournigand I Contract Researcher

Laboratory of New Technologies

Giovanni Romeo I Technical Director, Responsible of the Laboratory of New Technologies

Paolo Benedetti I Technician

Giuseppe Di Stefano I Senior Technologist

Alessandro Iarocci I Engineer Technologist

Massimo Mari I Technician

Francesco Pongetti I Engineer Technician

Giuseppe Spinelli I Engineer Technologist

Giuseppe Urbini I Engineer Technologist

Associated researchers

Cristiano Collettini | Sapienza Università di Roma, Italy | **Associated Professor**

Giancarlo Della Ventura | Università di Roma Tre | **Professor of Mineralogy**

Giulio Di Toro | University of Manchester | **Associated Professor**

Mario Gaeta | Sapienza Università di Roma, Italy | **Researcher**

Gianluca Iezzi | Università di Chieti, Italy | **Researcher**

Brent T. Poe | Università di Chieti, Italy | **Professor of Mineralogy**

Marco M. Scuderi | Sapienza Università di Roma, Italy | **Marie Curie Fellow**

Valentin R. Troll | Uppsala University, Sweden | **Chair of Petrology**

3I INSTRUMENTS and FACILITIES

HPHT Laboratory

- Multiple press 840 ton I Voggenreiter
- Piston cylinder - 3/4" and 1" pressure plates I Voggenreiter
- Multianvil - Walker type 6/8 I Voggenreiter
- Quick Press - Piston Cylinder 3/4" and 1" pressure plates I Depth of the Earth
- Bi-Tri-Axial Press (BRAVA) I RMP - INGV
- Slow to High Velocity rotary shear Apparatus (SHIVA) I RMP - INGV
- Electron microprobe equipped with 5 WDS and 1 EDS I JEOL JXA-8200
- Auto Carbon coater I JEOL JEC-530
- Field Emission Scanning Electron Microscope equipped with EDS and BSE detectors I JEOL JSM-6500F
- Fine coater I JEOL JFC-2300HR
- High and low temperature furnaces I Lenton
- Impedance analyser I Solartron SI1260
- Digital oscilloscope I Tektronix DPO4032
- Wave generator I Agilent 33250A
- H-Frame presses 10 ton I Enerpac
- Uniaxial testing machine with double load cell (15 and 250 kN) and LVDT controller I Tecnotest
- Precision balance I Sartorius
- Optical and stereo microscopes I Leica DMRXP and Euromex
- Ultra-high velocity, intensified, gated digital camera I Cordin 204-2
- High speed digital camcorder I Optronis and NAC 512 SC
- Stereomicroscopes I Leica MZ 9.5
- Semiautomatic polisher I Buehler Minimet 1000
- Power Supply I Agilent 6575A
- Helium Picnometer I AccuPyc II 1340
- Permeameter with double intensifier I Rock Physics
- Reometer MCR 301 Physica I Anton Paar
- Vertical Furnace RHTV 120-300/18 I Nabertherm
- High Temperature Furnace LHT 04/18 I Nabertherm

- Cecchi data acquisition system | Applied Seismology
- Rock drilling, cutting, and grinding equipment for samples preparation
- Thermal High speed camera | FLIR SC 645
- Welder PUK U3 | Lampert
- Laser line generator | Edmund optics
- Precision test sieves | Endecotts
- Laser MGL-III, 532nm 200mW, PSU-III-LED/Unit | Changchun New Industries
- Multi-Wavelenght Analyser with Particle sizing according to ISO 13317 | LUMiReader@PSA
- Polarized Free-field Microphones 40AN 1/2", Low Frequency (0.5Hz - 20kHz) | G.R.A.S.
- Vacuometro Pirani PVG-500

Acquired in 2015

- Petrographic microscope ECLIPSE E-50i POL | Nikon
- Drying oven UF 75 | Memmert
- Camera NAC | Memrecam-HX6

Laboratory of New Technologies

- Analog Oscilloscope | HP
- Analog Oscilloscope | Iwatsu SS5710
- Analog Oscilloscope | Tektronix TDS220
- Analog Oscilloscope | Tektronix
- Oscilloscope | HP54201
- Oscilloscope | HP54602b
- Power supply | Elind HL series
- Power supply | Elind 6TD20
- Power supply | DC DF1731SB
- Signal generator | HP8656A
- Function generator | HP3325A
- Multimeter | HP3478A
- Milling machine for printed circuit boards | T-Tech
- Logic state analyzer | HP16500A
- Superheterodyne spectrum analyzer | Tektronix

- Soldering-reworking station | JBC advanced AM6500
- Oscilloscope | FLUKE 199C
- Oscilloscope | Tektronix DPO4000
- Oscilloscope | Tektronix MSO4034
- Calibrator | FLUKE 5700 (series II)
- Function generator | HP33120
- Function generator | AGILENT 33250 A
- PXI Industrial computer with I/O boards | National Instruments
- Universal counter | HP53131A
- Waveform generator | Agilent 33210 A
- Oscilloscope W wave surfer | LeCroy 44MXs-A

Acquired in 2015

- 3d printer power Wasp
- 3d printer Delta 40 70

Machine shop

- Lathe | Grazioli Fortuna
- Small lathe | Ceriani
- Small milling machine | Schaublin
- Cutting machine | Ercoletta
- Bending machine | Ercoletta
- Drill press | Serrmac
- Small drill press | Webo
- Bandsaw | Femi
- Grinder | Femi
- Extractor hood | Filcar
- Inverter welding machine | Tecnica
- TIG welding machine | Cebora
- Miter saw
- Numerically controlled milling machine

4| LABORATORY ACTIVITIES

Experimental laboratory

Piston Cylinder apparatus

3/4 inch pressure plate: 5 experiments, in the frame of 1 project, have been performed. The project was devoted to the synthesis of olivine.

Quick press | Piston cylinder

The **1 inch pressure** plate has been used for 17 experiments in the frame of 1 project. The project was devoted to metamorphic rocks and their formation.

Furnaces

10 experiments have been performed in the frame of the following projects:

- Experimental study on radon emissions from high porosity tuffs exposed to sub-volcanic temperatures up to 800 °C.

Slow to High Velocity rotary shear Apparatus (SHIVA)

The fifth year of activity of SHIVA has been mainly dedicated at the investigation of frictional properties of cohesive rocks (e.g. gabbro, Carrara marble, basalts, serpentinite) and non-cohesive gouges under vacuum, room humidity and in the presence of fluids. We investigated the nucleation, propagation and arrest of earthquakes (and landslides) resulting from crustal deformation conditions (pressure, temperature, presence of fluids, stress perturbations, etc.). We studied the physico-chemical processes related to both the natural and induced deformation (i.e. acoustic emission, slip events, gases emanation, radon emanation, with participation to the NORTH premiale project) which are considered precursory to rupture nucleation. All the implementation addressed to these studies were preparatory for the start-up of the newly funded ERC "NOFEAR" project (P.I. Giulio Di Toro). We also studied the frictional properties of the gouge material recovered from the drilling (J-FAST, CRISP, SAFOD IODP) projects, the analogue materials retrieved from the Vajont landslide and mixtures of synthetic clays to provide information for numerical modeling and up-scale the experimental results to nature (participation to the ASTARTE project).

To achieve these goals, we performed 180 experiments during year 2015.

Some of these experiments were performed in collaboration with juniors scientists such as Piercarlo Giacomel (Master student Padua Univ., Italy now PhD at the University of Utrecht), Stefano Aretusini (PhD student, Padua Univ., Italy), Francois Passalegue (Postdoc, University of Manchester, UK), and international guests as Marie Violay (Researcher at EPSL, Lausanne, Swiss), LiWei Kuo (Lecturer at the Taiwan University, Taipei, Tw), Steven Smith (Lecturer at the Univesity of Otago, Dunedid, NZ) Paola Vannucchi (Lecturer at the Liverpool University, UK).

BRAVA

The year 2015 coincides with the fifth year of BRAVA activity. During this year we performed more than 150 experiments with a significant number of tests performed in the double direct shear configuration within the pressure vessel. The experimental work has been focused on finalizing the research lines foreseen in the ERC grant GLASS. In the following we summarize the main research themes:

1) Characterization of the frictional properties of carbonate/phyllosilicate-bearing faults including:

- Friction and healing properties of natural fault rocks (Tesei et al.);
- Friction and healing properties of decarbonated material (Carpenter et al.);
- Mechanical and chemical healing of Carrara marble (Carpenter et al.);
- Frictional properties and gouge development on large (20x20 cm) experimental faults (Tesei et al.);
- Frictional properties of natural fault rocks across the smectite/illite transitions (Tesei et al.);
- Frictional and healing properties of calcite-talc mixtures (Giorgetti et al.).

2) By reducing the stiffness of BRAVA, we have developed a method to cross the transition of stable sliding low/regular earthquakes in the lab. In addition, by investigating this transition with standard seismological techniques (cross-correlation of P-wave coda) we have been shedding light on the physical processes controlling slow/fast slip (Scuderi, Tinti, Marone et al.).

3) The role of fluid pressure in earthquake triggering. Here we have used a true triaxial stress field to characterize to role of fluid pressure in the evolution of Rate and State friction parameters. In addition we have started to run experiments in load control to test the fluid pressure threshold required to change the fault slip behaviour from creep to fast slip (Scuderi et al.).

Several researchers, including Chris Marone (Penn State University) in sabbatical in Rome, Paul Johnson (Las Alamos), Marie Violay and Felipe Orellana (Swiss Institute of Technology Lausanne), Frederic Cappa (University of Nice Sophia Antipolis France), Amir Sagy (Geological Survey of Israel) Federico Agliardi (University of Milano), Fabio Trippetta and Lorenzo Lipparini (University of Roma), have interacted with BRAVA to develop research topics on the mechanics of faulting and landslides.

Analog laboratory

A set of analog experiments were performed to investigate processes driving shallow explosions at White Island volcano (NZ). The experiments investigated the effects of varying shape, pressure and depth of exploding gas pockets and viscosity of enclosing medium on the dynamics of the ensuing explosion processes at the surface. In an ad-hoc designed setup about 300 runs were performed bursting balloons of different shapes and pressure

at different depths in water-kaolin suspensions of different viscosities. All experiments were recorded by two high speed cameras and two microphones, while suspension rheology was measured by using the MC301 Anton Paar rheometer.

Rheometer

57 experiments have been performed. Part of theme were tests conducted with siliconic oil, while the experiments have been performed with a solid-water suspension where the solid was made by clay/marble powder/sand.

FAMoUS (Fast Multiparametric Setup) TOOLBOX

The apparatus was implemented by providing a plug and play system for power connection. Connection and synchronization for the recently acquired NAC Memrecam HX-6 high-speed camera was provided. A specific connection was applied for operating the broadband seismometer Trillium Compact 120. Recalibration and extension of the thermal range to 25-1500° C interval was arranged for the thermal camera FLIR SC655. Two field experiments were carried out at Stromboli (May 2015) and Kilawea (Dec 2015), respectively, in order to study the behavior of basaltic explosive eruptions.

Microanalitical laboratory

FE-SEM and EMP performed 170 days of analyses in the frame of the following 25 research proposals.

Analysed samples included natural rocks, minerals experimental products.

Proposals

Pre-eruptive phase equilibria of magmas at Mt. Etna volcano: an experimental study
P.P. Giacomoni I Università di Ferrara

Analisi comparativa dei parametri geochimici, mineralogici e tessiturali di campioni di rocce piroclastiche del Distretto Flegreo e del Somma Vesuvio
L. Pappalardo I INGV-OV

Frictional behaviour and microstructures of calcite-bearing fault gouges
G. Di Toro I Università di Padova

The recent evolution of Turrialba Volcano (Costa Rica)
G. De Astis I INGV Roma 1

Investigation the CO_2 budget and source from active volcanoes in the Central American Volcanic Arc
A. Aiuppa I INGV Palermo

Identificazione di materiali vulcanici impiegati nell'edilizia dell'antica Roma
F. Marra I INGV Roma1

InteGrated Laboratories to investigate the mechanics of A Seismic vs Seismic faulting
C. Collettini I Università La Sapienza

The formation of rhyolitic melts of the Ramadas eruption
G. De Astis I INGV Roma 1

INGV DPC 2014-2015
M. Di Vito I INGV OV

Precursori di Eruzioni progetto V2 Convenzione C DPC-INGV 2014
M. D'Antonio I INGV OV

Textural and micro-chemical features of fault rocks from Central Apennines
G. Iezzi I Università di Chieti

Explosivity of gas-overpressure and vapor-explosion driven fragmentation in volcanic system
C. Montanaro I University of Munich

Analisi geologico-strutturale e microstrutturale in zone di faglia in rocce carbonatiche: meccanismi deformativi e ruolo dei fluidi
A. Billi I Università di Roma La Sapienza

High resolution geochemical of volcanic ash
D. Perugini I Università di Perugia

Low temperature methanation in geologic environments
G. Etiope I INGV Roma 2

Analysis of the pyroclastic deposits of the December 29th 2013 eruption of Chaparrastique volcano (San Miguel, El Salvador)
E. Del Bello I INGV Roma 1

Viscosity of pure sulfur
T. Scolamacchia I University of Munich

Study of the characteristic behaviour of active/exhumed faults VS large scale gravitative movements sliding planed in central Italy
M. Moro I INGV Roma 1

Paleoenvironmental reconstruction
A. Smedile I INGV Roma 1

The role of crystal mushes in the differentiation process of calc-alkaline magmas
V. Tecchiato I Università di Roma La Sapienza

Hydrocarbons migration patterns of the north-west edge of the platform Apula 1
F. Trippetta I Università di Roma La Sapienza

Hydrocarbons migration patterns of the north-west edge of the platform Apula 2
F. Trippetta I Università di Roma La Sapienza

The causes and consequences of large scale ash aggregation
S. Mueller I university of Munich

Experimental petrology study constrain the trachy-basalt magma-anhydrite interaction
T. Mandolini I Università di Urbino

Cannonballs: a peculiar features of (basaltic) scoria cones?
A. Di Piazza I INGV Roma 1

5I RESEARCH PROJECTS

1. MIUR – Programma Nazionale di Ricerche in Antartide I Stabilità delle fasi idrate nel mantello litosferico dei grandi sistemi di rift continentale: un approccio petrologico-sperimentale su noduli e lave basiche della Terra Vittoria Settentrionale I **P.I. Mollo S.**

2 International Continental Scientific Drilling Program - ICDP I Krafla Magma Drilling Project I **P.I. Eichelberger J.**

3. European research project I VERTIGO 'Volcanic ash: fiEld, expeRimenTal and numerIcal investiGations of prOcesses during its lifecycle', an EU International Training Network I **P.I. Kueppers U.**

4. National Science Foundation project I Strombolian and Hawaiian Explosions: New Insights From Synchronizing Videos and Exsolved Volatiles. I **P.I. Houghton B.**

5. European Research Project I MED-SUV (Mediterranean Super Volcanoes): Long-term monitoring experiment in geologically active regions of Europe prone to natural hazards: the Supersite concept I **P.I. Puglisi G.**

6. Progetto Premiale MIUR 2012 I NoRth: New hORizons of the Technology applied to experimental researches and geophysical and volcanological monitoring I **P.I. Scarlato P.**

7. Italian Civil Protection, INGV 2014-2016 Agreement I V1 Probabilistic evaluation of volcanic hazard I **P.I. Marzocchi W.**

8. European Research Council - Consolidator Grant ERC CoG 614705 I New Balloon Observations Of Millimetric Extragalactic Radiation I **P.I. ASI - Romeo G.**

9. Sviluppo di un sistema di misura di gas in aria per uso su drone I **P.I. Romeo G.**

10. FP7-IDEAS-ERC LUSILAB I Lusi: a unique natural laboratory for multidisciplinary studies of focussede fluid flow in sedimentary basin I **P.I. Mazzini A.**

11. EU Project -ERC Starting Grant Project GLASS: InteGrated Laboratories to investigate the mechanics of ASeismic vs. Seismic faulting I **P.I. Collettini C.**

12. EU Project -ERC Consolidator Grant Project NOFEAR: New Outlook on seismic faults: From EARthquake nucleation to arrest I **P.I. Di Toro G.**

6| PARTNER LABORATORIES

1. **Institute of Geochemistry and Petrology** | ETH Zurich | **Switzerland**
2. **Dipartimento di Scienze Biologiche, Geologiche e Ambientali** | Università di Catania | **Italy**
3. **Dipartimento di Fisica e Scienze della Terra** | Università di Ferrara | **Italy**
4. **Planetary Environmental Facilities** | Aarhus University | **Denmark**
5. **Physical Volcanology Laboratory** | Lancaster University | **UK**
6. **Petro-Volcanology Research Group** | Università di Perugia | **Italy**
7. **Experimental Volcanology Lab** | Munich University | **Germany**
8. **Laboratorio di Cosmologia Sperimentale** | Sapienza Università di Roma | **Italy**

7 | PARTNER INSTITUTIONS

1. Institute of Geochemistry and Petrology | Swiss Federal Institute of Technology in Zurich (ETHZ) | Switzerland
2. Dipartimento Geotecnologie | Università di Chieti | Italy
3. Dipartimento di Scienze della Terra | Sapienza Università di Roma | Italy
4. Dipartimento di Scienze Geologiche | Università degli Studi Roma Tre | Italy
5. Istituto di Geoscienze e Georisorse | CNR | Italy
6. Dipartimento di Fisica e Scienze della Terra | Università degli Studi di Ferrara | Italy
7. Dipartimento di Scienze Biologiche, Geologiche e Ambientali | Università di Catania | Italy
8. Department of Geology and Geophysics | SOEST | USA
9. Instituto de Geología del Noroeste Argentino | Universidad Nacional De Salta | Salta, Argentina
10. Department of Physics and Astronomy | Aarhus University | Denmark
11. Department of Earth and Environmental Sciences | University of Munich | Germany
12. Department of Earth Sciences | University of Durham | UK
13. Lancaster Environment Centre | Lancaster University | UK
14. HVO Hawaiian volcano observatory | USGS | USA

8.1 PETROLOGY, MINERALOGY, VOLCANOLOGY

Studies on the formation of rhyolites from Ramadas Volcanic Center (Altiplano-Puna, Argentina) through microprobe analyses, SEM investigations and experiments of melting at variable pressure

G. De Astis, V. Misiti, R. Becchio, G. Giordano, L. Bardelli

Research Line V1

Ramadas volcanic centre (RVC - 6.6 Ma old) is a monogenetic calderic depression, now largely obliterated, almost coeval with the Late Miocene outbreak of highly explosive silicic activity in the Altiplano-Puna plateau. Ramadas erupted a rather complex suite of garnet-bearing, rhyolitic pyroclastic rocks (Tait et al., 2009), dominated by a fall deposit (>35 km^3) and starting with the emplacement of lag breccia containing abundant metasedimentary lithics and garnet-tourmaline leucogranites. In proximal-intermediate outcrops multiple fall layers alternated with PDC deposits, whereas close to the main vent the waning phreatomagmatic stages of the eruption formed a small volume tuff-ring. A lava coulée was emplaced at the end of the eruption. Unusually, the dominant pyroclasts in the tuff-ring sequence are non-vesiculated fragments of peraluminous (rhyolitic) perlite. Volcanological data together with textural features of typical tube pumice evidence a volatiles-rich, plinian eruption, produced by an

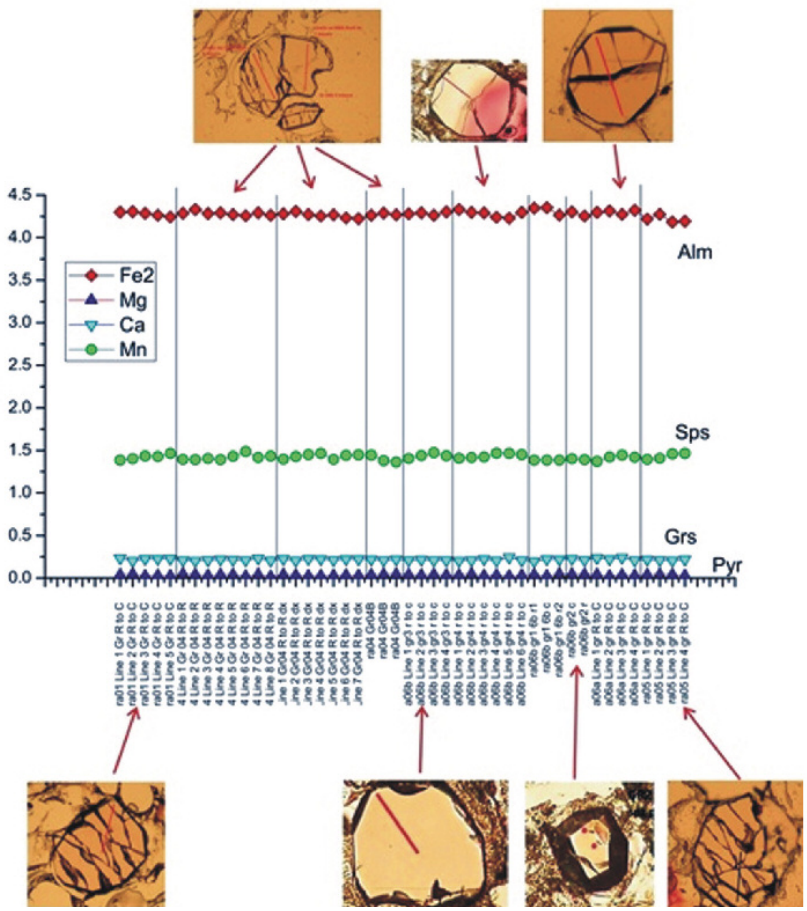

Fig. 1 I Friction of an low-displacement thrust (Millaris Fault) is similar to the friction of large-displacement weak faults (San Andreas fault, Zuccale low-angle normal fault, Nankai thrust).

aphyric rhyolitic magma, with garnet as micro-phenocrysts.

A new set of petro-textural and mineralogical data on the volcanic products erupted by RVC have been collected through the use of JEOL JXA-8200 microprobe and JEOL JSM-6500F FeSEM at the HPHT Laboratory (INGV, Rome). Petrographic and textural studies on juveniles confirm the presence of euhedral garnet as dominant phase and identify micrometric metaigneous fragments (Qtz+Bt+Kfs+Mt+Tur). BSE imaging and microprobe analyses on glasses, garnets and accessory mineral phases (zircon and monazite) provide further data to understand the genesis and eruptive conditions of these atypical rhyolites, which result to be even geochemically different from those outcropping in the same region (strong Ba, La, Sr and HREE depletion, strong Eu negative spike). Garnets display a homogeneous, unzoned almandine-spessartine composition (Alm72-71Sps24-23Grs4-3Pyr0-1 – Fig. 1) and are contained in a glassy groundmass with peraluminous character. Although the garnets of post-magmatic origin (e.g. the fumarolic ones) are not so rare in lavas, those of magmatic origin are uncommon and can crystallize only under restricted P-T conditions. Additionally, the presence of Zr and Mnz is associated with both magmatic and high-T metamorphic processes. Although our data set must be widened, our study and preliminary modelling point to the occurrence of thermal metamorphism shifting to partial melting of Fe-MnO-rich metapelitic rocks (or even re-melting of older acid volcanics), with final extraction of volatiles-rich rhyolitic melts, able to produce a plinian eruption. The hypothesis of crustal partial melting was tested through a wealth of pressure calibration experiments on La Puna crustal rocks (still going on) by a piston cylinder apparatus (Quick-Press) that is suitable for experiments at pressure between 150 and 500 MPa. Figure 2 shows some photos of rocks studied after the running, where evidence of melting are visible.

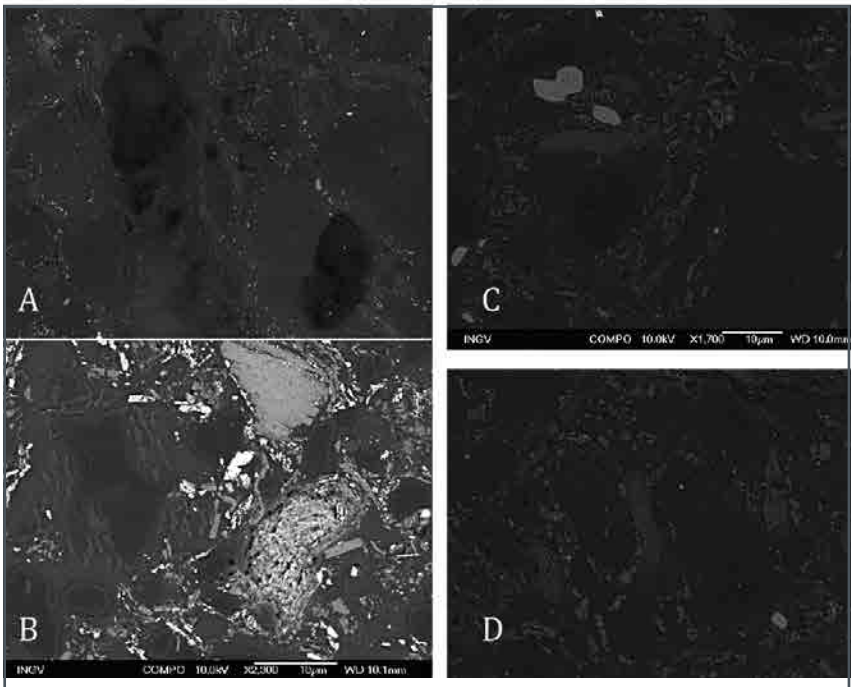

Fig. 2 I A) Migmatite photo: experiment QP1 84, 6 hours at P= 4 kbars and T= 700°C – heating rate = 50°C/min.
B) Metapelite photo: experiment QP1 87, 6 hours at P= 4 kbars and T= 800°C – heating rate = 50°C/min.
C-D) Micaschist photos: experiment QP1 86, 6 hours at P= 4 kbars and T= 800°C – heating rate = 200°C/min.
Blue points in photos A and D represent the spots on mineral phases and glass (melted portions) where EDS semi-quantitative analyzes have been carried out.

Chemical and degassing dynamics of magma-sulfate ($CaSO_4$) interaction

F. M. Deegan, V.R. Troll, C. Freda, J. Bedard, V. Misiti, H. Geiger

Research Line V3

There is growing evidence that emplacement of large igneous provinces (LIPs) is linked to catastrophic climate change and mass extinctions. A fundamental control on the severity of the environmental impact of LIPs seems to be the type of sedimentary rock that was intruded. Volatile-rich sediments including limestones, shales, sandstones, and sulfate evaporites de-gas in contact with magma, liberating greenhouse and toxic gases such as CO_2, CH_4, SO_2, and halocarbons. In the Canadian High Arctic Igneous Province (HALIP), magmatic sills that supplied large outpourings of magma are intruded into crustal rock sequences that include sulfate, shale, and carbonate. The HALIP thus represents an ideal case study for examining the chemical and degassing processes involved in magma-sulfate interaction.

We have begun an experimental petrology research program to replicate magma-sulfate interaction using high temperature (1200°C), time-varied petrological experiments, similar in design to previous magma-carbonate interaction experiments carried out at INGV (Fig. 1).

We generated our first results in November – December 2014 and expect that further analysis of our experiments will generate insights into i) large-scale crustal degassing during emplacement of the HALIP with implications for paleo-climate changes and ii) processes during magma-crust interaction that can lead to economic concentrations of sulfides from $CaSO_4$ recycling. Another magma-sulfate experimental series using recently synthesised hydrated magmatic starting material is planned for 2016.

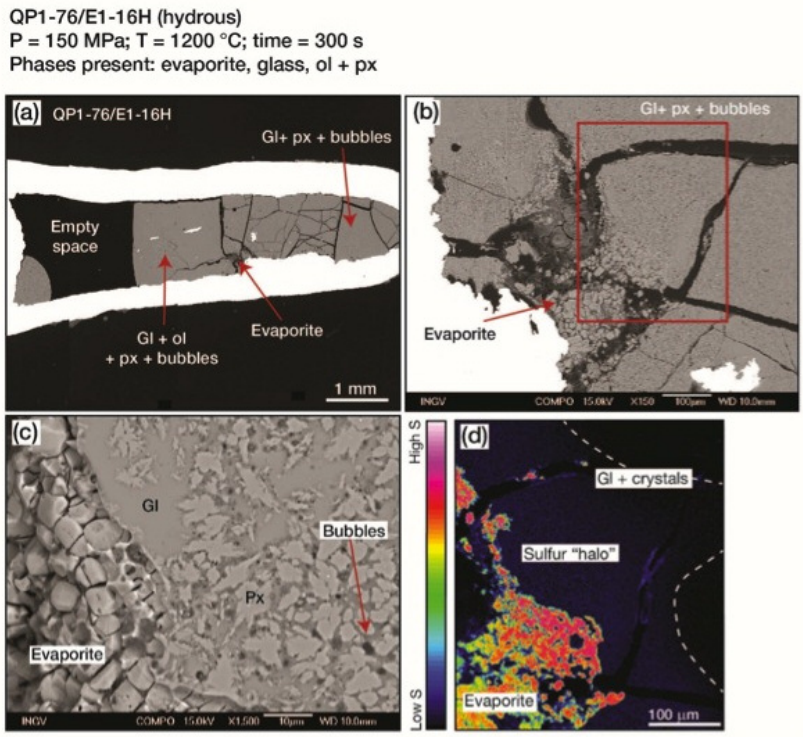

Fig. 1 I Results of a basalt-sulfate interaction experiment carried out at 150 Mpa, 1200 °C, for 300 s. (a-c) Scanning Electron Microscope images of the experiment at varying scales show the sulfate, glass, crystals, and bubbles. (d) Sulfur map of the boxed area in (b). The S-map was carried out using the Field Emission Electron Probe Micro Analyser at Uppsala University, Sweden and shows a halo of S-enriched glass and crystals surrounding the sulfate. (Gl = glass, px = pyroxene, ol = olivine)

Effect of particle volume fraction on the settling velocity of volcanic ash particles: implications for ash dispersion models

E. Del Bello, J. Taddeucci, M. De' Michieli Vitturi, P. Scarlato, D. Andronico, S. Scollo, U. Kueppers

Research Line V3

We report experimental measurements of the enhanced settling velocity of volcanic particles as function of particle volume fraction. In order to investigate the differences in the aerodynamic behaviour of ash particles when settling individually or in mass, we performed systematic largescale ash settling experiments using natural basaltic and phonolitic ash. By releasing ash particles at different, controlled volumetric flow rates, in an unconstrained open space and at minimal air movement, we measured their terminal velocity, size, and particle volume fraction with a high-speed camera at 2000 fps. Enhanced settling velocities of individual particles increase with increasing particle volume fraction (Fig. 1). This suggests that particle clustering during fallout may be one reason explaining larger than theoretical depletion rates of fine particles from volcanic ash clouds. We provide a quantitative empirical model that allows to calculate, from a given particle size and density, the enhanced velocity resulting from a given particle volume fraction. The proposed model has the potential to serve as a simple tool for the prediction of the terminal velocity of ash of a hypothetical distribution of ash of known particle size and volume fraction. This is of particular importance for advection diffusion transport model of ash where generally a one-way coupling is adopted, considering only the flow effects on particles. To better quantify the importance of the enhanced settling velocity in ash dispersal, we performed 3D numerical simulations (using the Discrete Particle Model DPMFoam of the open source software OpenFOAM) investigate the effect of particle volume fraction on the surrounding air (Fig. 2). Particles with a normal size distribution are released in still air with zero velocity from the top of the domain. The incompressible

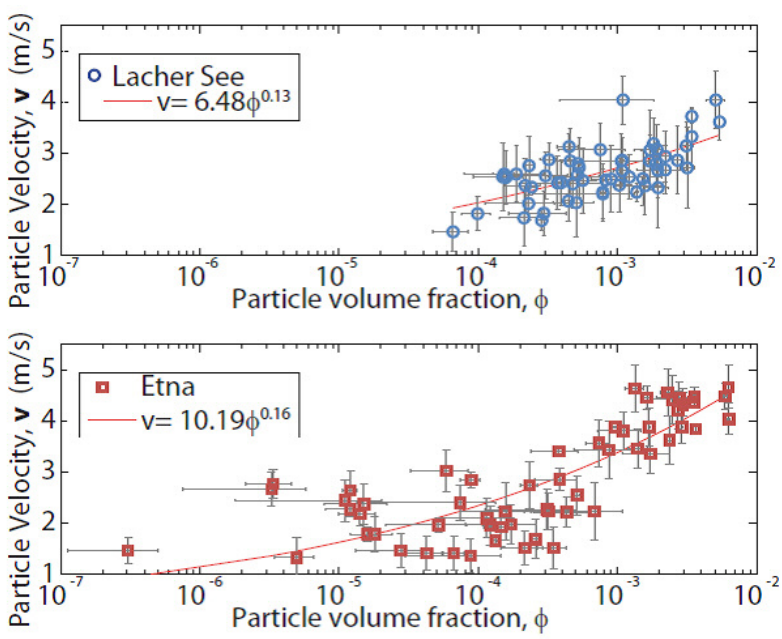

Fig. 1 | Plotting particle velocity against particle volume fraction provides a power law relationship in the form $v = k\Phi^n$, k and n being dependent on the density and size. Each point represent the v and Φ averaged over 40 frames sequences.

Navier-Stokes equation is solved in an Eulerian frame and the transport equations in a Lagrangian frame for the continuous and the discrete (particles) phases, respectively. The two phases are coupled mostly through momentum transfer due to buoyancy and drag. We finally introduced the new formulation in a Lagrangian model calculating for realistic eruptive conditions the resulting ash concentration in the atmosphere and on the ground.

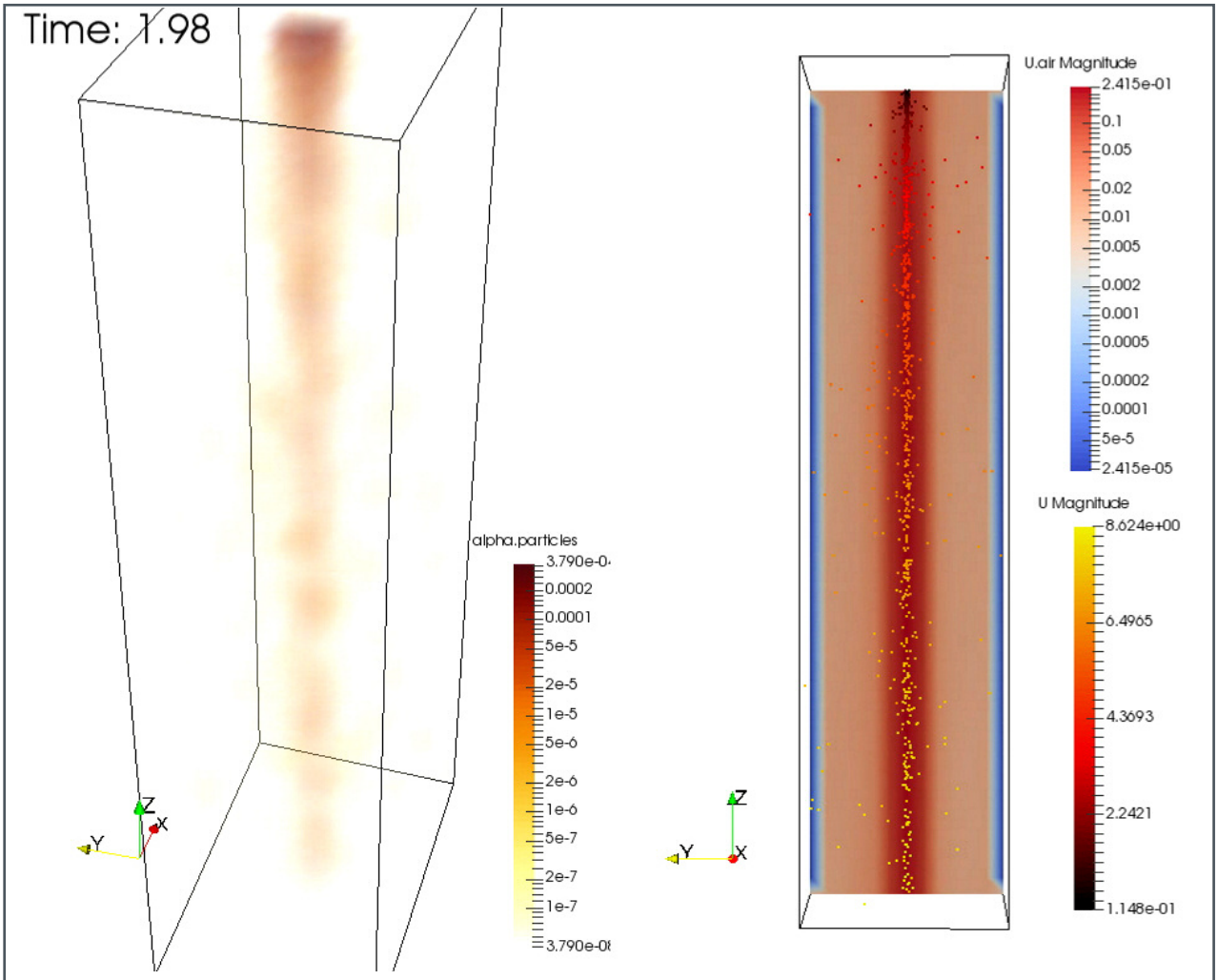

Fig. 2 I A still frame from a 3D numerical simulation showing the distribution of the particle volume fraction (alpha particles, left panel) and air (U air magnitude, right panel) increasingly accelerating downwards due to particles sedimentation with increasing particle mass flow rate. As a consequence, the terminal velocity of particles increases (U magnitude, right panel).

Dynamics of strombolian eruptions at Batu Tara volcano (Indonesia)

P. Scarlato, E. Del Bello, T. Ricci, D. Gaudin, J. Taddeucci, C. Cesaroni

Research Line V3

In September 2014, high-speed imaging and acoustic data were acquired during 3 days of almost continuous recording (04-06/09/2014) at Batu Tara Volcano, in the small isolated island of Pulau Komba, in the Flores Sea (about 50 km N of Lembata). This volcano is very similar to the Italian Stromboli Volcano in both eruptive style and edifice morphology. The field experiment aimed at investigating degassing and explosive dynamics using a combination of GPS synchronized devices deployed in direct view of the active vent:

i) a high-speed visible camera acquiring images at 500 frames per second (fps);

ii) a thermal infrared (FLIR) camera acquiring at 50-200 fps;

iii) a visible time lapse camera (GOPRO) acquiring at 0.2-0.5 Hz (2-5 s interval);

iv) two broadband microphones (Freq. range of kHz to 0.1 Hz) sampled at 10 kHz.

Explosions can be discriminated in type according to their visual, thermal and acoustic features. Some explosions are characterized by a first sudden radial ejection of large spatter and bombs (main pulse), eventually followed by other similar events (secondary pulses), with very little amount of ash involved. In these eruptions, infrasonic waveforms are characterized by a first, high amplitude transient, with a first positive peak pressure followed by rapid dampening, typical of a Strombolian eruption (Fig. 1a).

Other explosions are characterized by the sustained ejection of a dense jet of ash, with abundant decimetre to meter sized spatter and hot blocks. These eruptions are not accompanied by a maximum peak pressure at the eruption onset. Spectrograms show a high frequency component propagating for the entire duration of the signal (Fig. 1b). These two distinct types are sometimes overlapping and eruptions show a high amplitude transient followed by a high frequency coda (Fig. 1c). These different evolutions suggest that there are at least two repeatable explosion dynamics occurring in the conduit, with comparable gas overpressure, source depth and amount of gas involved.

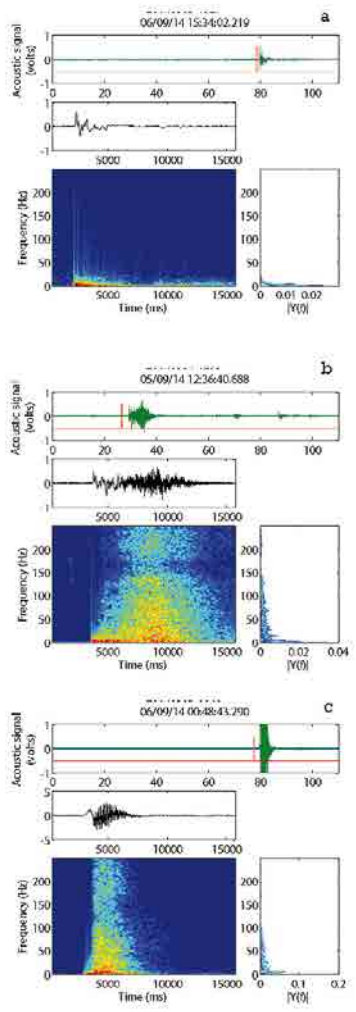

Fig. 1 I Examples of explosion types at Batu Tara based on infrasonic data. a) 'Strombolian-like' infrasonic waveform, characterised by a first positive peak pressure followed by rapid dampening. b) Explosions characterised by a long lasting high frequency component. c) Explosions with overlapping infrasonic waveforms.

Slugs and Plugs: the role of conduit boundary conditions in modulating strombolian explosive activity

E. Del Bello, S. Lane, E. Llewellin, M. James, J. Taddeucci, P. Scarlato, A. Capponi

Research Line V3

Strombolian activity is common in low-viscosity volcanism. It is characterised by quasi-periodic, short-lived explosions, which, whilst typically weak, may vary greatly in magnitude. The current paradigm for a strombolian volcanic eruption postulates a large gas bubble (slug) bursting explosively after ascending a conduit filled with low-viscosity magma. However, recent studies of pyroclast textures suggest the formation of a region of cooler, degassed, more-viscous magma at the top of the conduit is a common feature of strombolian eruptions. Following the hypothesis that such a rheological impedance could act as a 'viscous plug', which modifies and complicates gas escape processes, we conduct the first experimental investigation of this scenario. We find that: 1) the presence of a viscous plug enhances slug burst vigour; 2) experiments that include a viscous plug reproduce, and offer an explanation for, key phenomena observed in natural strombolian eruptions. Our scaled analogue experiments show that, as the gas slug expands on ascent, it forces the underlying low-viscosity liquid into the plug, creating a low-viscosity channel within a high-viscosity annulus. The slug's diameter and ascent rate change as it enters the channel, generating instabilities and increasing slug overpressure. When the slug reaches the surface, a more energetic burst process is observed than would be the case for a slug rising through the low-viscosity liquid alone. Fluid-dynamic instabilities cause low and high viscosity magma analogues to intermingle, and cause the burst to become pulsatory. The observed phenomena are reproduced by numerical fluid dynamic simulations at the volcanic scale (Fig. 1), and provide a plausible explanation for pulsations, and the ejection of mingled pyroclasts, observed at Stromboli and elsewhere.

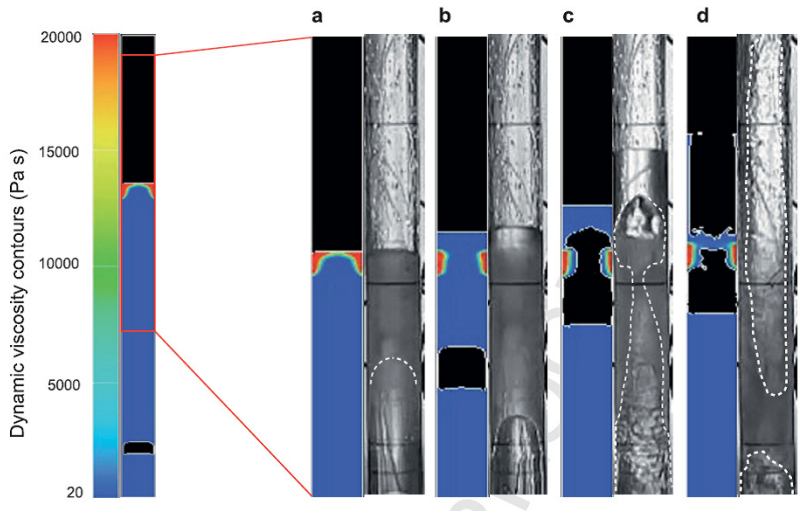

Fig. 1 I Results from 3D numerical simulation at the volcanic scale. The parameters of the simulation are: slug initial volume 22m^3, magma viscosity 20Pas, plug viscosity 20000 Pas; plug thickness 6m, conduit diameter 3m, magma column height 200 m. Still frames (a, b, c, d) extracted from the simulation show good comparison with experiments at the same scaled conditions, in terms of burst dynamics and liquid film perturbations, supporting the experimental procedures.

The second Broadband Acquisition and Imaging Operation (BAcIO2) at Stromboli Volcano (Italy)

P. Scarlato, J. Taddeucci, E. Del Bello, D. Gaudin, T. Ricci, P.Y. Tourningard, D. Andronico, T. Orr, B. Houghton, R. Carey, N. Clements, U. Kueppers, M. Burton, A. Sutton, G. Tamburello, M. Bitetto, R. D'Aleo

Research Line V3

The second edition of BAcIO, a multidisciplinary experiment gathering a large combination of worldwide monitoring expertise, was held in Stromboli in May 2015. This year, the experiment was attended by an international group of researchers from 8 countries and 16 research institutes or universities. The research, headed by INGV, has as its objective the improvement of understanding of Strombolian eruptive dynamics. The main topics of this year were: 1) the use of synchronized systems for stereoscopic filming of the eruptive activity, 2) acquisition of thermal images through a high speed IR camera, 3) acquisition of acoustic signals through a network of microphones, 4) measurement of geochemical variations of SO_2 in the summit area through the use of a UV chamber, 5) sampling of the ash, gases and aerosols. The deployment of instruments in the field consisted of a range of imaging, acoustic, and seismic data acquisition systems located at the "Roccette" (Fig. 1), plus a range of geochemistry measurements tools at the

Fig. 1 | The high-speed cameras array during the BAcIO2 campaign at 'Roccette' in May 2015. On the left side of the picture, the new NAC Memrecam HX7 camera. In the middle of the picture, FAMoUS apparatus, including the visible OPTRONIS high-speed camera plus the infrared FLIR camera. On the right side of the picture, the Phantom high speed camera, property of Hawaii University. UV cameras from UniPa were also operating at the same site.

"Pizzo sopra La Fossa" (Fig. 2). Imaging systems included: three high-speed visible cameras acquiring synchronized images at 500 and 1000 frames per second (property of INGV and the University of Hawaii); one thermal infrared forward looking (FLIR) cameras zooming into the active vents and acquiring at 50-200 fps; two high-definition cameras acquiring at lower (3-50 Hz) frame rates with a broader field of view; one UV camera system for the measurement of sulphur dioxide emission (University of Palermo). Acoustic systems included two broadband microphones (range of tens of kHz to 0.1 Hz), co-located with one of the high-speed cameras. The geochemistry measurements included two multi-gas stations (From Cambridge University and Hawaiian Volcano Observatory - USGS).

One of the main achievements of this year's campaign is the synchronized use of a third high-speed camera, setting up the first array of high-speed cameras deployed in a volcanic environment. By allowing to obtain three different fields of view of the same process, the use of three cameras has greatly increased the degree of precision reached by three-dimensional reconstruction of the expulsion and air transport of pyroclasts.

Fig. 2 I A panoramic view of the "Pizzo sopra la Fossa" from the "Roccette", where the Cambridge and HVO multi-gas stations were located.

KRAFLA MAGMA DRILLING PROJECT – the contribution of the HPHT experimental laboratory

HPHT group, S. Mollo, T. Ricci, E. Del Bello, M. Nazzari, D. Gaudin, G. Galli, A. Sciarra

Research Line V1 and V2

The Krafla Magma Drilling Project (KMDP), a component of the International Continental Scientific Drilling Program (ICDP), is an open multi-national consortium of scientists, geothermal engineers, and Landsvirkjun National Power Co. aimed at coring through the subsolidus – hypersolidus boundary in granite ("felsite") to liquidus rhyolite. The Krafla site, with its unprecedented 4-D view of a magma-hydrothermal system from source to surface, will be used

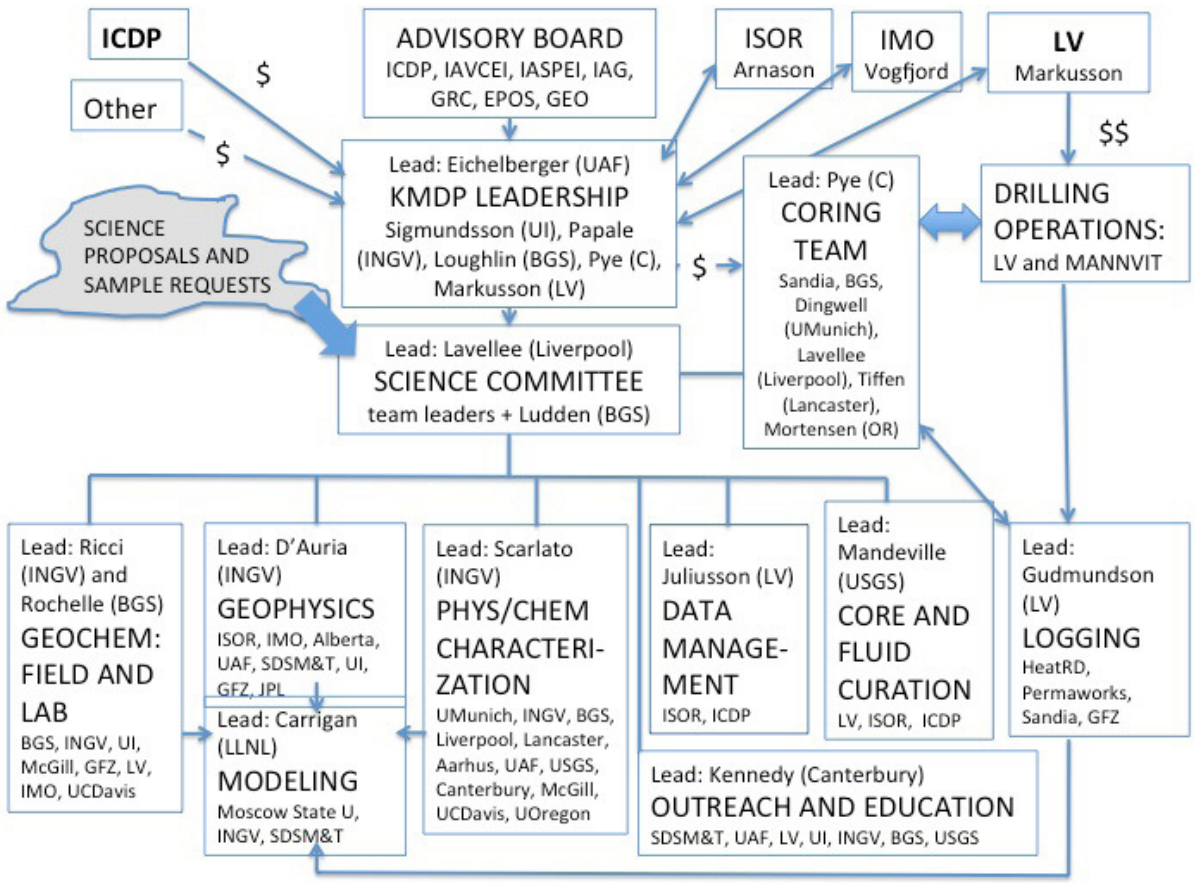

Fig. 1 I Organogram of KMDP showing leading roles of HPHT lab members.

to test and advance geophysical and geochemical volcano monitoring methods including emplacement of sensors in the magma chamber, assess the energy potential and optimal engineering approach for magma energy, investigate magma-hydrothermal coupling through intentional perturbation of the system, benchmark coupled mass-heat transfer reservoir models with self-induced thermal fracturing, and provide experiential learning in fields of volcano

hazards and renewable energy. The well is scheduled to be drilled in 2017, and a number of geophysical and geochemical experiments will be conducted in the frame of KMDP prior to, during, and after the drilling. The science team is divided into 9 disciplinary teams with designated leads and clear roles and responsibilities.

In the framework of the KMDP the HPHT laboratory will have a major involvement into selected research activities related to magmatism and geothermal drilling operation. In particular key personnel is involved in the physical/chemical/mechanical characterization of magma under Krafla caldera and the investigation of its relationship to the overlying hydrothermal system (Fig. 1). The activities of the proponents can be grouped into three main research areas:

1) Textural and chemical characterization of products (matrix glasses, fluid/melt inclusions, minerals and bulk rocks) from cores or fragments of the drilled rhyolitic magma, the felsite host rock, and a variety of samples from the phreatic explosion crater Viti within the Krafla system. Elemental (major and trace elements) and isotopic (radiogenic and stable isotopes) analyses will be performed to address the question of rhyolite petrogenesis, determine the temperature of the magma, and the timescales of interaction between rhyolites and mafic melts/crystals/hydrothermal fluids.
2) Experimental work aiming to simulate the emplacement of rhyolite within the shallow crust and track the crystallization behaviour of the magma through cooling rate experiments conducted under variable temperatures and melt-water concentrations. Viscosity determination on the chips from IDDP-1 measured with the falling sphere technique.
3) Geochemical surveys aimed at characterizing the diffuse degassing occurring inside the Krafla caldera and on its rims. Thermal imaging of the Krafla caldera area using an airborne thermal camera.

The 2013 eruption of Chaparrastique volcano (El Salvador): Effects of magma storage, mixing, and decompression

P. Scarlato, S. Mollo, E. Del Bello, A. von Quadt, R. Brown, E. Gutierrez, B. Martinez-Hackert

Research Line V2

On December 29, 2013, an isolated vulcanian-type eruption occurred at Chaparrastique volcano (El Salvador), after 12 years of inactivity. The explosion was classified as VEI 2 and produced an ash plume with maximum height of ~9 km. Therefore, with the aim to elucidate the magmatic processes responsible for the reawakened volcanic activity, textural and compositional details preserved in phenocrysts from the erupted products have been investigated in this study

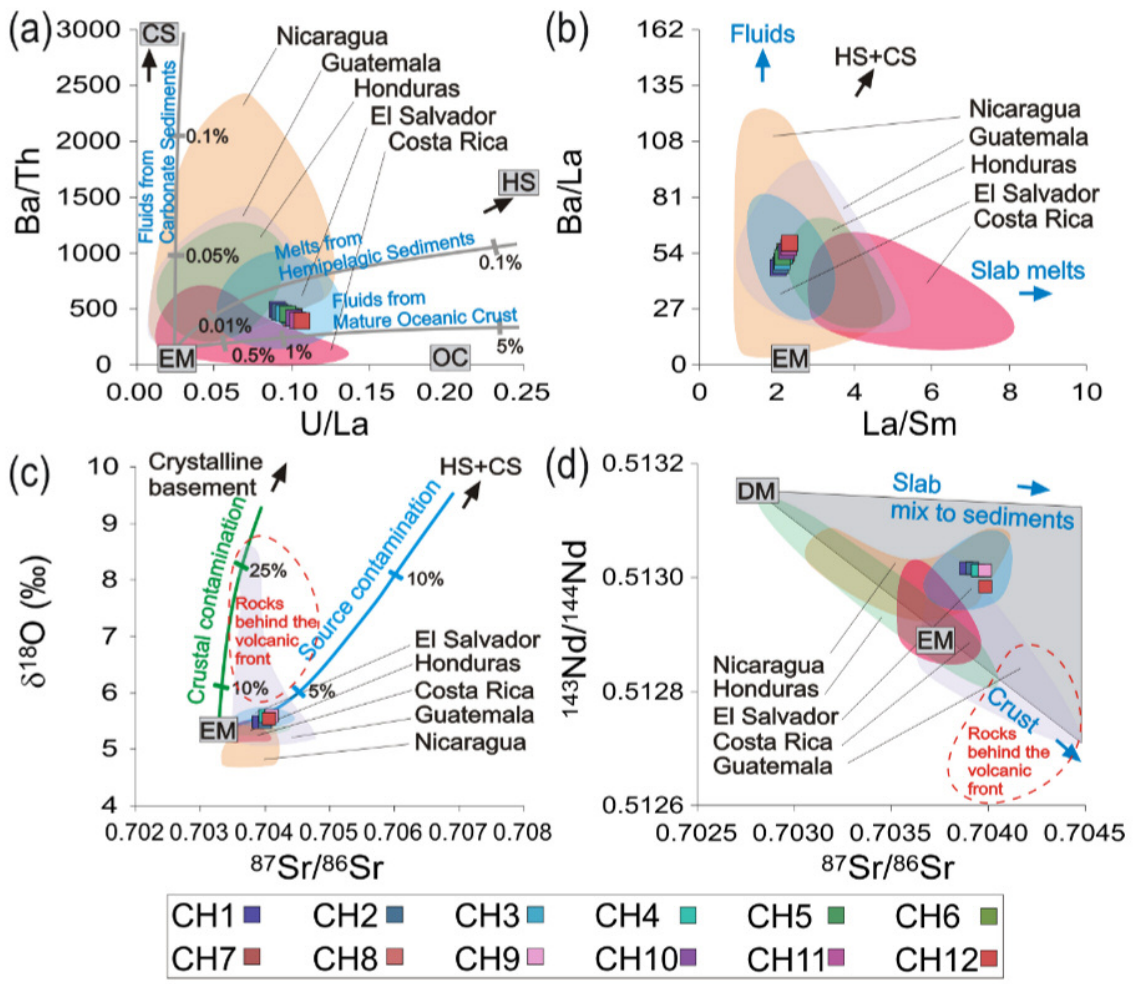

Fig. 1 I U/La vs. Ba/Th diagram based on soluble/insoluble element pairs. (a). La/Sm vs. Ba/La diagram based on ratios of elements that are not highly fluid mobile in arc systems, such as the REE and HFSE. This diagram allows to evidence the contribution of to the mantle wedge of melt-like components derived from the subducted slab (b). $^{87}Sr/^{86}Sr$ vs. $\delta^{18}O$ diagram that serve to discriminate crustal and source contamination.(c). $^{87}Sr/^{86}Sr$ vs. $^{143}Nd/^{144}Nd$ diagram shows evidence of crustal contamination for rocks in Guatemala that are behind the volcanic front. However, most of the volcanic products in Central America define an array with positive slop that represents a mix between the enriched MORB source and the subducted slab (d). EM, enriched MORB source. OC, oceanic crust. CS, carbonate sediments. HS, hemipelagic sediments. DM, depleted MORB source.

and integrated with geochemical and isotopic information from bulk rocks.

Phenocrysts consist of Fo-rich poikilitic olivines hosting high-Mg titanomagnetites, and Fo - poor olivines coexisting with low-Mg titanomagnetites. Mineral-melt equilibria suggest an origin for the distinct phenocryst populations by mixing between a high-T (~1130-1150 °C), basaltic magma with fO_2 (NNO buffer) typical of the lower crust in arc systems and a low-T (~1060-1080°C), basaltic andesitic magma with fO_2 (NNO+1 buffer) commonly encountered in shallower, more oxidized crustal reservoirs. Thermobarometry based on Fe-Mg exchange between orthopyroxene and clinopyroxene constrains the crystallization before eruption at relative low-P (~150-250 MPa) and low-T (~1000-1050 °C). Mixing between two compositionally distinct magmas is also evidenced by the occurrence of reverse zoned plagioclase phenocrysts with resorbed sodic cores and re-growth of sieve-textured calcic mantles. Conversely, plagioclase rims exhibit disequilibrium compositions addressed to decompression kinetics (~10^{-3} MPa/s) driven by rapid magma ascent to the surface (~0.03 m/s). Major and trace element modelling excludes fractional crystallization as the primary mechanism controlling the bulk rock variability, whereas geochemical data align along a mixing trend between two end-members representative of the primitive basalt and the differentiated basaltic andesite. Trace element and isotope data indicate that the primary source of magmatism is an enriched MORB-like mantle with the contribution of fluxes of metasomatic fluids and/or melts produced by the subducted slab. The role played by slab-fluid inputs of carbonate origin and slab- melts from the hemipelagic sediments seems to be minimal. Assimilation/contamination processes of magmas by crustal rocks are also negligible. In contrast, the geochemical signature of magmas is greatly influenced by slab-derived aqueous fluids produced prevalently by progressive dehydration of marine sediments and altered basaltic crust.

Rheological properties of debris- and mud-flows

P. Del Gaudio, G. Ventura

Research Line V3

In order to understand the movement and mechanisms of emplacement of gravity flows like debris- mud-flows, an appropriate rheological model of hyper-concentrated and dilute flows is required. In this study, we performed experiments using as starting material kaolin, marble powder, and sand variously mixed with water. A rheometer Anton Paar MCR301 equipped with vane geometry is used. At first, we studied suspensions of the separated solid component (kaolin and marble powder) mixed with selected weight fractions of water, then we studied the rheology of mixtures of kaolin and sand with different weight proportions of water.

Future experiments will include additional experiments using three solids and water mixtures. Steps at constant shear stress are applied for a sufficient time to reach a constant value of shear rate and viscosity. Once we have determined the values of viscosity and shear rate at each stress, the flow curves are reconstructed.

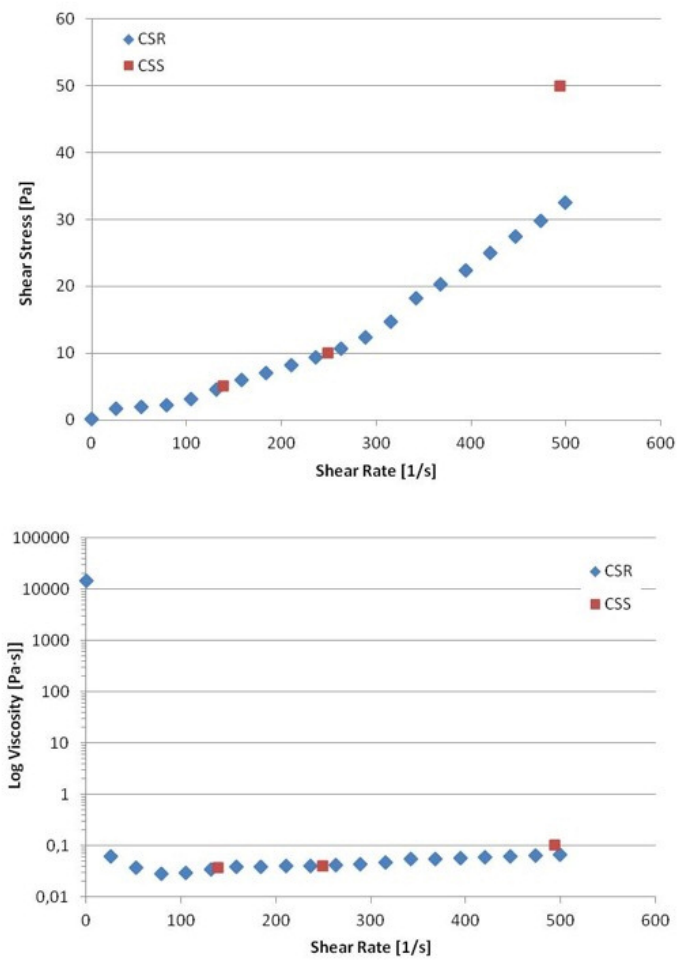

Fig. 1 I The figure shows the flow curves of a kaolin-sand water suspension. CSR is controlled shear rate experiment while CSS is controlled shear stress experiment.

The studied suspensions clearly show a non-Newtonian rheology.

At a fixed solid fraction, the suspension of kaolin and water displays the highest viscosity; the addition of sand to the kaolin-water suspension reduces the viscosity of the mixture. These preliminary results reveal the importance of a detailed analysis of complex, multi-sized suspensions in the study of mud- and debris-flows (Fig. 1).

Hydrogen diffusion in nominally anhydrous minerals: implications for mass and charge transport

A. Del Vecchio, B. T. Poe, V. Misiti, M. Cestelli Guidi

Research Line V2

In the last decades, knowledge about hydrogen incorporation in nominally anhydrous minerals has become essential to understand the dynamic behaviour of the Earth's mantle, because it plays a key role in several processes and has a large effect on the physical and chemical properties of minerals.

HP and HT synthesis were carried out at High Pressure and High Temperature Laboratory of INGV Rome: as starting material we used natural San Carlos Olivine and synthetic forsterite, obtained by a combination of mechanical activation and heat treatment of Talc ($Mg_3Si_4O_{10}(OH)_2$) and hydroxyd magnesium carbonate $MgCO_3$*$Mg(OH)$*H_2O, using a chamber furnace at high temperature Nabertherm LHT 04/18 until 1600 °C.

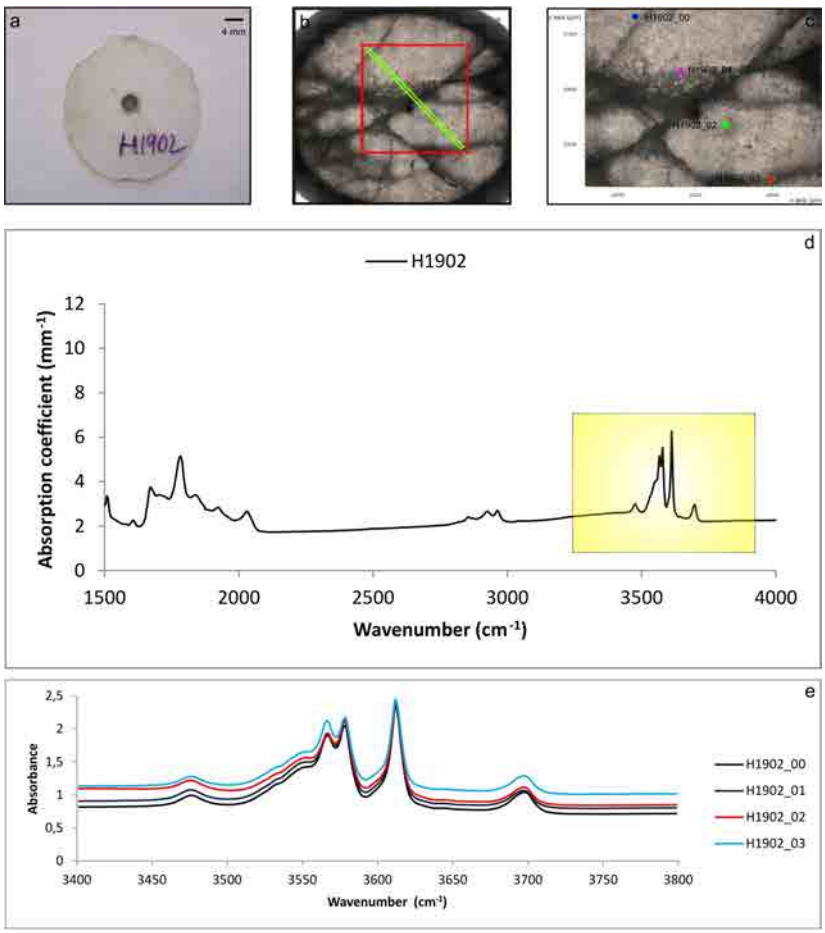

Fig. 1 I a) H1902 sample (forst+196,001 wt ppm H2O), b) view of 15X objective acquired with Hyperion 3000 microscope (LNF-Frascati) and c) data points of FTIR spectra. d) FTIR spectra of H1902 and e) FTIR spectra of data points in the frequence range of 3400-3700 cm-1 showing OH vibrational modes evenly distributed throughout the sample area.

Policrystalline materials were placed in platinum capsules and hydrated with fluid source and synthesized using a Voggenreiter 3/4 inch end-loaded piston cylinder apparatus end-loaded type at INGV Istituto Nazionale di Geofisica e Vulcanologia in Rome. Pressure was increased to 1,5 GPa and then AC power was supplied to reach experimental value of 1100 °C, with a gradient ob about 100°C/min.

FTIR spectra were acquired at INFN – LNF of Frascati, using SINBAD (Synchrotron Infrared Beam At Dafne), one of the light lines linked to DAFNE, the synchrotron radiation facility actually used at the LNF of Frascati.

FTIR spectroscopy represents the primary method to analyse the presence of hydrogen in nominally anhydrous minerals, because OH bonds are very sensitive to interaction with IR source, leading to stretching vibrational modes in a frequency range between 3200 – 3700 cm^{-1}.

FTIR spectra were acquired by smmothed and polished sections with thickness between 300 – 700 micron: for every sample we acquired images using Hyperion 300 microscope (15X objective), and we obtained a series of data point spectra to analyse the presence of H_2O and the omogeneous distribution of hydroxyl groups in all sample area.

Using Paterson calibration we obtain total OH concentrations of our samples (wt ppm H_2O), while using Peakfit 4.2 software we identified each peak with a Lorentzian equation characterized by three parameters such as frequence (wavenumber) absorbance and width in the middle of the peak (Fig. 1).

These parameters allow us to study mechanisms by which hydroxyl groups are incorporated in olivine and forsterite crystal lattices.

Raman vibrational spectroscopy gives us important informations about the strength of the Si-O bonds in the tetrahedral structure, and the interaction between tetrahedral and octahedral structure.

Analysis or Raman spectra show that the presence of hydroxyl groups lead first to a weakening of the structure, mainly on the stretching vibrational modes of Si-O bonds of the tetrahedral structure, and creating new vibrational modes representing new Si-OH groups in the silicate.

Unrest at Turrialba volcano (Costa Rica)

A. Di Piazza, A. Rizzo, M. DeMoor, G. Alvarado-Induni, G. De Astis

Research Line V1 e V2

Turrialba volcano is located directly upwind of the Central Valley of Costa Rica, which is home to ~60% of the country´s population and the international airport. The volcano has experienced six magmatic eruptions during the last 3400 years. The last major eruption occurred in 1864-1866 and was preceded by phreatic eruptions, which transitioned to phreatomagmatic activity and climaxed with Strombolian eruptions.

This progression is a classic example of the expected events as a rising magma body displaces a shallow crustal hydrothermal system, and is well preserved in the geologic record. In the last years the reactivation of the volcano, produced ash eruptions that have significantly affected this part of Costa Rica. We have collected over 80 ash samples from the 2014-2015 eruptions. These ashes are complex mixtures of hydrothermal minerals, free crystals, variably altered lithics, and glassy clasts (Fig. 1a) in different proportions. Some (rare) clasts are very well preserved (Fig. 1a) with fresh matrix glass and pristine crystals; these ones sometimes displayed molten/quenched rims, and others showed cryptic chemical alteration and/or secondary minerals lining vesicles. The appearance of juvenile material marks a fundamental threshold in eruptive behavior that is important to recognize from a hazards perspective.

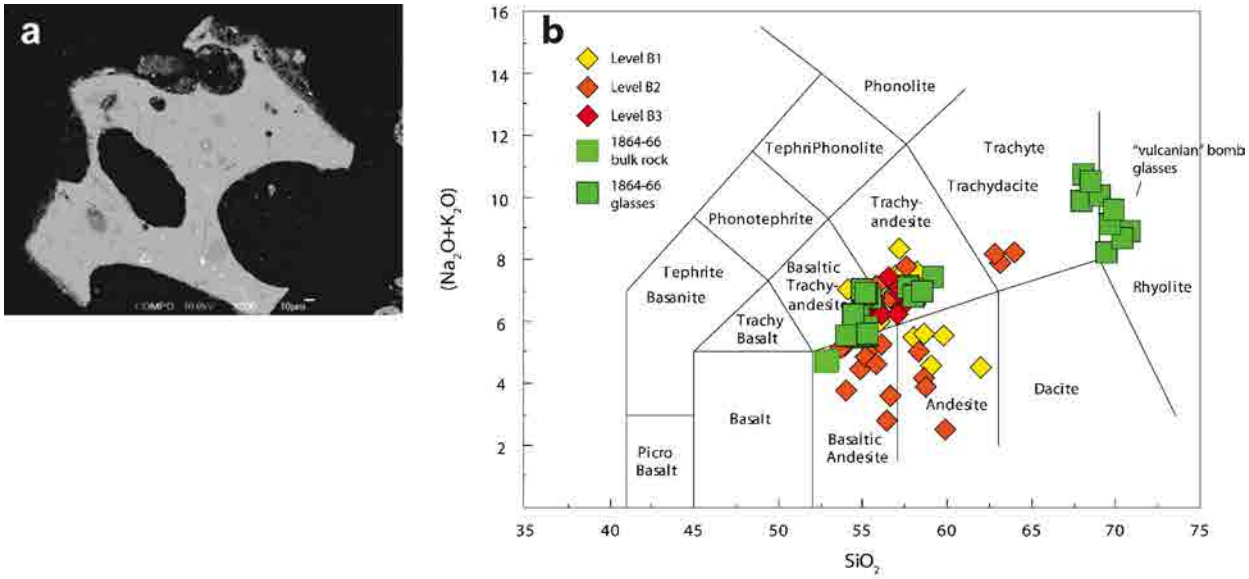

Fig. 1 I (a) SEM imaging of fresh glassy clasts, potentially representing new magma reaching the surface. However, these clasts (b) have similar composition to the magmatic products from the 1864-1866 eruption.

The composition of the unaltered component, obtained through EMPA analyses on fresh glasses, is very similar to that of the previous magmatic eruption (basaltic trachyandesite to trachyandesite; Fig. 1b).

To compound the problem, alteration of freshly deposited material can occur very rapidly, probably on a scale of days to weeks in the conduit region where acid gas concentrations are high. Thus, we are left with a seemingly intractable problem of importance to all reactivating volcanoes: it's hardly difficult to distinguish (petrologically or geochemically) between new magma inputs at the surface and/or erosion of old magmatic (or phreatomagmatic) products in these types of ashes.

Cannonballs: a peculiar features of (basaltic) scoria cones?

A. Di Piazza, E. Del Bello, S. Mollo

Research Line V2

The term "cannonball" is referred to spherical or sub-spherical eruptive products, generally not vesiculated, that are found at monogenic volcanoes worldwide, such as Olot (Spain), Cerro Chopo (Costa Rica), Pacaya (Guatemala), Pelagatos Cone (Messico), Cinder Cone – Lassen volcano (USA). Generally they were interpreted as hot pasty lava rounded by mechanical processes while travelling at high speed down slopes. However the mechanism of formation is not well demonstrated and not properly deepened.

In this project we propose to study some cannonball samples from Cerro Chopo and Agua Zarcas monogenic cones (Costa Rica). Thin sections of cm- to mm-size samples were prepared, cutting the sample from core-to-rim. This to analyze the morphological features of vesicles and the compositions of crystals focusing on the transition zone between core and rim. Through SEM-EDS observations a clear distinction between a core and a rim zone can be made (Fig. 1). These two domains show significant differences in textural features such as vesicle and crystal distributions (Fig. 1). The core zone is characterized by larger vesicles (diameter up to 0.78 mm); the distribution of the vesicle population is polymodal, reflecting coalescence phenomena on the larger size vesicles and the collapse of the smaller ones. The rim zone is micro-vesiculated (diameter up to 0.12 mm) and shows a significant population of microlites (specially pyroxenes and oxides). Chemical map will be performed through SEM-EDS, in order to unveil the distribution of the chemical elements inside the samples. In addition EMP-Microanalyses of minerals and glasses will be performed to understand the process responsible for the formation of this peculiar eruptive products.

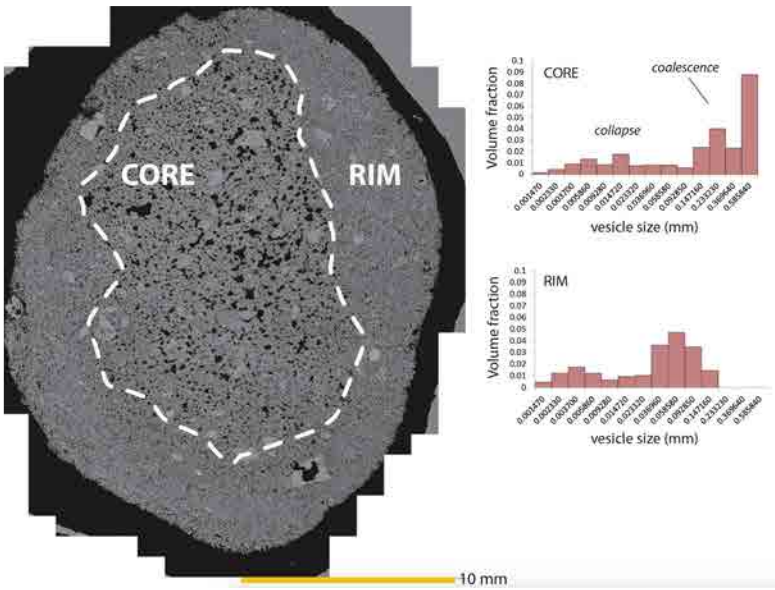

Fig. 1 I BSE image of the entire cannonball sample from Cerro Chopo volcano. On the right, Vesicle Volume Distribution of core and rim zones.

3D Reconstruction of pyroclast trajectories using high speed cameras and photogrammetry

D. Gaudin, J. Taddeucci, P. Scarlato, E. Del Bello, B. Houghton, T. Orr, D. Andronico, U. Kueppers, R. Carey

Research Line V3

High speed videos of volcanic explosions enables the reconstruction of pyroclasts trajectories, with a three-fold interest: 1) to better constrain the ejection mechanism, 2) to spot eventual in-flight collisions and interaction with gas and/or ash plumes, and 3) to compute the final emplacement of bomb-sized clasts with some implications for hazard assessment and risk managements. However, videos are intrinsically two-dimensional, and motion towards or away from the observatory is not taken into account, which may lead to the underestimation of bomb velocities and does not allow studying the directionality of the ejections.

To overcome this limitation, we adapted photogrammetry techniques to reconstruct 3D trajectories of pyroclasts erupted during explosions at Stromboli (Aeolian Islands, Italy) and spattering at Halema'uma'u lava lake (Kilauea, Hawaii, USA). In each case, we used two or three high-speed video cameras (500-1000 Hz frame rate), set up to form an angle of 5-10° with respects to the observed activity. The synchronization was achieved using a common triggering signal. Pyroclasts were tracked manually on the videos, and feed a home-made algorithm based on photogrammetry techniques.

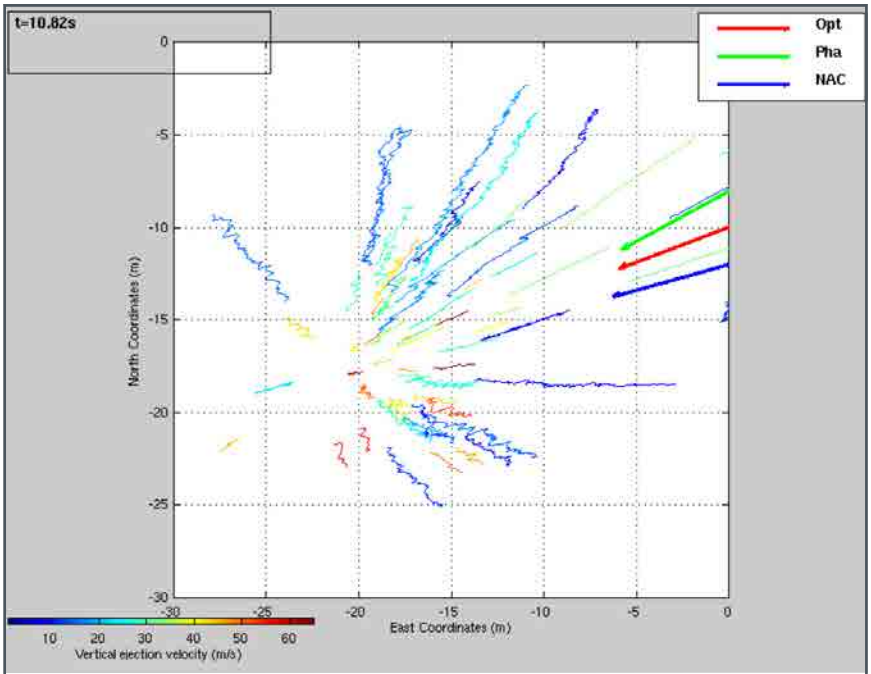

Fig. 1 | Bird-eye view reconstruction of bomb trajectories erupted during an explosion at Stromboli volcano. The three arrows represent the direction of the three cameras, and the trajectories are color-coded according to the vertical ejection velocity. Note that all the trajectories originate from the same region (i.e. the vent), and that the slowest particles are located at the periphery (modified from Gaudin et al., AGU 2015).

The analysis of the trajectory of tens of bombs at some key moments of the explosions allows observing the internal structure of the jet, with faster bombs generally erupted in the center and slower bombs in the periphery. It also enables the identification of identify shifts of the mean directivity and the dispersal angle of the jets during the explosions (Fig 1). These reconstructions are in excellent agreement with the observations from monitoring systems, demonstrating the applicability of our method.

Integrating puffing and explosions in a general scheme of vent dynamics during Strombolian-style volcanic activity

D. Gaudin, J. Taddeucci, P. Scarlato, A. Harris, M. Bombrun, E. Del Bello, T. Orr, B. Houghton, T. Ricci

Research Line V3

The denomination "Strombolian activity" covers a large variety of volcanic explosions, both in terms of intensity (from puffing to normal Strombolian explosions) and of type of products (gas, ash, bombs). All of them are believed to be caused by the same mechanism, i.e. the burst of gas pockets in the volcanic conduit. In order to better constrain the controls on the different eruption styles, we used the large thermal infrared high speed videos database collected at Stromboli (Italy, 2012, 2013, 2014, 2015), Batu Tara (Indonesia, 2015), Yasur (Vanuatu, 2011), Etna (Italy, 2014). This database includes all the known types of Strombolian activity: 1) puffing, corresponding to frequent (typical frequency of seconds) burst of meter sized gas pockets gas, 2) rapid explosions, i.e. the repeated ejection of bombs at 30 m/s, and 3) normal Strombolian explosions where initial velocities can reach 400 m/s. The latter is, in turn, classified according to its ejecta contents in types 0 (gas-rich), 1 (bomb-rich), 2a (bomb- and ash-rich), and 2b (ash-rich). We developed qualitative and quantitative tools to allow the comparison, in single plots, of these different types of activities. In particular, rise history diagrams allows observing the frequency, temperature, velocity and ejecta content of all the types of explosions. In parallel, we paid a particular attention to quantify the puffing activity (gas pockets volumes and frequency), whose variations of intensity are an excellent indicator of the upper conduit conditions. In the short-term, we aim to replace all Strombolian activity in a general interpretative scheme (Fig. 1).

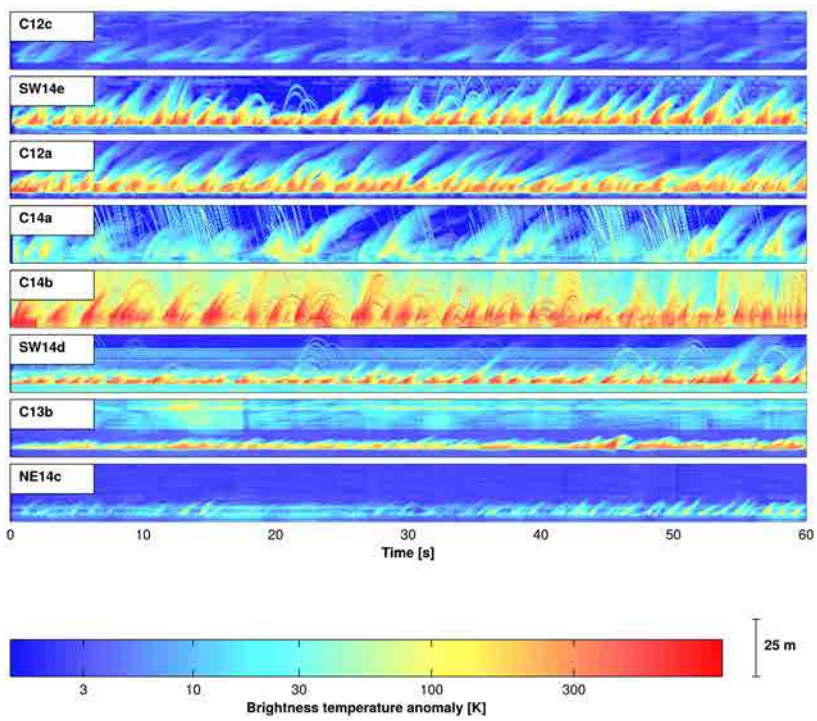

Fig. 1 | "Rise history" diagrams characterizing puffing activity at Stromboli from high speed-thermal videos. For each frame, the temperature anomaly generated by hot gas and pyroclasts is highlighted by removing the background temperature, defined for each pixel as the minimum pixel temperature in a 2 s preceding the observation. The time-evolution of the temperature anomaly is then represented with respect to the height, by retaining on each frame only the maximum value computed for each row of the video. Bombs and gas puffs appear as parabolas and streaks and respectively, with an inclination related to their rise (or fall) velocity.

Unraveling the Eyjafjallajökull 2010 plumbing system and magma chamber dynamics through high-resolution geochemical investigations

K. Laeger, M. Petrelli, D. Andronico, P. Scarlato, C. Cimarelli, V. Misiti, E. Del Bello, D. Perugini

Research Line V3

The April–May 2010 eruption of the Eyjafjallajökull volcano (EFJ, Iceland) was triggered by an intrusion of fresh magma coming from deeper portions of the crust migrating into shallower depth of 3-6 km in the magmatic system. Here, we present new EMPA and LA-ICP-MS analyses on groundmass glasses of ash particles erupted between 18.05. -22.05.2010 (Fig. 1). The glasses define two well separated groups: The first group is basaltic in composition with SiO_2 ranging from 49.98 to 51.76 wt.% and a total alkali content ($Na_2O + K_2O$) in the range between

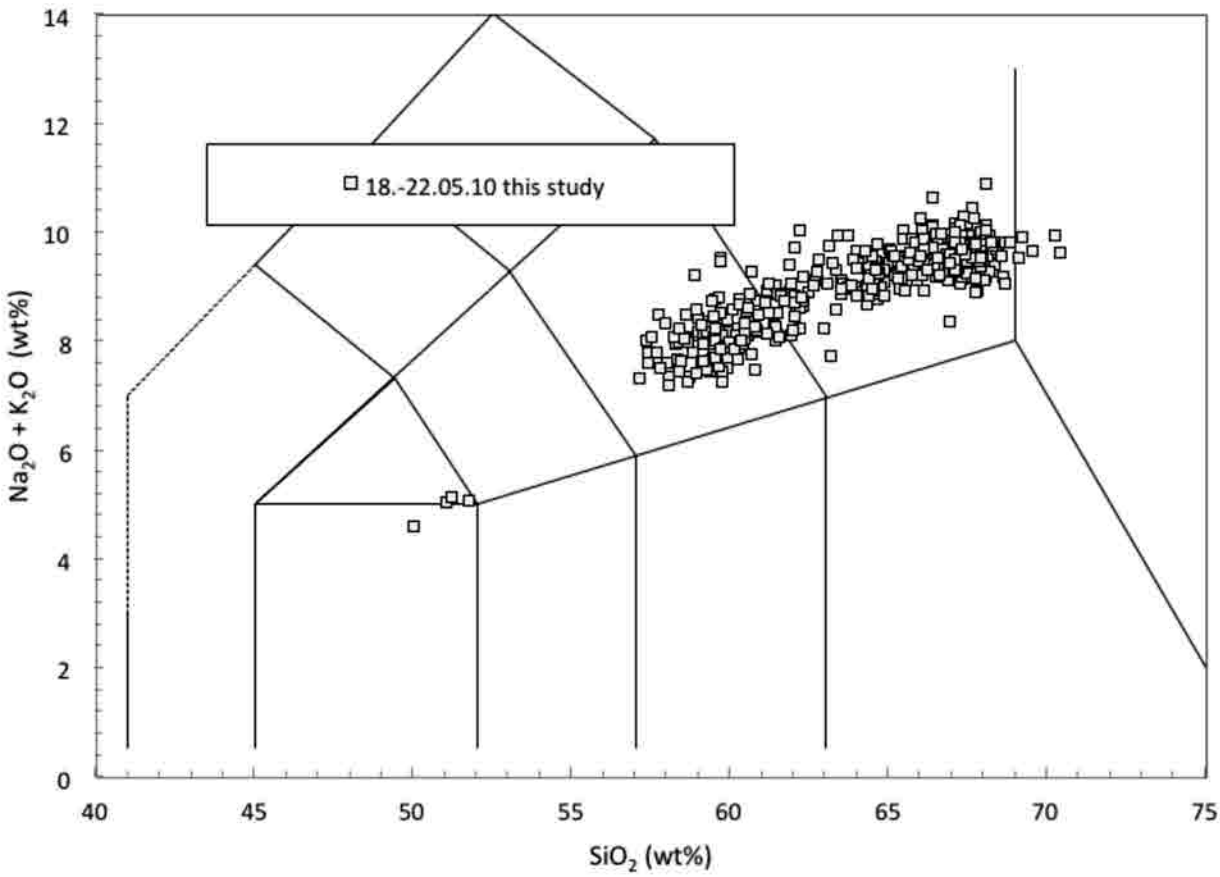

Fig. 1 I Total alkali versus silica diagrams of lava and tephra of the 2010 EFJ eruption deposited between 18. – 22.05.10.

4.63 and 5.17 wt.%. The second group ranges between trachyandesitic and rhyolitic compositions with SiO_2 ranging between 57.13 to 70.38 wt.% and a total alkali content from 7.21 to 10.90 wt.%. Least square modelling after Störmer and Nicholls (1978) discriminates best the origin of the basaltic glass by both fractional crystallization of

a more primitive basalt or mixing of a basalt and a felsic magma (Fig. 1). Furthermore, this model proves that the trachyandesitic range is the result of mixing of trachyandesite and trachyte magma. Magma mixing modeling after Langmuir (1978) and element concentration histograms indicate a probable incomplete magma mixing as the main process forming the great compositional variability observed in the erupted products. Finally, we estimated mixing end-members of intermediate (~59 wt.% SiO_2) and felsic composition (~66-68 wt.% SiO_2) with a felsic melt-proportion of 0.35-0.47.

In the 90s, recorded seismicity and ground deformation indicated intrusions at shallow depth under the EFJ edifice probably forming separated sills. Therefore, the origin of the trachyandesite is presumably to find in a discrete magma batch that generated years before eruption. The rhyolite composition can be considered as the residual melt that remained in the plumbing system of EFJ since the last eruption in 1821-23. We suggest that these different magma batches formed the plumbing system of EFJ and have been remobilized by the intrusion of new basaltic magma from depth, triggering the 2010 eruption.

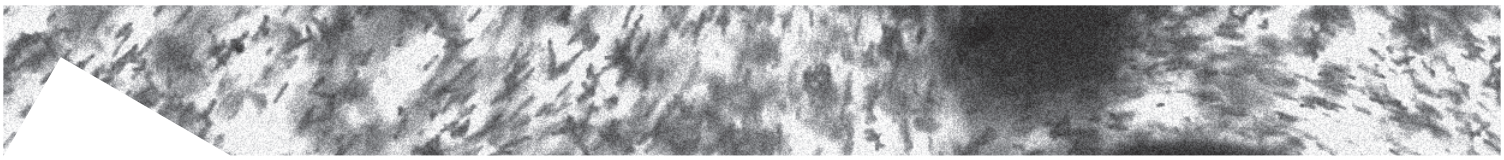

Melt extraction in mush zones: the case of crystal-rich enclaves at the Sabatini Volcanic District (central Italy)

M. Masotta, S. Mollo, M. Gaeta, C. Freda

Research Line V2

A peculiar feature of the Sabatini Volcanic District (SVD, central Italy) is the occurrence of crystal-poor pumices and crystal-rich enclaves within the same eruptive host-deposit. The stratigraphic sequence of pumices and enclaves indicates the tapping of a stratified magma chamber, where a crystal-poor phonolitic magma laid on top of a more primitive crystal-rich magma. The crystal-rich enclaves are genetically related with the pumices and record the evolution of a solidification front, in which a more differentiated melt was produced, extracted and eventually erupted. We collected and analysed crystal-rich enclaves from one of the largest phonolitic eruptions at the SVD, and used their petro-chemical features to reconstruct magma differentiation and crystal-melt separation in the solidification front. On this basis, three groups of enclaves have been identified: porphyritic enclaves, holocrystalline enclaves and sanidinites (Fig. 1a). The mineralogical variability faithfully reproduces the spatial and temporal evolution of the solidification front, from early-to-intermediate crystallisation conditions (porphyritic- and holocrystalline-type), to the late stage of solidification (sanidinites), in which the percolation of a more differentiated melt through the crystal mush triggered the instability of the solidification front. Results from numerical models indicate that gravitational instability is the most efficient mechanism to explain melt extraction in mush zones of medium-sized (~10 km^3), short-lived (~10^4 years) magma chambers (Fig. 1b).

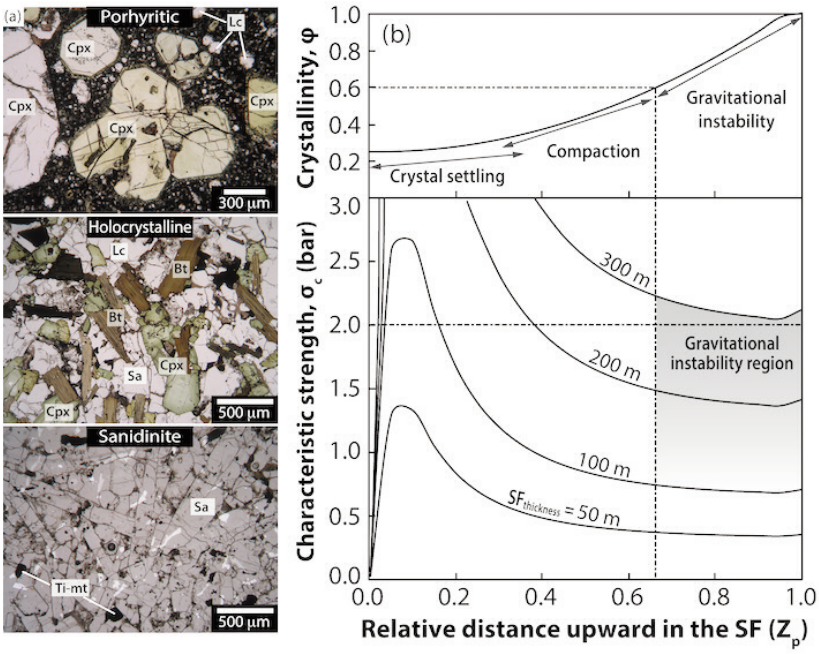

Fig. 1 | (a) Microphotographs of the crystal-rich enclaves, namely porphyritic (top), holocrystalline (middle) and sanidinites (bottom), **(b)** Crystallinity and characteristic strength calculated at each point along the solidification front as a function of the crystal fraction; the shaded grey area indicates the weakest part of the solidification front that are subjected to tearing or detachment of the crystalline network.

Glass stability of silicate glasses with sub-alkaline compositions

V. Misiti, A.L. Elbrecht, M. Davis, G. Iezzi, F. Vetere, A. Cavallo, S. Mollo

Research Line V1

The resistance of a glass to crystallise upon heating is defined as glass stability (GS). High and low GS imply a reluctance and facility to nucleate, respectively. GS is defined via several parameters, commonly determined by differential scanning calorimeter (DSC) spectra to measure Tg (glass transition), Tx (onset of crystallization) and Tm (melting) temperatures. However, glass-forming ability (GFA) and especially GS attributes of natural and widespread sub-alkaline silicate melts and glasses are poorly known. Thereby, six sub-alkaline silicate glasses were investigated to capture their GS and correlate that with their GFA. Six sub-alkaline glasses were prepared starting from two natural rocks (basalt: B100 and rhyolite: R100); the other four glasses, B80R20, B60R40, B40R60 and B20R80, were prepared by mixing in wt.% B100 and R100. Each glass was mounted in Al_2O_3 sample holders (B100 also in Pt) and heated in a DSC at a rate of 10 °C/min (600 °C/h) from ambient to liquidus temperatures. The DSC run products were, after quench, analysed by SEM and EPMA, in order to characterise the amount of each phase by image analysis (area %) and their composition (wt.%), respectively.

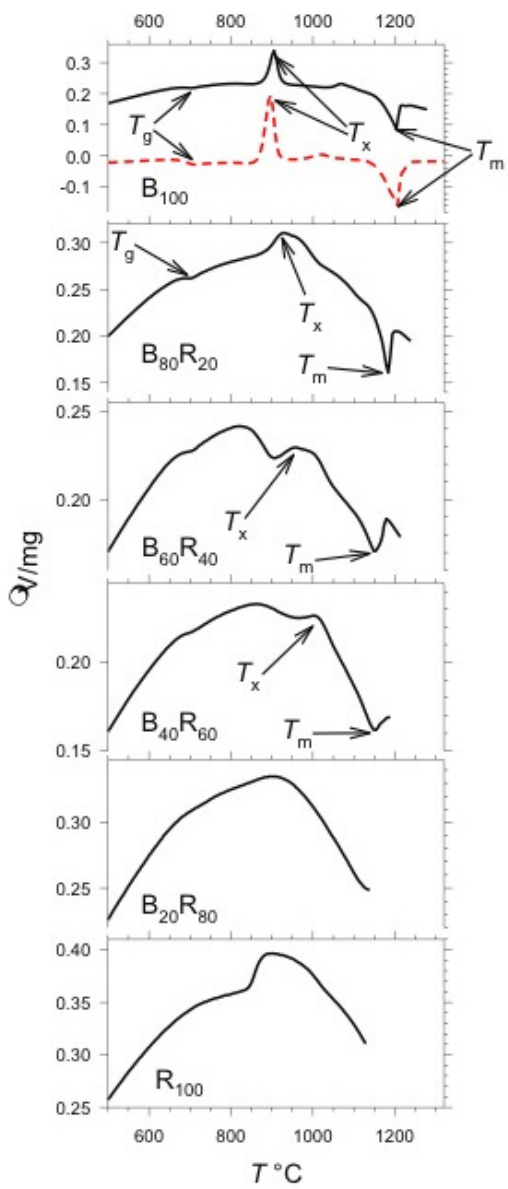

Fig. 1 I DSC spectra of the six glasses heated at 10 °C/min. All glasses were measured using alumina holders, except the B100 measured either in Pt (dashed red line) and alumina sample holders. The glass transition, onset of crystallization and melting temperatures (Tg, Tx and Tm, respectively) are indicated by arrows. The B20-R80 and R100 compositions do not shown any peak. From B100 down to B40R60 the peaks are progressively less prominent.

DSC thermograms are reported in Fig. 1; peaks related to Tg, Tx and Tm temperatures are marked by arrows. R100 and B20R80 spectra do not show any peaks, whereas B100, B80R20, B60R40 and B40R60 show peaks that are progressively less prominent (Fig. 1); the B100 spectra collected with Pt (red line) and Al_2O_3 sample holders show different resolutions.

Phase assemblages of B100 (top row) to B40R60 (last row) are displayed in Fig. 2. In agreement with DSC

data, the amount of glass (gl) increases, whereas that of clinopyroxene (cpx) decreases from B100 to B40R60, whereas R100 and B20R80 are completely glassy; the amount of spinel (sp) is invariably a few area%. Plagioclase crystallises heterogeneously only on the alumina sample holders in B100 and B80R20. R100 and B20R80, B40R60 and B60R40 glasses have oxides equal to their starting compositions in agreement with the absence of crystals or very low crystallization during heating. Instead, B100 and B80R20 glasses are enriched in Si, Al and Na and depleted in Fe, Mg and Ca due to significant crystallization of sp (spinel) and mostly cpx. Cpx in B100 is relatively rich in Ca and Mg.

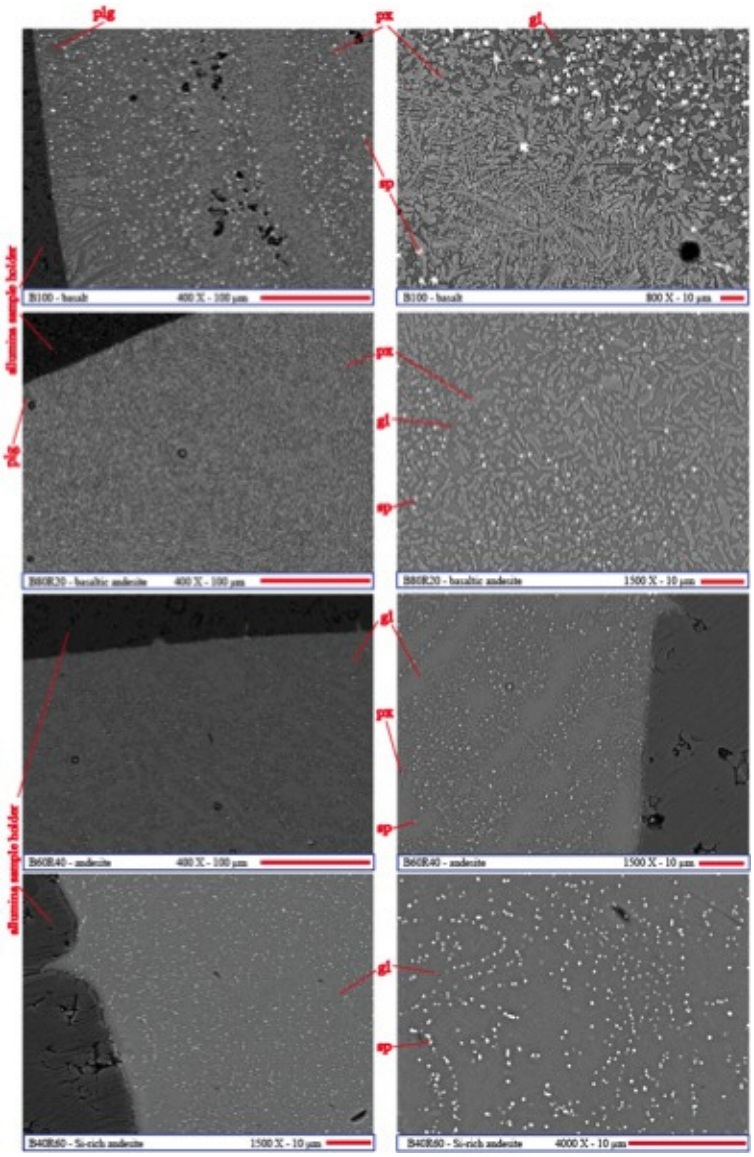

Fig. 2 I Phase assemblages by FE-SEM images of run-products heated at 10 °C/min in alumina sample-holders. From B100 (top row) to B40R60 (last row) the amount of glass (gl) increases, whereas that of pyroxene (px) decreases; the amount of spinel (sp) is invariably few area%. Plagioclase crystallises heterogeneously only on the alumina sample holders in B100 and B80R20.

Reconstruction of magmatic variables governing recent Etnean eruptions: constraints from mineral chemistry and P-T-fO_2-H_2O modelling

S. Mollo, P.P. Giacomoni, M. Coltorti, C. Ferlito, G. Iezzi, P. Scarlato

Research Line V3

Petrological investigations of active volcanoes are often supported by mass balances, thermodynamic calculations and/or experiments performed at key conditions. Conversely, the compositions of mineral phases found in natural products are generally used as input data for predictive models calibrated to derive the intensive variables of the magmatic system.

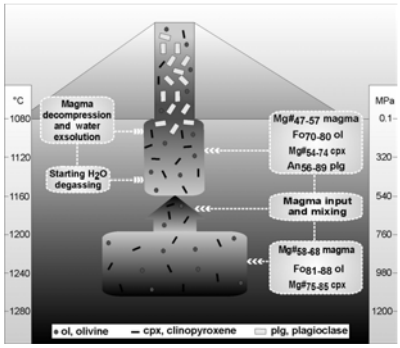

Fig. 1 I Schematic representation of T-P paths driving the crystallization ofmagmas atMt. Etna. Primitive basalts crystallizeMg-rich olivine and clinopyroxene at 600–1100 and 1150–1250 °C. Conversely, evolved trachybasalticmagmas equilibratewithMg-poormafic phenocrysts at 0.1–500 MPa and 1050–1175 °C. Most of the crystallization of plagioclase occurs at shallow levels and in the conduit due to the effect of water degassing and magma decompression.

In order to evaluate the extent to which mineral chemistry records crystallization conditions, we have compared the compositions of olivine, clinopyroxene, plagioclase and titanomagnetite in 2001-2012 trachybasaltic lavas at Mt. Etna with those obtained through thermodynamic simulations and experiments conducted under anhydrous, water-undersaturated and water-saturated conditions.

This systematic comparison allows us to track recent differentiation processes beneath Mt. Etna, as well as the P-T-fO_2-H_2O variables controlling the solidification path of magma. Two compositionally distinct populations of olivine and clinopyroxene phenocrysts are found in these lavas: Mg-rich and Mg-poor minerals formed at 600-1100 MPa and 1100-1250 °C, and 0.1-500 MPa and 1050-1175 °C, respectively. The oxygen fugacity varies by 1-2 log units suggesting water exsolution during magma ascent in the conduit and magma emplacement near the surface.

The nucleation and growth of normally zoned plagioclases occurs at P <100 MPa, when the amount of H_2O dissolved in the melt abruptly decreases from about 3.0 to 0.2 wt.% due to magma decompression and degassing. This leads to the conclusion that Etnean magmas fractionate throughout the entire length of the vertically developed plumbing system where magma mixing, volatile exsolution and degassing are the most important processes driving eruptions (Fig. 1).

Clinopyroxene and titanomagnetite cation redistributions at Mt. Etna volcano (Sicily, Italy): Footprints of the final solidification history of lava fountains and lava flows

S. Mollo, P.P. Giacomoni, D. Andronico, P. Scarlato

Research Line V3

For a better understanding of the final solidification history of eruptions at Mt. Etna volcano (Sicily, Italy), we have investigated cation redistributions at the interface between sub-millimetre-sized clinopyroxene and titanomagnetite crystal rims and coexisting melts. The studied products were scoria clasts from lava fountains and rock samples from pahoehoe and aa lava flows. Our data indicate that scoria clasts from lava fountaining were rapidly quenched at the contact with the atmosphere, preserving the original crystal textures and compositions inherited during magma dynamics within the plumbing system. Kinetics and energetics of crystallization were instantaneously frozen-in and post-eruptive effects on mineral chemistry were negligible. The near-equilibrium compositions of clinopyroxene and titanomagnetite indicate that lava fountain episodes were supplied by high-temperature, H_2O-rich magmas ascending with velocities of 0.01–0.31 m/s. In contrast, magmas feeding lava flow eruptions underwent a more complex solidification history where the final stage of the crystal growth was mostly influenced by volatile loss and heat dissipation at syn- and post-eruptive conditions. Due to kinetic effects associated with magma undercooling, clinopyroxenes and titanomagnetites formed by crystal attachment and agglomeration mechanisms leading to intricate intergrowth textures. The final compositions of these minerals testify to closure temperatures and melt–water concentrations remarkably lower than those estimated for lava fountains. Kinetically-controlled cation redistributions at the crystal–melt interface suggest that the solidification of magma was driven by degassing and cooling processes proceeding from the uppermost part of the volcanic conduit to the surface (Fig. 1).

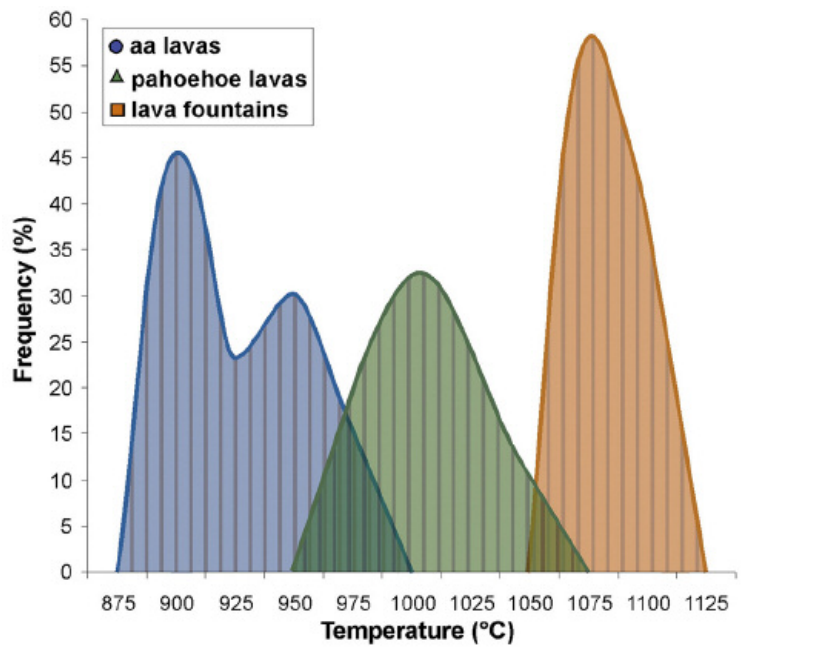

Fig. 1 I Crystallization temperatures of lava fountains, aa and pahoehoe lavas estimated through the P- and H_2O-independent thermometer of Putirka et al. (1996).

A K-feldspar–liquid hygrometer specific to alkaline differentiated magmas

S. Mollo, M. Masotta, F. Forni, O. Bachmann, G. De Astis, G. Moore, P. Scarlato

Research Line V3

We present a K-feldspar–liquid hygrometer specific to alkaline differentiated magmas that is calibrated through the regression analysis of sanidine and anorthoclase crystals coexisting with trachyte and phonolite melts. Partial-regression leverage plots were used to determine the minimum number of regression parameters that closely

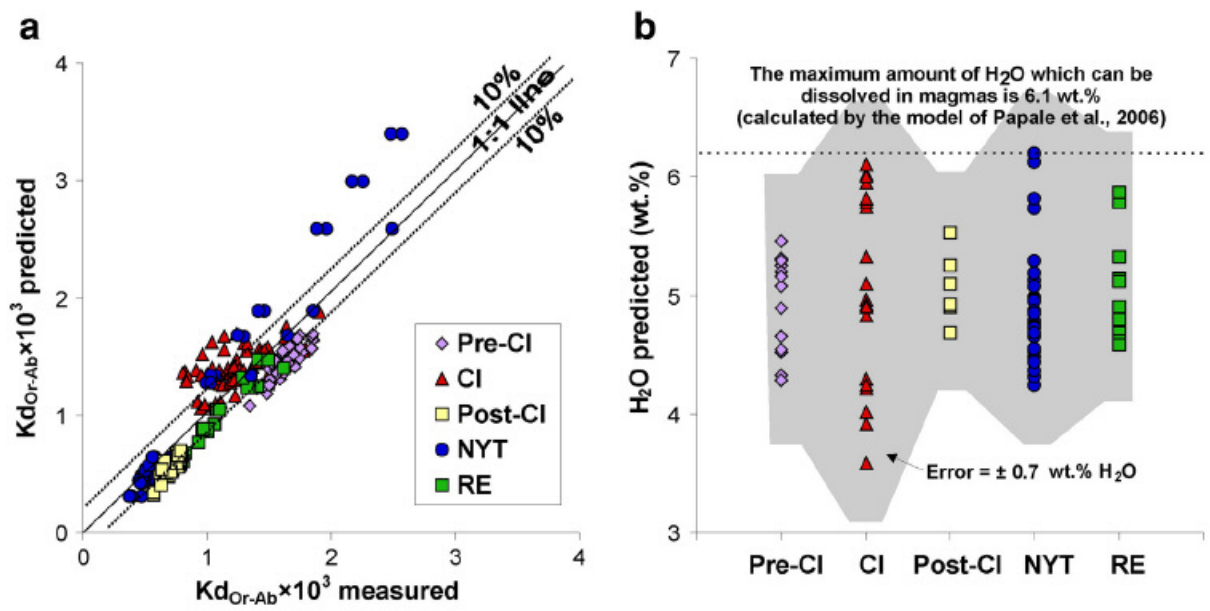

Fig. 1 | K-feldspar–liquid pairs from products of the Phlegrean Fields were used as input data for our new models. First, we have tested for equilibrium assuming as reliable the compositions plotting within 10% of the one-to-one line and yielding almost constant H_2O predictions (a). Second, after the screening of disequilibrium data, we have used the hygrometer to estimate the melt-H_2O content (b). Our estimates are consistent with results from H_2O solubility modeling and a number of previous melt inclusion data measuring comparable H_2O concentrations for both primitive and more evolved magmas. Pre-CI: pre-Campanian Ignimbrite eruptions. CI: Campanian Ignimbrite eruption. Post-CI: post-Campanian Ignimbrite eruptions. NYT: Neapolitan Yellow Tuff eruption. RE: recent eruptions.

describe the variance of the dataset. The derived model was tested using K-feldspar–liquid pairs not included into the calibration dataset in order to address issues of systematic errors. When K-feldspar and plagioclase crystals coprecipitate from the same alkaline liquid under identical P-T-X-fO_2-H_2O conditions, the ability prediction of the new hygrometer is comparable to that of previous plagioclase–liquid models. To minimize the error of H_2O estimate caused by the inadvertent use of disequilibrium data in natural samples, we have also calibrated a new test for equilibrium based on Or–Ab exchange between K-feldspar and coexisting melt. As an immediate application for both equilibrium and hygrometer models, we used as input data K-feldspar–liquid pairs from alkaline explosive

eruptions at the Phlegrean Fields. The estimates of H_2O dissolved in natural trachyte and phonolite magmas closely match those determined by melt inclusion analysis and H_2O solubility modeling. This leads to the conclusion that our new models can significantly contribute to a better quantitative characterization of the H_2O content in differentiated alkaline magmas feeding large-volume explosive eruptions (Fig. 1).

Experimental constraints on the origin of pahoehoe cicirara lavas at Mt. Etna Volcano (Sicily, Italy)

F. Vetere, S. Mollo, P. P. Giacomoni, G. Iezzi, M. Coltorti, C. Ferlito, F. Holtz, D. Perugini, P. Scarlato

Research Line V3

We present results from phase equilibria experiments conducted on the most primitive pahoehoe cicirara trachybasaltic lava flow ever erupted at Mt. Etna Volcano. This lava is characterized by a pahoehoe morphology in spite of its high content of phenocrysts and microphenocrysts (>40 vol%) with the occurrence of centimetre-sized plagioclases (locally named cicirara for their chick-pea-like appearance). Our experiments have been performed at 400 MPa, 1100–1150 °C and using H_2O and CO_2 concentrations corresponding to the water-undersaturated crystallization conditions of Etnean magmas. Results show that olivine does not crystallize from the melt, whereas titanomagnetite is the liquidus phase followed by clinopyroxene or plagioclase as a function of melt–water concentration. This mineralogical feature contrasts with the petrography of pahoehoe cicirara lavas suggesting early crystallization of olivine and late formation of titanomagnetite after plagioclase and/or in close association with clinopyroxene. The lack of olivine produces MgO-rich melt compositions that do not correspond to the evolutionary behaviour of cicirara magmas. Moreover, in a restricted thermal path of 50 °C and over the effect of decreasing water concentrations, we observe abundant plagioclase and clinopyroxene crystallization leading to trace element enrichments unlikely for natural products. At the same time, the equilibrium compositions of our mineral phases are rather different from those of natural cicirara phenocrysts and microphenocrysts. The comparison between our water-undersaturated data and those from previous degassing experiments conducted on a similar Etnean trachybasaltic composition demonstrates that pahoehoe cicirara lavas originate from crystal-poor, volatile-rich magmas undergoing abundant degassing and cooling in the uppermost part of the plumbing system and at subaerial conditions where most of the crystallization occurs after the development of pahoehoe surface crusts (Fig. 1).

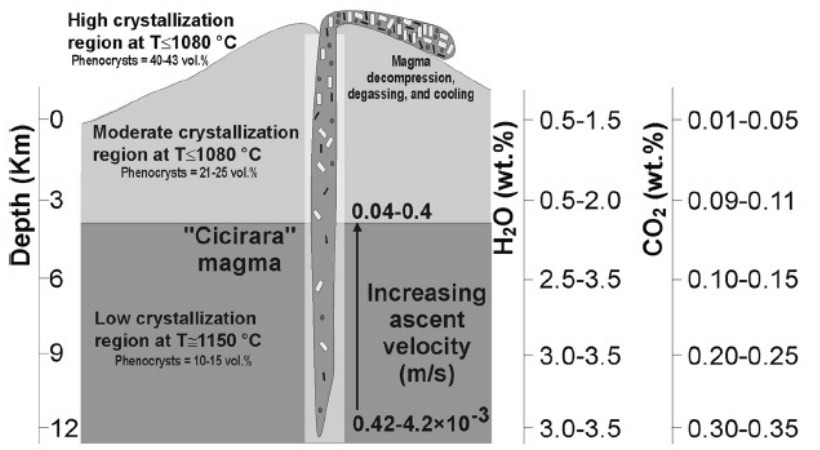

Fig. 1 I Schematic representation of magma dynamics driving the crystallization of cicirara magmas at Mt. Etna Volcano. The crystallization proceeds from a first region at depth where high-temperature, volatile-bearing magmas rise with low ascent velocities to a second shallow region where low-temperature, degassing magmas are rapidly erupted onto the surface.

The geological CO_2 degassing history of a long-lived caldera

G. Chiodini, L. Pappalardo, A. Aiuppa, S. Caliro

Research Line V2

The majority of the ~100 Holocene calderas on Earth host vigorously active hydrothermal systems, the heat and volatile budgets of which are sustained by degassing of deeply stored magma. Calderas may thus contribute a nontrivial, although poorly quantified, fraction of the global budget of magmatic volatiles such as CO_2. Here we use original isotopic and pet- rological results from Campi Flegrei volcano, Italy, to propose that hydrothermal calcites are natural mineral archives for the magmatic CO_2 that reacted with reservoir rocks during the geological history of a caldera. We show that Campi Flegrei calcites, identified in core samples extracted from 3-km-deep geothermal wells, formed at isotopic equilibrium with magmatic fluids having $\delta^{18}OH_2O$ of +8.7‰ to +12.7‰, and $\delta^{13}CCO_2$ of ~–1.5‰. This inferred fossil fluid composition is virtually identical to that of present-day fumaroles, demonstrating a stable carbon source during the caldera's (<40 k.y.) history. We use the mass of calcites stored in the hydrothermal system to estimate that 12 Gt of magmatic CO_2 reacted with the Campi Flegrei rocks during the caldera history; this corresponds to a time-averaged CO_2 flux of ~800 t d^{-1}. This long-term CO_2 flux, the first of its kind in the geological literature, is similar to the present-day soil CO_2 degassing flux (1100 ± 200 t d^{-1}). We conclude that the actual magmatic CO_2 degassing flux from calderas may be severely underestimated if subsurface calcite pre- cipitation is not taken into account (Fig. 1).

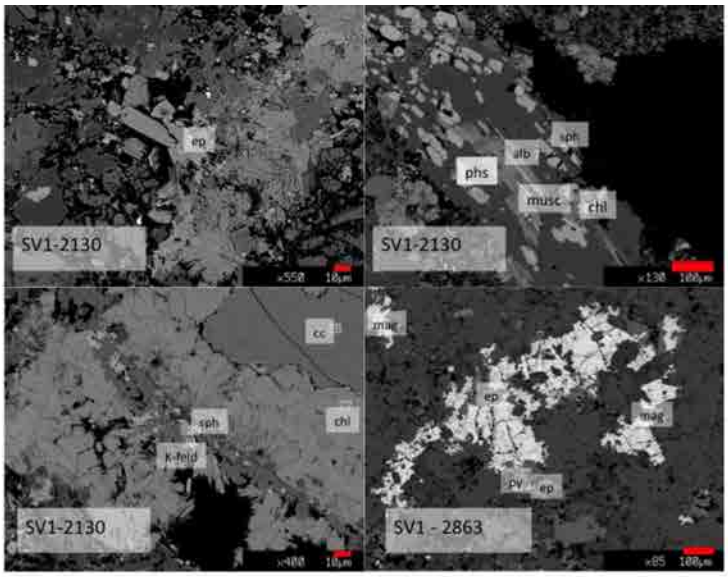

Fig. 1 I Examples of back-scattered electron images of polished thin sections representative of samples from studied wells.

Nanomechanical characterisation of k-basalt from roman comagmatic province

D. Passeri, V. Misiti, M. Rossi, A. Cavallo, M. Natali, A. Bettucci

Research Line V3

The possibility of performing multiscale mechanical characterization of K-basalt from Roman Comagmatic province has been investigated in collaboration with EMiNa research group (Department of Basic and Applied Sciences for Engineering, Sapienza University of Rome) supervised by Prof. Marco Rossi, using also the facilities available at Sapienza Nanotechnology and Nanoscience (SNN) Lab of CNIS (Center of Nanotechnology applied to the Engineering). Preliminary tests consisting in the acquisition of semi-quantitative nanomechanical images and single-point measurements of indentation modulus have been carried out through contact resonance atomic force microscopy (CR-AFM). In CR-AFM the tip is in contact with the sample surface, which is set into out-of-plane oscillation at ultrasonic frequencies through a piezoelectric transducer coupled to the back of the sample. The sample elastic properties determine the cantilever resonance frequencies that can be detected and used to evaluate the indentation modulus of the sample.

In correspondence of regions of the sample with uniform mechanical properties, the indentation modulus has been evaluated as high as 72 GPa, using a Suprasil glass as a reference. This value was found in good agreement with the bulk indentation modulus of the same sample measured as high as 67 ± 5 GPa by a pulse-echo methods, in collaboration with the laboratory of Acoustical Physics (Department of Basic and Applied Sciences for Engineering, Sapienza University of Rome) supervised by Dr. Andrea Bettucci.

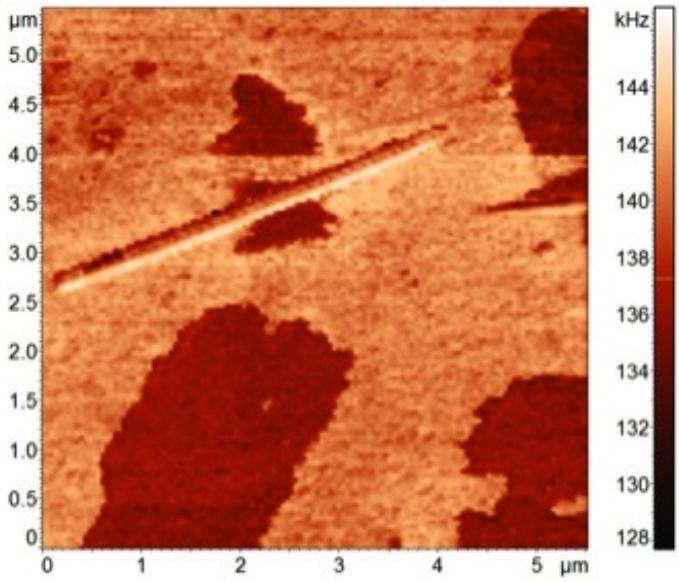

Fig. 1 I CR-AFM map of an area of the K-basalt from Roman Comagmatic province, revealing the not uniform local mechanical properties..

Preliminary CR-AFM images of the samples revealed the presence of areas with not homogeneous mechanical properties. In particular, a stiffer matrix seems to incorporate areas with reduced elastic modulus (Fig. 1). This could be compatible with the presence of subsurface voids, which are responsible for the reduction of the apparent elastic modulus, as well as of surface contaminant layers. Further studies are ongoing to clarify these results.

Characterization of volcanic plume dynamics using high-speed imagery

P. Y. Tournigand, J. Taddeucci, P. Scarlato, D. Gaudin, E. Del Bello

Research Line V3

Parameterizing the physical processes responsible for ash injection and plume dynamics is crucial to constrain numerical models and forecasts of potentially hazardous ash dispersal events. We present results from a new method based on visible and thermal high-speed video processing from unsteady plumes. High speed cameras allow us to identify different dynamics of ash injection and dispersal, and the different phases during volcanic plume dispersion with a time resolution down to 1 ms. The use of this tool allow us to be more accurate with our observations and to better define already studied features and new ones. Quantitatively pre-processing of our records was performed in order to highlight the volcanic plume from the background by using different types of filters without altering the data, to allow us to use manual and automated procedures to track volcanic plumes. We extracted data

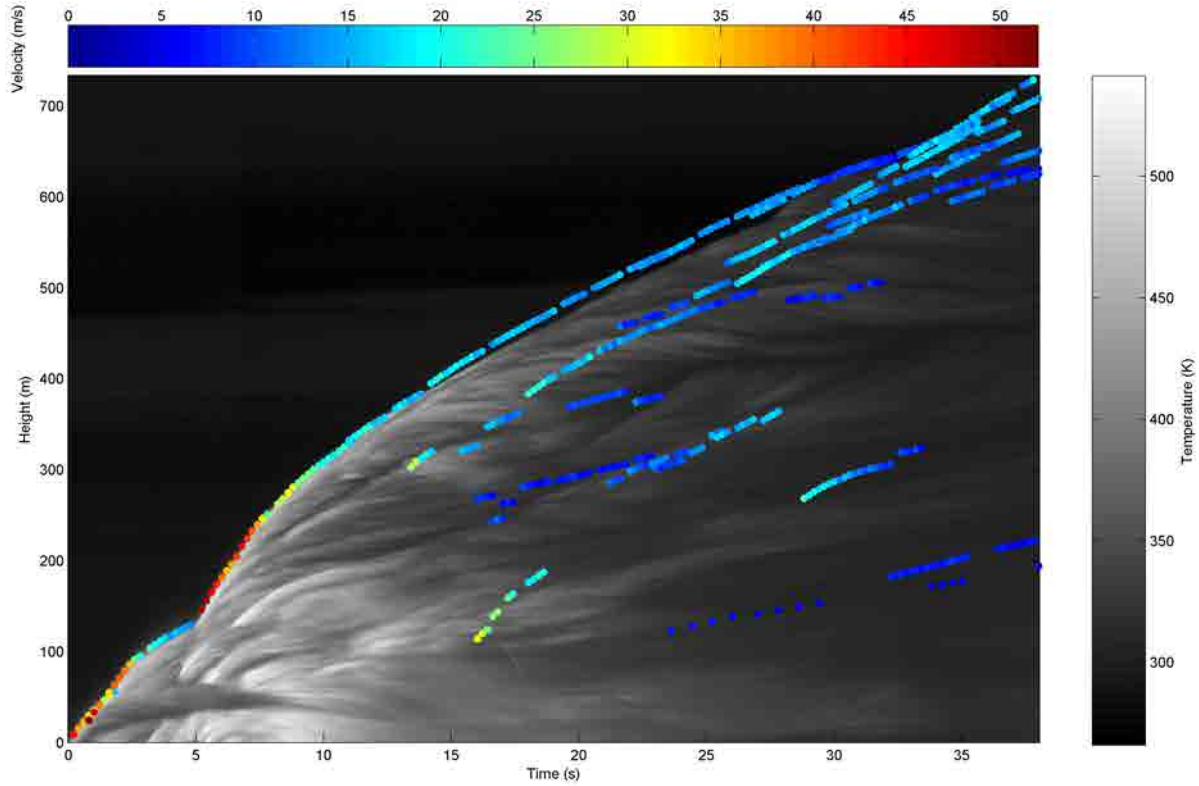

Fig. 1 I Evolution of plume height (m), velocity (m/s) and temperature (K) over time for one explosion from Sakurajima volcano, Japan.

from these videos (plume high, velocity, temperature, mass, volume,...) using different software in function of the parameter expected (Fig. 1). Doing this allows us to be able to define and constrain the main parameters and processes, and to define eruptions and explosions types, but also to find correlations between parameters and establish

empirical relations. Figure 1 shows Sakurajima's plume evolution over time in terms of height, velocity and temperature. The link between these parameters is observable in this case. High plume velocities are measurable at the very beginning of the explosion and at low height, these velocities decrease with time before increasing again around 5 seconds, if we consider also the temperature we observe that it is following exactly the same trend over time. It shows that this explosion can be subdivided in two phases corresponding to a first release of material and gas, followed by a second pulse (occurring potentially around 3 s after the onset of the first one, following the temperature data slope). The velocities are manually tracked in this case and correspond to the front of the plume but also to eddy all over the plume. This gives the possibility to consider different parts of the plume and to compare them, to better understand dynamical similarities and differences between each of them. Using this method, we defined range of values for each parameter and their respective impact on plume dynamics and stability, to be able to obtain characteristic fields of values for each case and link it to explosions type and evolution. Doing this allowed us to highlight different explosions types in between volcanoes but also for a same volcano.

Retrieving eruptive vent conditions from dynamical properties of unsteady volcanic plume using high-speed imagery and numerical simulations

P. Y. Tournigand, J. Taddeucci, J. J. Peña Fernandez, D. Gaudin, J. Sesterhenn, P. Scarlato, E. Del Bello

Research Line V3

Vent conditions are key parameters controlling volcanic plume dynamics and the ensuing different hazards, such as human health issues, infrastructure damages, and air traffic disruption. Indeed, for a given magma and vent geometry, plume development and stability over time mainly depend on the mass eruption rate, function of the velocity and density of the eruptive mixture at the vent, where direct measurements are impossible. High-speed imaging of eruptive plumes and numerical jet simulations were here non-dimensionally coupled to retrieve eruptive vent conditions starting from measurable plume parameters. High-speed videos of unsteady, momentum-driven volcanic plumes (jets) from Strombolian to Vulcanian activity from three different volcanoes (Sakurajima, Japan, Stromboli, Italy, and Fuego, Guatemala) were recorded in the visible and the thermal spectral ranges by using an Optronis CR600x2 (1280x1024 pixels definition, 500 Hz frame rate) and a FLIR SC655 (640x480 pixels definition, 50 Hz frame rate) cameras. Atmospheric effects correction and pre-processing of the thermal videos were performed to increase measurement accuracy. Pre-processing consists of the extraction of the plume temperature gradient over time, combined with a temperature threshold in order to remove

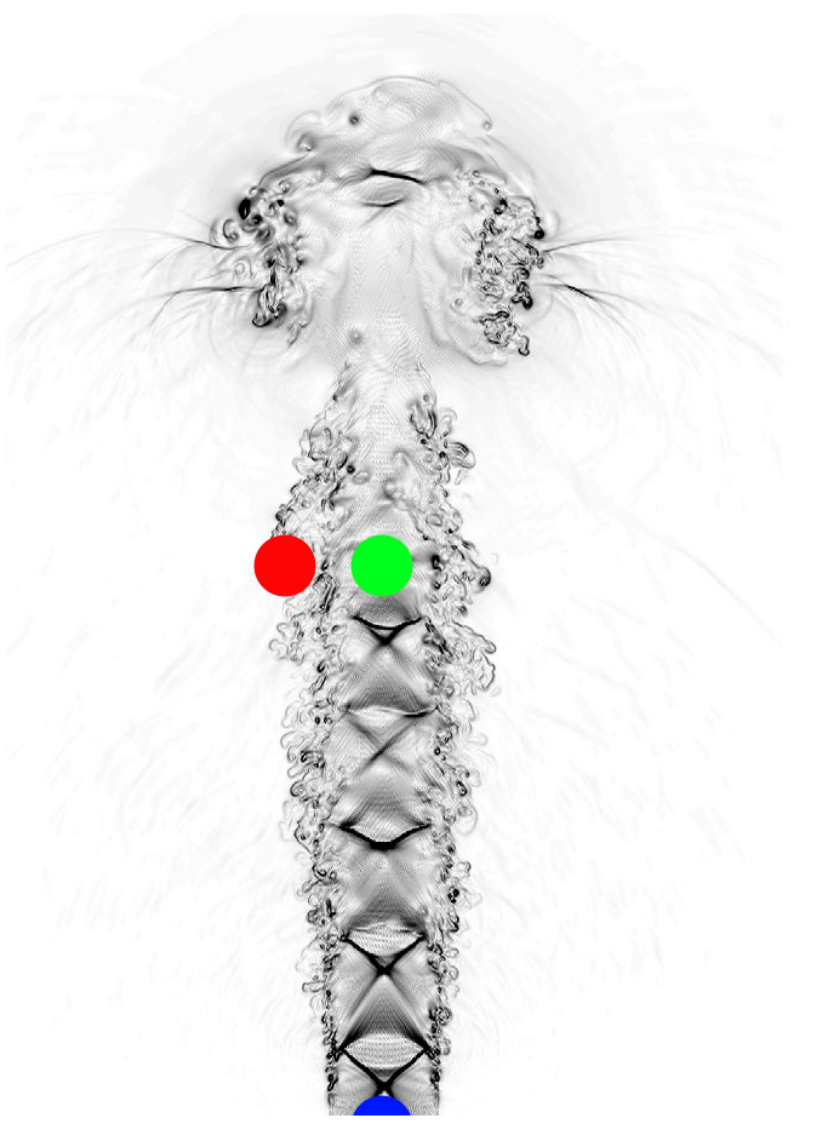

Fig. 1 | Numerical simulation of jet. We can observe different parts of the jet such as the boundary shear layer (red point), the centerline (green point) and the vent (blue point).

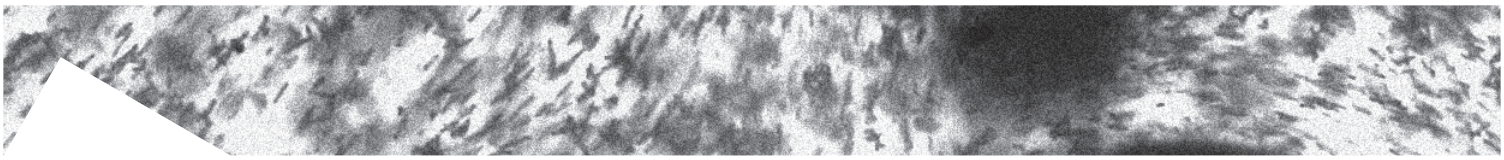

the image background. The velocity and the apparent surface temperature fields of the plumes, and their changes over timescales of tenths of seconds, were then measured by particle image velocimetry and thermal image analysis, respectively, of the pre-processed videos (Fig. 1). The parameters thus obtained are representative of the outer plume surface, corresponding to its boundary shear layer at the interface with the atmosphere, and may significantly differ from conditions in the plume interior. To retrieve information on the interior of the plume, and possibly extrapolate it even at the eruptive vent level, video-derived plume parameters were non-dimensionally compared to the results of numerical simulations of momentum-driven gas jets impulsively released from a vent in a pressurized container. These simulations solve flow conditions globally, thus allowing one to set empirical relations between flow conditions in different parts of the jet, most notably the shear layer, the flow centerline, and at the vent (Fig. 2). Applying these relations to the volcanic cases gives access to the evolution of velocity and temperature at the vent. From these, the speed of sound and flow Mach number can be obtained, which in turn can be used to estimate the pressure ratio between atmosphere and vent and finally, assuming some conduit geometry and mixture density, the total amount of erupted gas. Preliminary results suggest subsonic exit velocities of the eruptive mixture at the vent, and a plume centerline velocity that can be twice as fast as the one measured at the plume boundary.

High-speed imaging of lava lake activity at Kilauea

J. Taddeucci, B. Houghton, P. Scarlato, D. Gaudin, E. Del Bello, T. Orr

Research Line V3

In December 2015 laboratory representatives participated in a NSF-sponsored multidisciplinary field campaign at the active lava lake hosted in the Halema'uma'u crater of Kilauea volcano, Hawaii. This field campaign hosted scientists from several different institutions from, US, Europe and Oceania. Deployed instruments included UV, thermal and visible cameras, gas sensors and acoustic sensors.

Within this campaign the FAMoUS toolbox of the laboratory was deployed, including, beside the Optronis and FLIR cameras, the two new GRAS microphones. The new high-speed camera NAC HX-6 was also deployed and synchronized with the other equipments, allowing a two-fold increase in the spatial and temporal resolution of the acquired images. In addition one of the new Sony 4K camcorder was also deployed, continuously filming with the broadest field of view and the best spatial resolution. The joint data acquisition will allow for a truly multiscale-multidimensional analysis of key dynamic processes like, e.g., bubble burst, pyroclasts formation, and lava lake motion.

Fig. 1 I The INGV team and their international colleagues on the edge of the Halema'uma'u crater of Kilauea volcano, Hawaii. Part of the deployed instruments are visible, pointing downward towards the lava lake.

On the role of sulfur in explaining different degassing patterns in volcano-hydrothermal systems

T. Scolamacchia, V. Misiti, P. Del Gaudio, A. Cavallo, P. Scarlato

Research Line V3

Understanding the solubility behaviour of sulphur in silicate melts is complex due to its multiple valence states and the possible occurrence of non-volatile S-rich phases. The assessment of the total mass fraction of S dissolved in the pre-eruptive gas-phase has always been a critical topic in an attempt, among other issues, to forecast the amount of SO_2 released by explosive eruptions and its impact on the climate. Several eruptions released SO_2 amounts orders of magnitude greater than those possibly dissolved in melts, unearthing the "excess-S" problem. The source of anomalous SO_2 emissions could be instead explained with a contribution from S stored in hydrothermal systems, without needing evidences for a gas saturation of magmas. In fact, S-layers have been reported at several active volcanoes hosting hydrothermal systems (i.e. Ruapehu, Poás, Kusatzu Shirane and recently inferred at El Chichón and Ilamatepec). S-layers may be more frequent that commonly thought.

Bacon and Fanelli (1943) noted variations in viscosity of S in the presence of impurities using capillary methods. Even if innovative in the 40's, their experimental results need a validation using other experimental approaches. With modern thermocouples and automated viscometers, we can improve the precision of the measurements, with other conditions that more closely replicate the volcanic system. Moreover, also the sample size can be reduced to perform analyses allowing performing more experiments with a reduced amount of raw material.

We want to understand if the variations in sulfur viscosity when impure, and following the addition of different species can explain the different passive degassing patterns observed at several active volcanoes

The results expected would offer a tool to understand the role of such element in "modulating" passive emissions, and contribute to clarify controversial aspects related to anomalous high- SO_2 emissions in explosive eruptions.

We are investigating the variations in S-viscosity at T and P typical of volcanic hydrothermal systems (ranging from few ten of meters as in Ruapehu up to few kilometer as in Phlegrean Fields), using a rheometer equipped with a pressure cell and a piston cylinder respectively. Steel geometries of rheometer are substituted by Plexiglass ones because of potential contamination of the device. Investigated samples are natural samples collected at Kawah Ijen (Indonesia) and at Solfatara (Phlegrean Fields).

Samples images have been recorded by FE-SEM, while chemical analyses have been done by EPMA at the Istituto Nazionale di Geofisica e Vulcanologia. SEM images related to Kawah Ijen sulfur spherules sample, while chemical analyses belong to Solfatara crater in the Phlegrean fields.

Bubble bursts in mud: insights from laboratory experiments

M. Edwards, B. Kennedy, A. Jolly, B. Scheu, P. Jousset, J. Taddeucci

Research Line V3

Phreatic eruptions are common in the recorded history of White Island, New Zealand. Although the larger eruptions have been described in literature, little attention has yet been given to the smaller, more frequent phreatic activity. In addition, the style in which steam bubbles are released during phreatic eruptions at the surface can be highly variable and is poorly understood.

Experimental modelling of bubble bursts in mud was conducted in order to identify the influence of viscosity, bubble shape and depth on the White Island regimes. An analogue to the White Island mud was created by mixing of

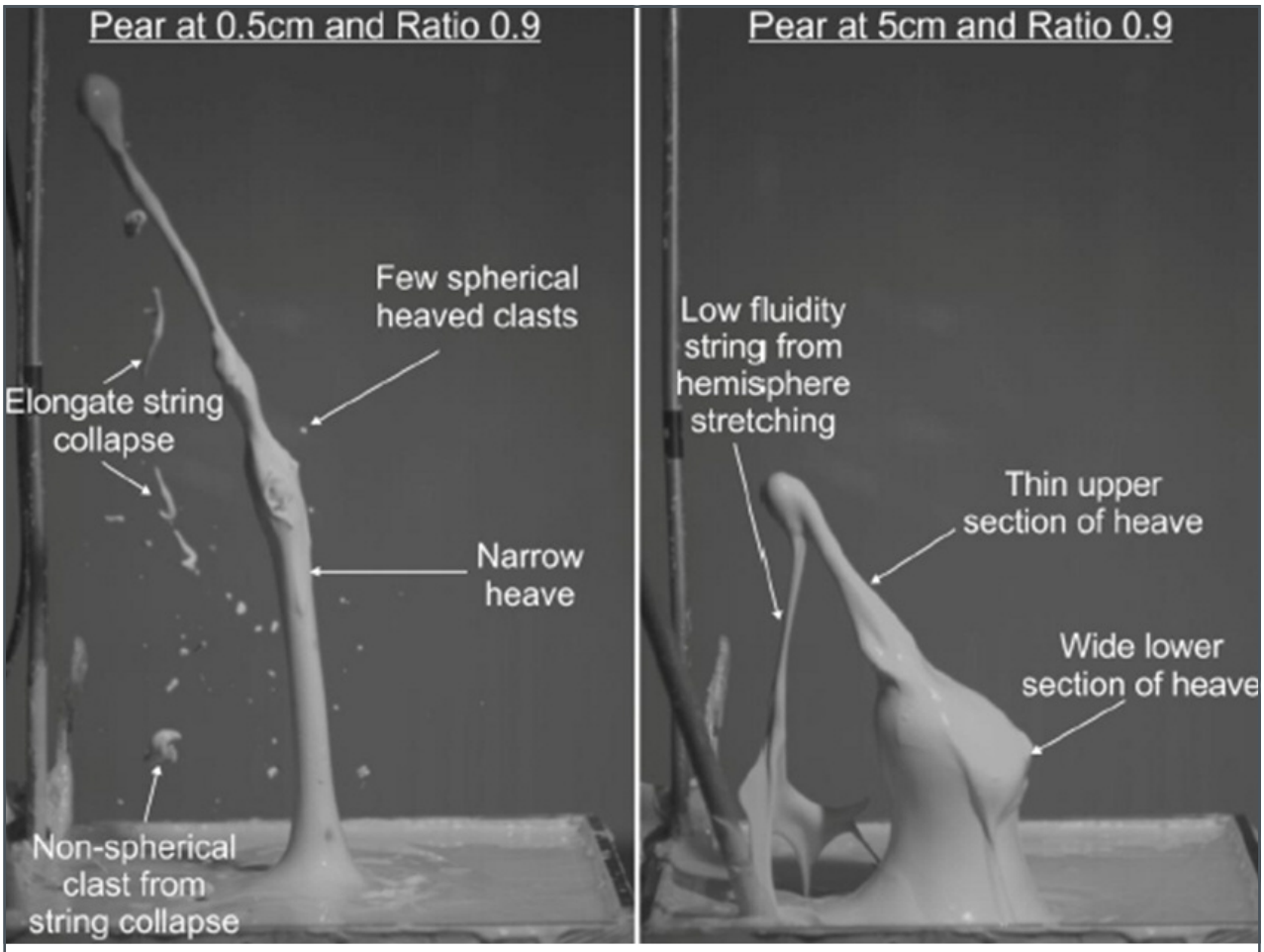

Fig. 1 I Example of bursting of pressurized balloons through kaolin-water suspensions.

kaolinite powder and water to controlled ratios. Bursts were performed at depths of 0.5, 5 and 10 cm in 9 different mud ratios corresponding to an increasing viscosity. Results of these experiments show that viscosity has a negative influence on heave heights but controls the transition from fluidal to brittle structures. Importantly, both a shal-

lowing of bubble depth and increase to bubble length are shown to increase the height of heaves. Here, increases to bubble length towards long, conduit-controlled slug-shaped bubbles is shown to be a possible mechanism for the increasing ejection heights. Decrease of the mud pool level by desiccation, results in shallower bubble depths, and is also considered to be an influence to the observed increased explosivity and more brittle behaviour of bubble bursts and mud heaves (Fig. 1).

Multiparametric study of Strombolian activity at Mt. Etna in 2014

J. Taddeucci, E. Del Bello, P. Scarlato, T. Ricci, D. Andronico, U. Kueppers, A. Cannata, L. Spina

Research Line V3

Seismic and acoustic surveillance is routinely performed at several persistent activity volcanoes worldwide. However, interpretation of the signals associated with explosive activity is still equivocal, due to both source variability and the intrinsically limited information carried by the waves. Comparison and crosscorrelation of the geophysical quantities with other information in general and visual recording in particular is therefore actively sought. In July 2014 Strombolianstyle explosive activity occurred at two adjoined vents formed along a new eruptive fissure. Visually, the activity appeared as shortlived explosions ejecting bomb to lapillisized, molten pyroclasts at a remarkably repeatable

Fig. 1 I Deployment of FAMUoS at Etna in July 2014.

time interval. The frequent occurrence and the highly repeatable nature of the explosions provided us with a rare occasion to systematically investigate the seismic and acoustic fields radiated by this common volcanic source. During July 15 and 16, 2014 we deployed FAMoUS (FAst, MUltiparametric Setup for the study of explosive activity) at about 300 meters from the vents, recording more than 60 explosions in thermal and visible highspeed videos (50 to 500 frames per second) and broadband seismic and acoustic instruments (1 to 10000 Hz for the acoustic and from 0.01 to 30 Hz for the seismic). Crosscorrelation of this data set help defining better the key monitoring parameters offered by the geophysical approach (e.g., ejected mass and velocity), also adding to our general understanding of the eruptive process (Fig. 1).

Solid solution along the $LiAlSi_2O_6$ – $LiFeSi_2O_6$ clinopyroxene join

G. Bromiley, A. Cavallo, F. Karavassili, I. Margiolaki, P. Pratim Das, A. Stewart, M. Tribaudino, J. Wright, G. Iezzi

Research Line V1

Seven clinopyroxene compositions along the join M2LiM1AlTSi$_2$O$_6$ (spodumene) to M2LiM1Fe^{3+}TSi$_2$O$_6$6 (ferri-spodumene) were synthesized at 2 GPa, 800 °C and very oxidized conditions (using H_2O_2 fluid) in an end-loaded piston cylinder. In addition, the LiFe^{3+}Si$_2$O$_6$ composition was also synthesized under reducing and intrinsic conditions of piston cylinder, to check the effect of fO_2 on iron speciation. The run-products were characterized by image analysis (area %) on FE-SEM micro-photographs, Rietveld refinements on XRPD synchrotron spectra and SAED-TEM patterns. Run-products are composed mainly of lithium clinopyroxene (Li-cpx), plus minor amounts of hematite (magnetite under reducing condition) and corundum, as independently detected by image analysis and Rietveld refinements (wt. %); moreover, Rietveld data were used to derive cell parameters, M1-site occupancy (Al vs Fe^{3+}), atomic positions and average bond lengths of all these Li-cpx indexed in the C2/c space groups according to SAED-TEM.

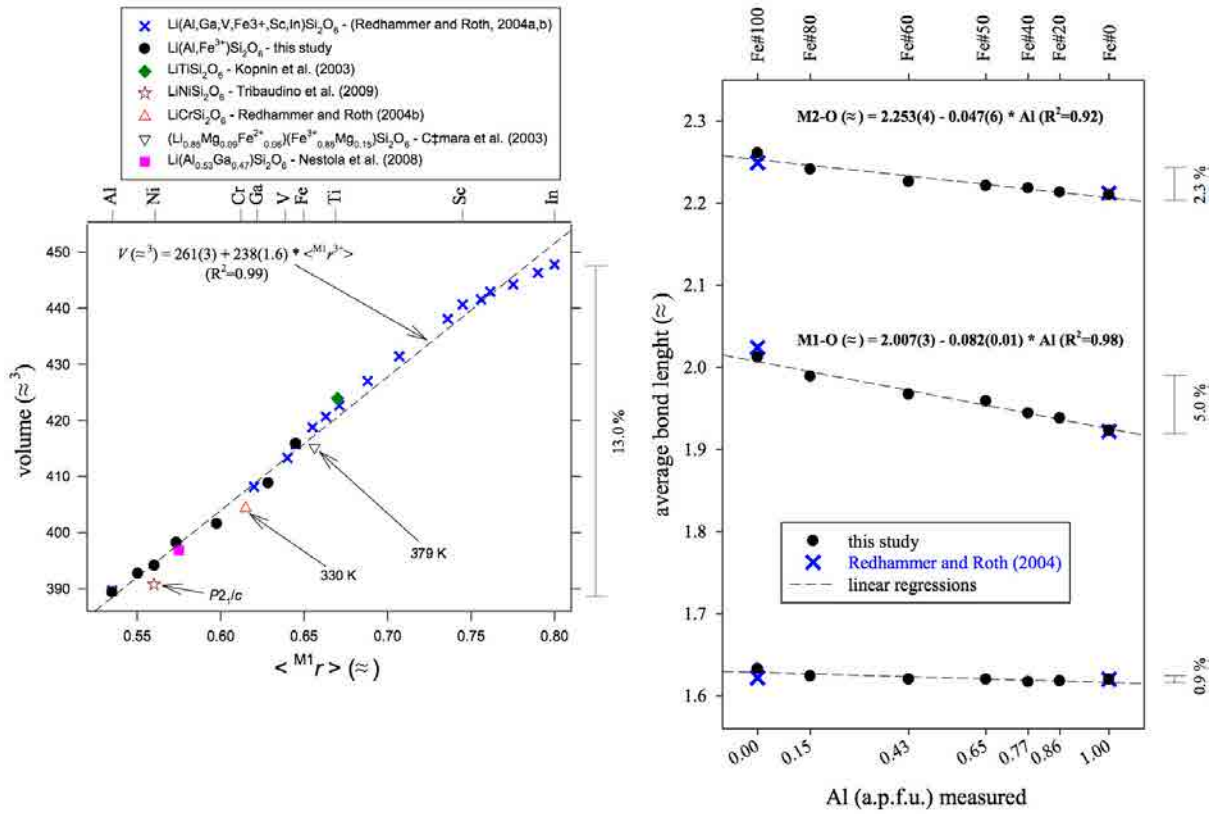

Fig. 1 | left) Evolution of cell volume at 298 K as a function of the average cation size at the M1-site of LiMe^{3+}Si$_2$O$_6$ clinopyroxenes; filled and open symbols are C2/c and P21/c (Tc are also reported), respectively. (right) Evolution of average bond lengths (top: M2-site, middle: M1-site, bottom: T-site) as a function of the M1Al (a.p.f.u.) measured by Rietveld refinements (black circles); the blue crosses are reported in comparison with our data (SC-XRD); the substitution of Al by Fe^{3+} at the M1-site mainly involves the M1-O, but also the M2-O average bond length is affected due to steric effects; T-site is only slightly modified. The relative variations (%) are calculated as: (max-min)/max.

Li-cpx with Al and Fe^{3+} amounts close to 50:50 are actually slight richer in Al a.p.f.u. than nominal; the $LiFe^{3+}Si_2O_6$ grown under very oxidized and reducing conditions have very similar cell parameters, indicating that fO_2 is unable to induce a significant incorporation of Fe^{2+} in these Li-cpx. The replacement of Al with Fe^{3+} induces a linear (%) increase of the cell edges following b > a > c, whereas β is roughly constant and the cell volume increases linearly (Fig. 1). Furthermore, the substitution of Al with Fe^{3+} only weakly affects the T-O average length (<1 %), whereas M2-O and M1-O bonds increase in a linear manner of 2.3 and 5.0 %, respectively (Fig. 1).

These data have been compared with other available in literature on Li-cpx, as well as Na and Ca-cpx, to model lattice strain, bond lengths, steric effects and phase transitions behaviors. The replacement of Al with a progressive large cations in $LiM^{3+}Si_2O_6$ cpx (M^{3+}, Ni, Cr, Ga, V, Fe^{3+}, Ti, Sc and In) determines a linear increasing following V > b > a > c, whereas β is roughly constant except for Ti-end-member and P21/c compositions (Fig. 1).

Lattice strains induced by X, T and P for Li-cpx in the C2/c stability field show that when M1-site is progressively filled with a large cation ε1 axis (ε1 > ε2 > ε3) along b increases, whereas ε2 and ε3 are nearly parallel to a and at about 30 ° from c; conversely, T will provoke a similar enlargement of ε1 and ε2 along b and a edges, respectively, whereas ε3 is again oriented at about 30 ° from c ; finally, the increasing of P will instead shorten all strain tensor components (ε1, ε2 and ε3) with a similar % amount; notably, high-P is the only stress that induces a strain component to be almost parallel to c edge.

Speciation and diffusion profiles of H_2O in water-poor beryl: comparison with cordierite

G. Della Ventura, F. Radica, F. Bellatreccia, C. Freda, M. Cestelli Guidi

Research Line V1

This paper reports on water speciation and diffusion in synthetic beryl samples treated in CO_2-rich atmosphere, at 700 MPa and 700°C and 800°C, respectively. The study has been conducted by means of polarized FTIR (Fourier Transform Infra Red) integrated with FPA (Focal Plane Array) imaging. As expected, the infrared spectra show the

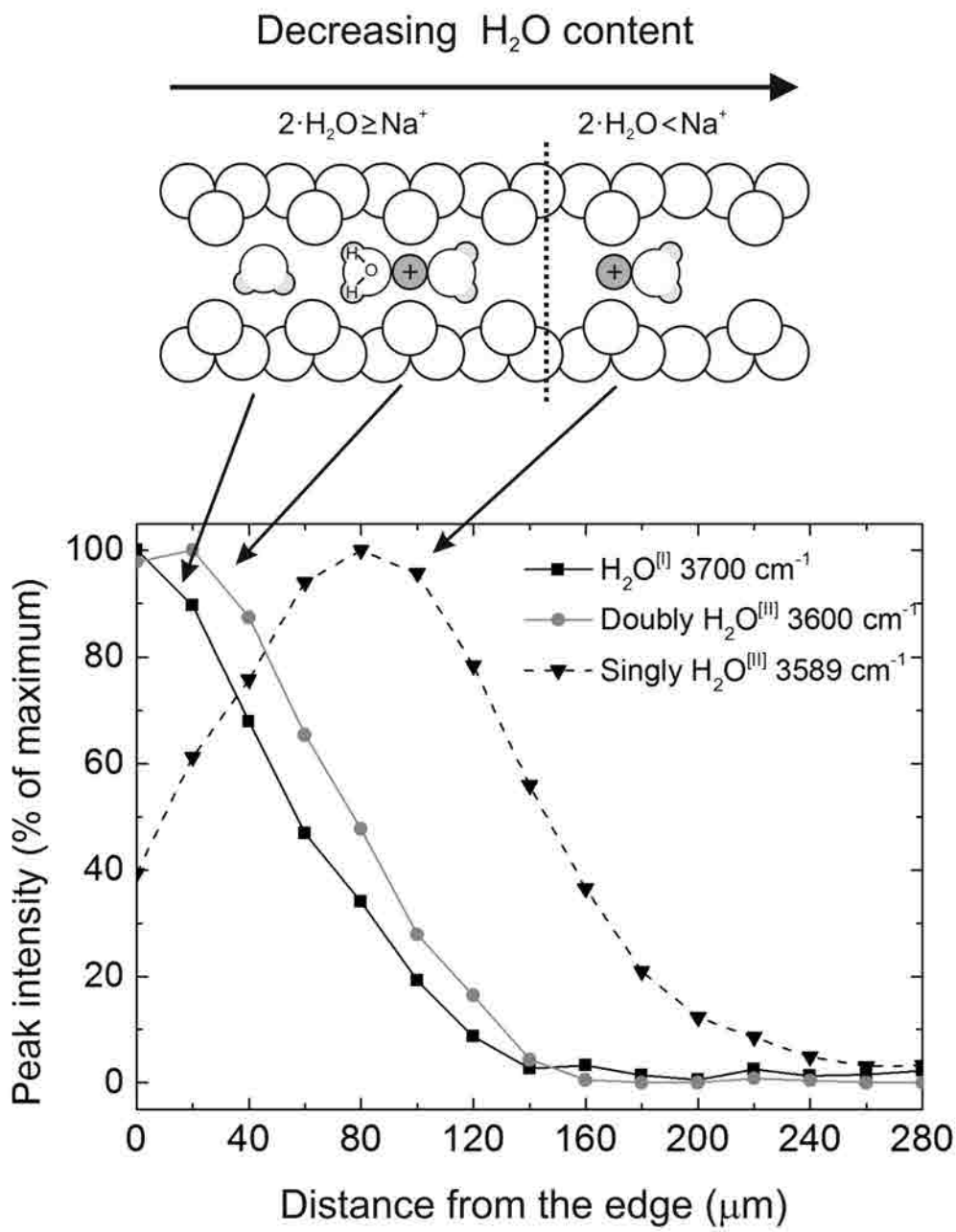

Fig. 1 | Schematic representation of the configuration of water molecules inside the structural channels of beryl, as the overall water content decreases. Bottom: concentration trends of selected peaks in the FTIR spectra. Peak intensities are scaled to the maximum intensity value.

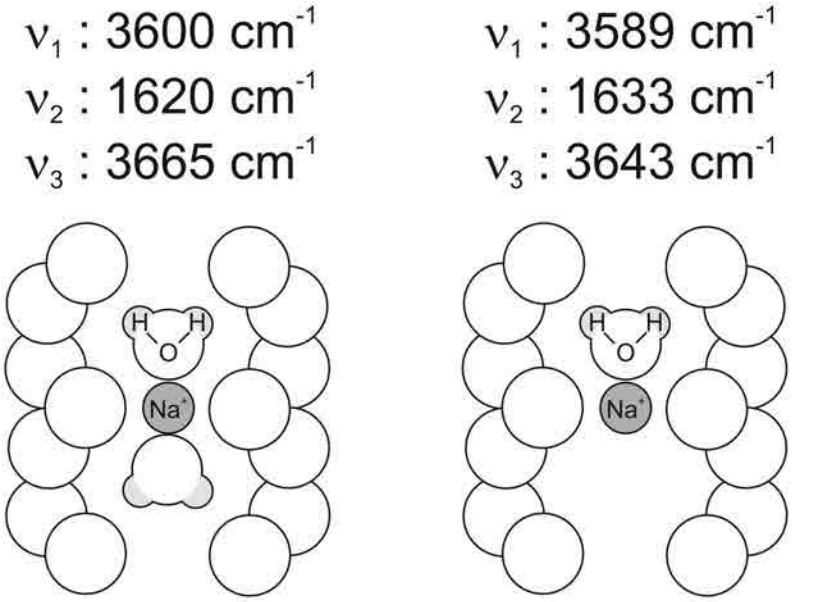

Fig. 1 I Schematic representation of the proposed band assignment for singly versus doubly coordinated type II water in beryl.

presence of CO_2 but also of minor H_2O, interpreted as resulting from moisture present in the starting materials used for the experiments. FPA-FTIR images show that H_2O diffuses into the beryl matrix along the structural channels oriented parallel to [001]. Spectra collected along profiles parallel to the c axis show subtle changes as a function of the distance from the crystal edge; these changes can be correlated to a progressive change in the H_2O coordination environment in the channel, as a response to the varying H_2O/alkali ratio. In particular, the data show that when $2 \cdot H_2O > Na+$ apfu (atoms per formula unit), H_2O can assume both type I and type II orientation; in the latter case, each Na cation coordinates two H_2O[II] molecules (doubly coordinated H_2O). If $2 \cdot H_2O < Na+$ apfu, then H_2O[II] molecules are singly coordinated to each Na cation. The same type of feature is observed and commented for the structurally related cordierite. Diffusion coefficients and activation energies have been also determined for both types of water molecules (Fig. 1 and 2).

Kinetics of incorporation of CO_2 in cordierite and beryl: an FTIR-FPA spectroscopy study

F. Radica, G. Della Ventura, F. Bellatreccia, C. Freda, M. Masotta, M. Cestelli Guidi, G. Cinque

Research Line V1

In this work, we address experimentally the diffusion of CO_2 into cordierite and beryl, two isostructural microporous rock-forming minerals, using FTIR spectroscopy coupled with FPA (focal-plane-array of detectors) imaging. Fragments of a natural, almost Mg end-member cordierite and CO_2-free synthetic beryl were used as starting materials; the cordierite crystallites were degassed before the experiments.

Starting crystals were treated in a CO_2-saturated atmosphere at different pressure, temperature and time conditions, using a non end-loaded piston-cylinder apparatus. Ag-carbonate was used as the source for carbon dioxide. After the high pressure experiments, the recovered crystals were oriented using a spindle stage, cut and doubly polished, and analyzed using polarized micro-FTIR spectroscopy to study the distribution of CO_2 across the sample and quantify its concentration.

The IR data show that pressure plays a major role on the incorporation of gaseous CO_2 in both cordierite and beryl, whereas the effect of temperature is limited. The spectroscopic data show that the diffusion of CO_2 occurs preferentially along the structural channels parallel the c-axis direction (top Fig. 1). Diffusion coefficients (D) for beryl were calculated using the monodimensional diffusion equations; obtained values are in the order of 10-14 m^2/s between 700 – 900°C (bottom Fig. 1).

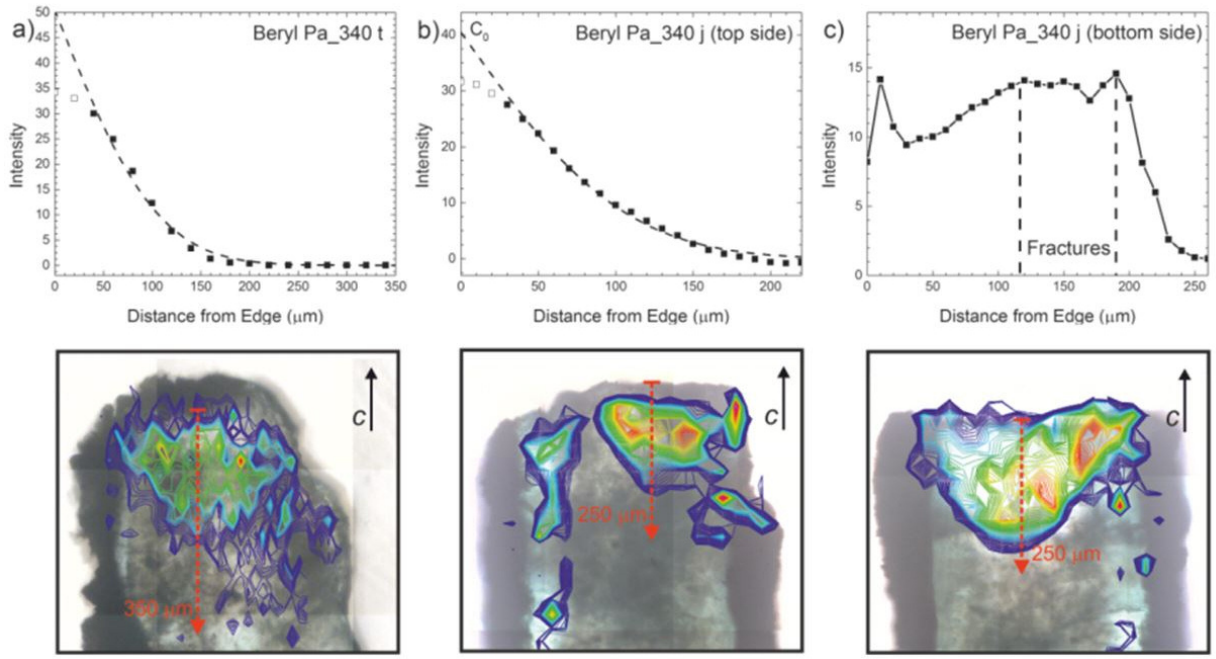

Fig. 1 I (a, b) selected CO_2 diffusion profiles measured along the c axis direction. (c) Example of a diffusion profile obtained across two fractures about 115 μm and 190 μm from the crystal edge.

Fitting of the diffusion coefficients in the Arrhenius plot yielded −logD0 = 7.2±0.7 m^2/sec and an activation energy Ea = 122±15 kJ/mol. Sample cracks formed during the high pressure experiments were found to enhance significantly the gas diffusion within the samples (Fig. 2).

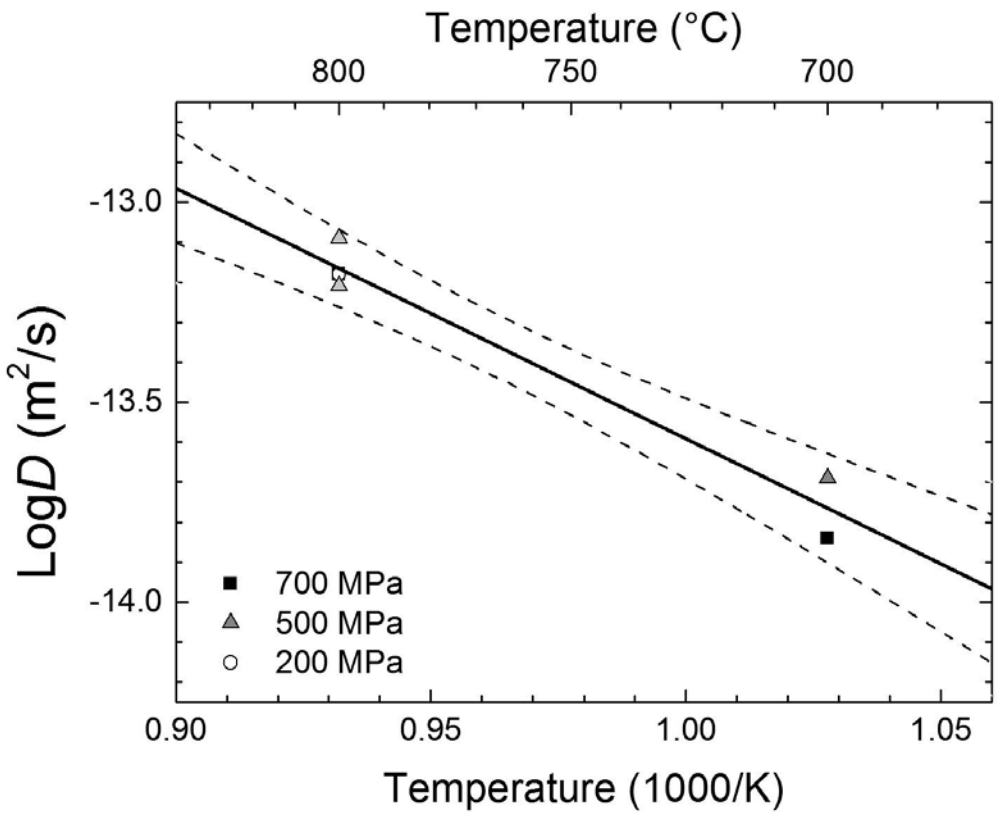

Fig. 2 I Arrhenius plot for diffusion coefficients of CO_2 in treated beryl samples.

FTIR imaging in diffusion studies: CO_2 and H_2O in a synthetic sector-zoned beryl

G. Della Ventura, F. Radica, F. Bellatreccia, A. Cavallo, G. Cinque, L. Tortora, H. Behrens

Research Line V1

In this work we investigate the strongly inhomogeneous distribution of CO_2 and H_2O in a synthetic beryl having a peculiar hourglass zoning of Cr due to the crystal growth.

The sample was treated at 800°C, 500 MPa, in a CO_2 rich atmosphere. High-resolution FESEM images revealed that the hourglass boundary is not correlated to physical discontinuities, at least at the scale of tens of nanometers. Polarized FPA-FTIR imaging, on the other side, revealed that the chemical zoning acts as a fast pathway for carbon dioxide diffusion, a feature never observed so far in minerals.

The hourglass zone boundary may be thus considered as a structural defect possibly due to the mismatch induced by the different growth rates of each sector. High-resolution synchrotron-light FTIR imaging, in addition, also allows enhancement of CO_2 diffusion along the hourglass boundary to be distinguished from diffusion along fractures in the grain.

Therefore, FTIR imaging provides evidence that different diffusion mechanisms may locally combine, suggesting that the distribution of the target molecules needs to be be carefully characterized in experimental studies.

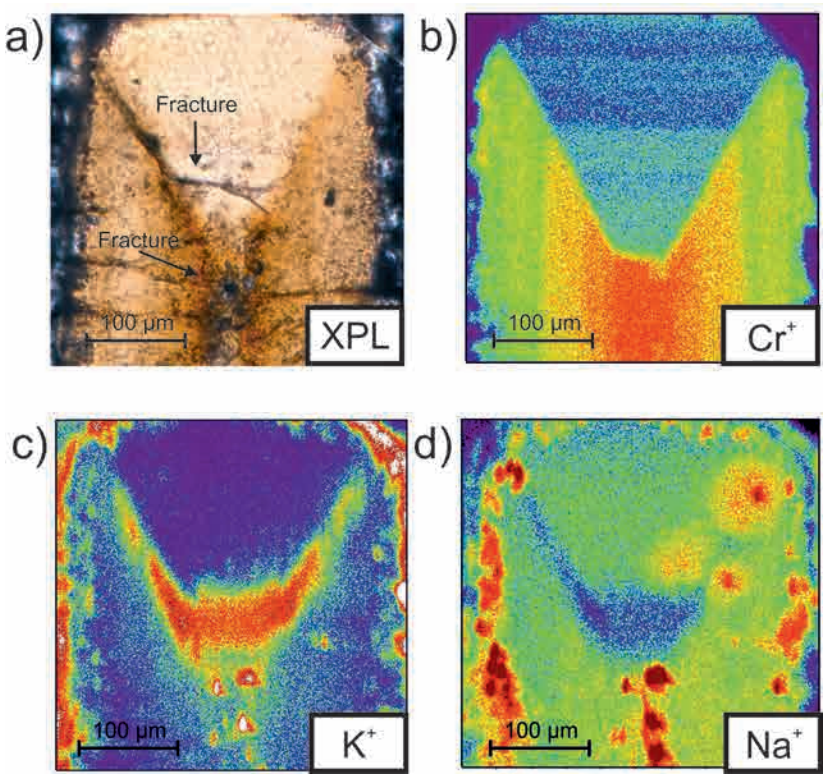

Fig. 1 | TOF-SIMS images of the studied beryl sample after the experimental run. The color scale is proportional to the element contents from red (high) to blue (low).

This piece of information is mandatory when the study is aimed at extracting diffusion coefficients from analytical profiles.

Combination of TOF-SIMS and FPA data shows a significant depletion of type II H_2O along the hourglass boundary (Fig. 1) indicating that water diffusion could be controlled by the distribution of alkali cations within channels, coupled to a plug effect of CO_2 (Fig. 2).

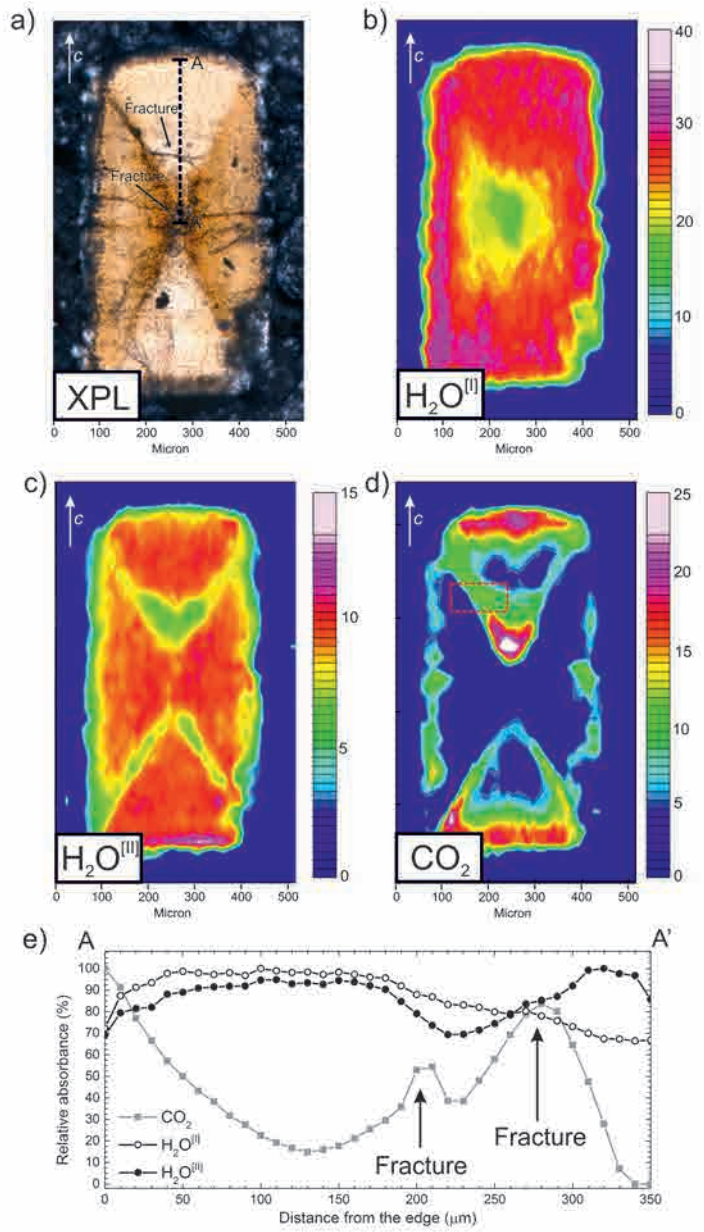

Fig. 2 I Polarized-light FPA-FTIR images of the studied sample.

8.2 ROCK PHYSICS

Unravelling Heavy Oil distribution and its controlling factors through the use of multi-scale scale datasets: the Oligo-Miocene Carbonate Reservoir of the Maiella Mountain (Central Apennines, Italy)

F.Trippetta, R. Ruggieri, L. Lipparini

Research Line T2

Heavy oil and bitumen provide a large potential supply of the world's oil resource; in Italy these resources have been extensively extracted across 19th and early 20th Centuries, particularly from the parially outcropping reservoirs of the Majella NW flank (Central Apennines). Even if studied in many aspects and largely exploited in the past, the HC distribution in this area is still not well known and understood.

The aim of our ongoing research is thus to contribute in understanding and characterize the main factors that controlled HC distribution, such as reservoir quality, trap geometry, burial/exhumation history, migration mechanism and fault/fracture system and the contribution of HC content in changing the petrophysical properties of rocks, by merging laboratory experiments, well data and static models. We focus on the carbonate-bearing Majella reservoir that represent an interesting analogue for the several oil fields discovered in the subsurface in the region, allowing a comparison of a wide range of geological and geophysical data at different scale.

The main reservoir is made of high porosity ramp calcarenites of the Bolognano formation (Oligo-Miocene), structurally slightly affected by a superimposed fracture system and displaced by few major NNW/SSE normal faults, with some minor strike-slip movements recognised.

With the objective to produce a dense 3D model (using Petreltm) of the reservoir petrophysical characteristics and hydrocarbon distribution (in the subsurface and at surface), various dataset at different scales were integrated:

- Data from original Field work and thin section analysis.
- Laboratory measurements from about 30 samples (density, porosity, Vp/Vs).
- Results of an extensive historical drilling campaign: about 200 shallow wells, 80-230m deep (pay thickness, HC%).
- Well and subsurface data from deep exploration drilling.

Sets of rock specimens were selected in the field and in particular two groups were investigated: 1. clean rocks (without oil) and 2. HC bearing rocks (with different saturations). For both groups, density, porosity, P and S wave velocity, permeability and elastic moduli measurements at increasing confining pressure were conducted on cylindrical specimens at the HP-HT Laboratory of the Istituto Nazionale di Geofisica e Vulcanologia (INGV) in Rome, Italy.

For clean samples at ambient pressure, laboratory porosity varies from 10 % up to 26 % and P wave velocity (Vp)

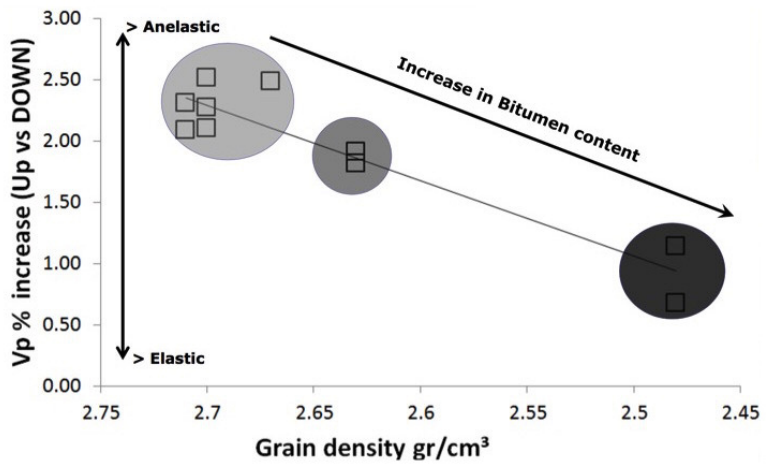

Fig. 1 I Variation of hysteresis (calculated as the difference between Vp measured at ambient pressure before and after the application of a 100 MPa confining pressure to the sample) with increasing HC content. The HC content seems to facilitate elastic behaviour by reducing hysteresis.

spans from 4,1 km/s to 4,9 km/s and a very good correlation between Vp, Vs and porosity is observed. The P wave velocity at 100 MPa of confining pressure, ranges between 4,5 km/s and 5,2 km/s with a pressure independent Vp/Vs ratio of about 1,9. The presence of HC within the samples affects both Vp and Vs. In particular velocities increase with the presence of hydrocarbons proportionally respect to the amount of the filled porosity. Preliminary data also suggest a different behaviour at increasing confining pressure for clean and-oil bearing samples: almost perfectly elastic behaviour for oil-bearing samples and more inelastic behaviours for cleaner samples (Fig. 1). Thus HC presence appears to contrast the increase of confining pressure acting as semi-fluids, reducing the rock inelastic compaction and enhancing its elastic behaviour.

Field observation and subsurface data highlights that HCs presence/quantity within the reservoir (laterally and vertically), is not simply related with porosity trend, nor it is just directly related to faults/fractures presence. Evidences suggest a more complex phased HC migration/emplacement/trapping and exhumation history that we want to contribute to unravel through the merging of the different dataset and lab experiments (currently ongoing velocity/permeability measurements and deformation tests on both clean/oil-saturated rocks).

The comparison of laboratory results with surface and subsurface data is expected to produce new clues to understand the observed distributions of HCs, also as analogue for other oil fields.

"Reddish patina" from shear zones of Central Apennines

A. Merico, L. Smeraglia, B. Pace, A. Billi, A. Cavallo, G. Iezzi

Research Line V3

Reddish patinas are roughly planar bodies, with a thickness ranging from ~1 mm to ~1 cm, an irregular contour on plane and with a very distinguishable colour from red to brown, sometimes vanishing from green to light pink (Fig. 1). They are peculiar in carbonate rocks cropping on Appennines. Despite their common occurrences, these intriguing object has not been investigated yet, such to unravel their textural and chemical-physical peculiarities potentially indicative of their formation, particularly their tectonic and seismic significance, if any.

Here, we considered two shear zones located at East and North of Fucino plain: San Benedetto-Gioia dei Marsi (SBGM) and the Tre Monti (TM) tectonic structures, respectively. We first considered the occurrence and distribution of reddish patinas in the field. Patinas inevitably and irregularly occur only on tectonic planes, either with

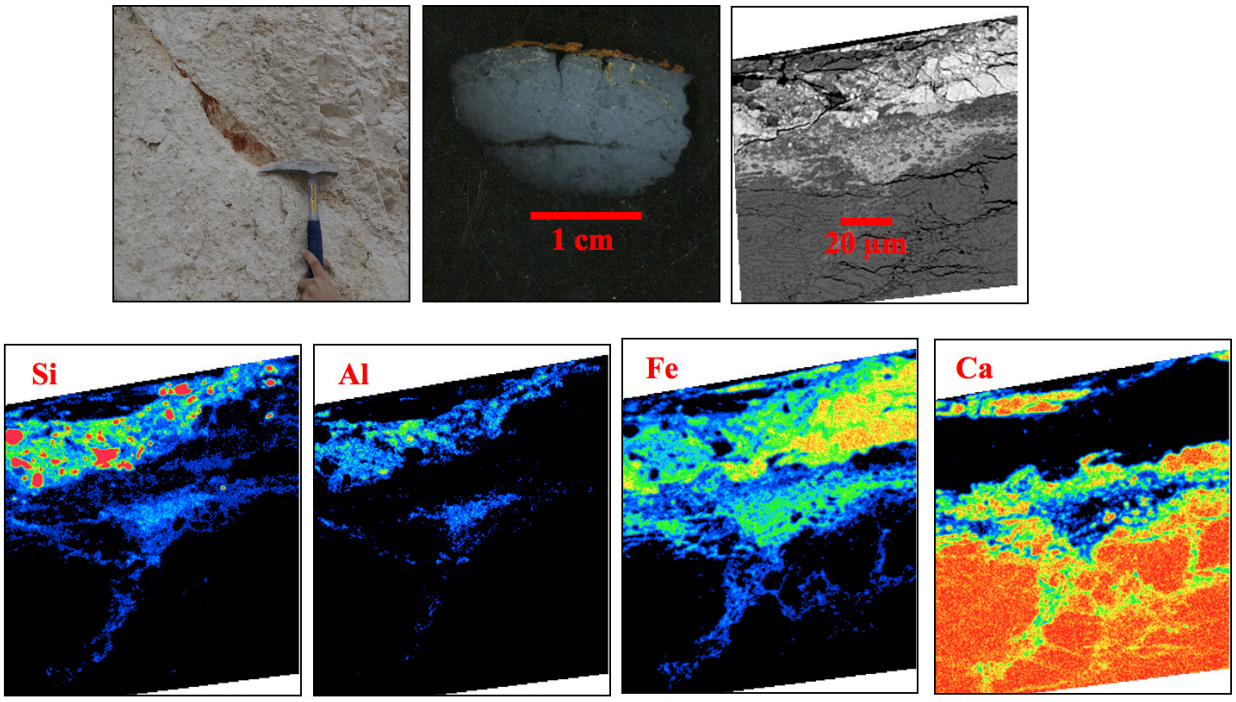

Fig. 1 I (top row, right to left). Typical reddish patinas in the field; thin section scan image of patinas plus hosting carbonate matrix perpendicular to tectonic plane; patinas, hosting carbonate and their irregular contacts at a micrometric scale. (down row, right to left) Si, Al, Fe and Ca EPMA maps showing chemical distribution of elements in and around patinas.

significant or apparent absent slip as well as onto main faults, secondary conjugate faults or joints; in addition, these patinas invariably show kinematic features indicative of their involvement in the tectonic processes. From this first survey on the filed, we selected three patina-bearing carbonate tectonised rocks, two from the two SBGM and TM main faults and one from the inner portion of the SBGM shear zone. We prepared polished rock surface

normal to the planes of patinas to observe their macroscopic features and to select area for thin sections (Fig. 1). The three thin sections were analyzed with optical microscopy and BSE-SEM, as well as by EPMA to quantify their compositional features and relation with hosting carbonate matrix (Fig. 1). Furthermore, these patinas with their carbonate matrix were also investigated by XRPD and XRF.

XRPD indicate that patinas from TM are composed of poorly crystalline $Fe^{3+}(OH)_3$ goethite, whereas the two XRPD patterns from SBGM samples detected only calcite, indicative of a very low amount of patina hosted in these rocks. The carbonate matrix free of patina is composed of $CaCO_3$ for > 99.5 wt.%, whereas other oxides account for <0.5 wt.%.

Optical and SEM observations at different magnifications (2.5 to 2000 X) show that patinas are mainly aligned along their hosting tectonic plane, but some minor flames are almost normally injected in the carbonate hosting matrix (Fig. 1). The most intriguing and useful features of these patinas are provided by Si, Al, Fe and Ca EPMA maps (Fig. 1). Patinas are enriched in Si, Al and Fe and Ca-free; however, inside patinas two zones with a different enrichment in Fe can be observed (Fig. 1).

All these data point out that occurrence of patinas are driven by tectonic structures; however, it is still undetermined if they formed before or approximately simultaneous to tectonic events. The formation of patinas from dissolution of hosting carbonates and/or from precipitation from meteoric waters can be excluded according to their physico-chemical characteristics. It is instead plausible that patinas witness relative deep circulation of brines and were injected in these carbonate rocks under the same tectonic stress field that produced these shear zones. The parent bodies from whom these brines originate is still completely lack.

Textural variations into carbonate fault rocks: the San Benedetto-Gioia dei Marsi (Fucino, central Italy) shear zone

A. Merico, M. Cremona, L. Ferranti, B. Pace, G. Iezzi, A. Colella, M. Scafa

Research Line T2

Shear zones in carbonate fault rocks are frequently defined in terms of grain-size features collected on few key samples of fault core. However, possible textural variations along the strike of the main fault plane and moving away from the fault core into the damage zone are relatively less studied.

Thereby, we have focused on the shear zone associated to the San Benedetto-Gioia dei Marsi (SBGM) fault (Fucino Plain, central Italy) in the Venere quarry outcrop, broadly located in the central portion of the fault. The SBGM is an active normal fault located along the eastern border of the Fucino basin, and is considered responsible for the large 1915 earthquake (Mw 7.0) that struck central Italy. The about 100 m wide shear zone consists of fault planes and cohesive, fractured and pulverised carbonate rocks.

Here, we have analysed in the field, collected and studied in laboratory several oriented samples along the main

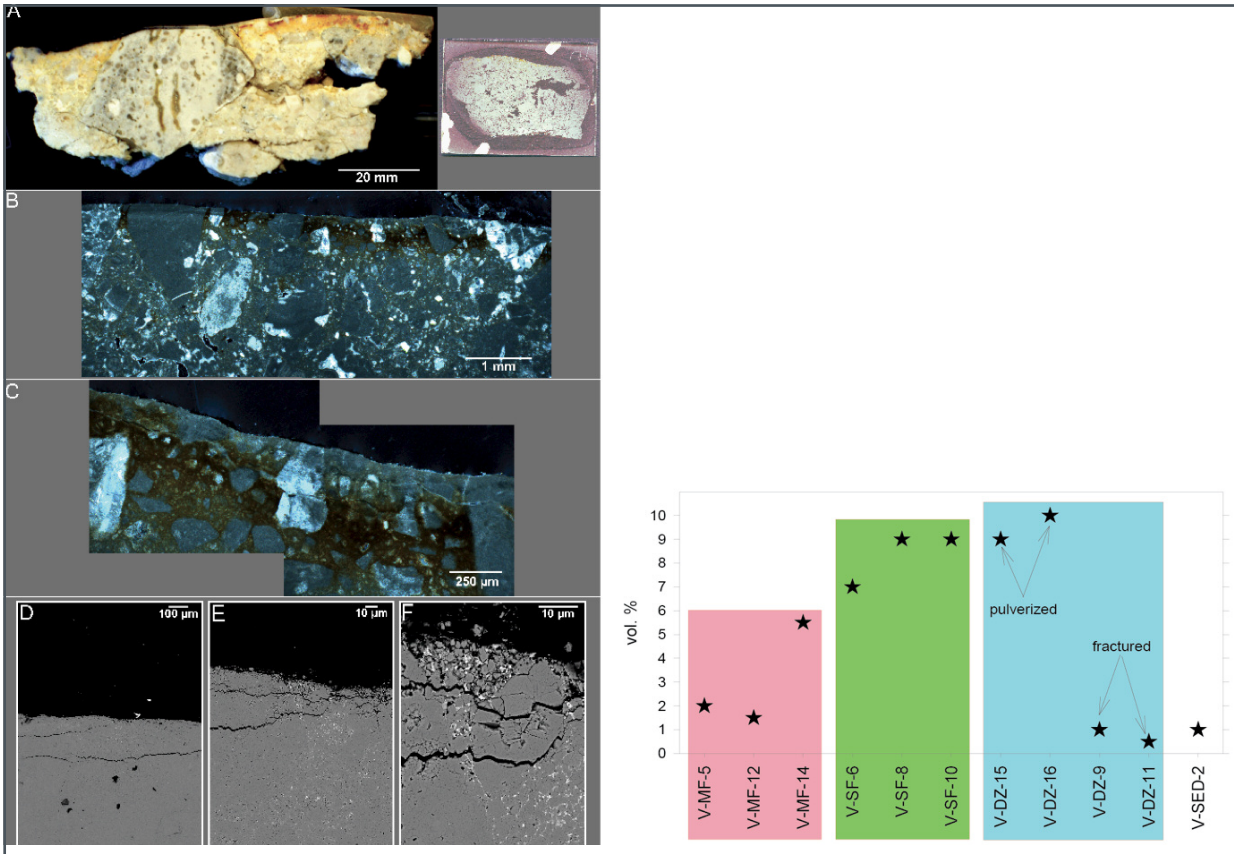

Fig. 1 | (left) Representative images of rock surfaces at different magnifications for qualitative and quantitative analyses of textural parameters: (A) polished rock surface, (B and C) optical and (E, D, F) BS-SEM (SEM, D, E, F) microscopic micro-photographs. (right) Variations of connected porosity of the analysed samples from the different portions into the SBGM shear zone (V-MF: Venere main fault, V-SF: Venere secondary fault, V-DZ: Venere damage zone, V-SED: Venere sedimentary and undeformed carbonate rock).

fault and within both its core and the pulverised rocks inside the damage zone. We quantified the textural parameters using mesoscopic and microscopic images (Fig. 1). Mesoscopic data were obtained on detailed field measurements (scan areas), photos and polished rock sample surfaces (few dm^2), whereas microscopic data were studied on thin sections (35 cm^2) using both optical and electronic (SEM) images. Textures of tectonic grains were quantified by image analysis, to obtain the area, aspect ratio and long plus short axes of equal-area ellipses. Therefore we detailed the textural variations from microns to centimetres. The grain size distributions evidence that these fault rocks are cataclastics. Interestingly, the main fault is characterised by a higher amount of large grains (> 2mm) than the damage zone samples; in addition rock samples on the main fault shows differences in grain size distribution along strike.

Moving from the undeformed to the main fault along three roughly parallel transects, petrophysical measurements by Hg-porosimeter show that porosity is <1% in the host rock (~100 m away from the fault), about 10% in the damage zone, and comprised between ~2 and 6 % in the three fault core samples (Fig. 1), confirming previous results and extending the area of decreasing porosity up to ~10 m away from the fault. All these results unravel that rock textures in the shear zone are very variable and reflect complex deformation processes. The actual features of a carbonate shear zone can be more properly captured studying rocks along strike and normal to the fault plane.

An empirically-based steady-state friction law and implications for fault stability

E. Spagnuolo, S. Nielsen, M. Violay, G. Di Toro

Research Line T4

Empirically-based rate-and-state friction (RSFL) have been proposed to model the dependence of friction forces with slip and time. The relevance of the RSFL for earthquakes mechanics is that few constitutive parameters define critical conditions for fault stability (i.e. critical stiffness and frictional fault behavior).

However, the RSFL were determined from experiments conducted at sub-seismic slip rates (V<1 cm/s) and their extrapolation to earthquake deformation conditions (V> 0.1 m/s) remains questionable on the basis of the experimental evidence of (1) large dynamic weakening and (2) activation of particular fault lubrication processes at seismic slip rates.

Here we propose a modified RSFL (MFL) based on the review of a large published and unpublished dataset of rock-friction experiments performed with different testing machines. The MFL has the following analytical formulation:

$$\mu_{ss} = [\mu_0 + (a-b)\log(V/V_0)]/(1+(V/V_c)^p) \qquad \text{Eq. (1)}$$

where μss is the steady state friction value, $V_0 = 1\mu m/s$ and μ_0 $(V_0) \approx 0.7$ are reference values often used in the RSFL literature.

Parameters Vc and ρ were determined with a best fit linear least square procedure resulting in the range of variability reported in Table 1 for three main rock types (i.e calcite- silica- bearing and quartz - rich rocks).

The MFL is valid at steady-state conditions from sub-seismic to seismic slip rates (0.1 μm/s <V<3 m/s) and describes the initiation of a substantial velocity-weakening in the 1-20 cm/s range.

The critical velocity Vc and the parameter ρ have a microphysical foundation which strongly correlates with specific physicochemical processes occurring at the asperity scale and within the slipping zone.

The MFL results in a critical stiffness increase that creates a peak of potential instability in that velocity regime (Fig. 1). The variability of Kc with the velocity regime might explain

(1) why friction experiments performed at either high (~1 m/s or more) or low (<1 cm/s) velocities are less demanding than those conducted in the intermediate velocity regime, where the stability and control of the system are more difficult to achieve (Fig. 1b),

(2) the onset of slip behavior with different frequency content (from stable slip to stick slip) and provide hints on the plethora of events observed on natural fault systems.

The MFL leads to a new definition of fault frictional stability with consequence on slip event styles and relevance

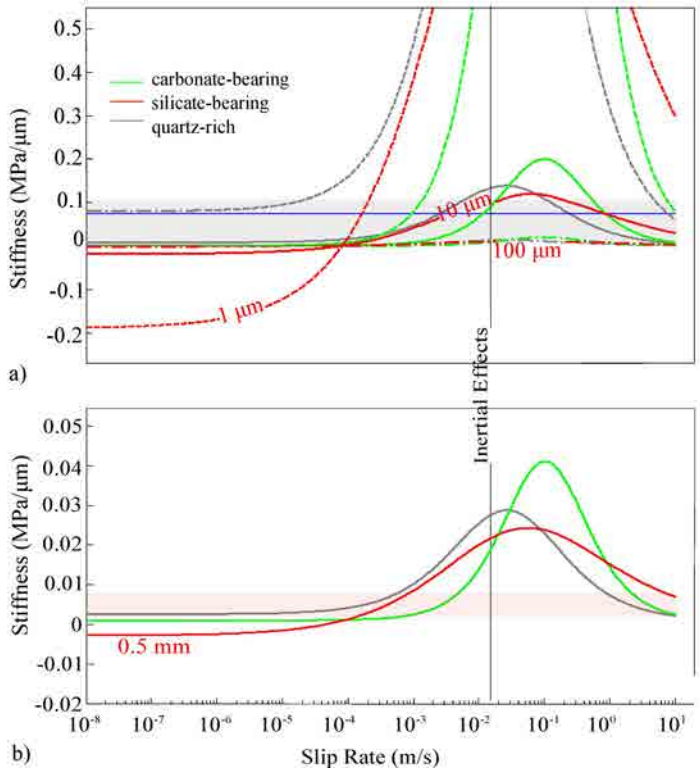

Fig. 1 | The critical stiffness kc vs. machine (or natural) stiffness k for the three rock categories. a) Laboratory faults: kc is computed using the MFL (Eq. 1) for σn =10 MPa. The k =0.074 MPa/μm for SHIVA is in blue solid line, a range of other machine stiffness corresponds to the gray shaded area. For kc <k frictional sliding is stable, for kc ≈ k and V~0.1 m/s (intermediate velocity regime) theoretical stability analysis predicts the onset of oscillations, consistently with experimental observations. For kc > k (V>Vc) the friction coefficient drops, and inertial effect may become dominant. b) Natural faults: kc results from the extrapolation of the MFL to natural conditions (σn = 100 MPa, Dc = 0.5 mm). A range of k for natural faults (red shaded area) was computed assuming a fault patch radius between 5-50 m and shear stiffness of G=25 GPa.

for models of seismic rupture nucleation, propagation and arrest.

Fracture energy, friction and dissipation earthquakes

S. Nielsen, E. Spagnuolo, M. Violay, S. Smith, G. Di Toro, A. Bistacchi

Research Line T4

Recent estimates of fracture energy G0 in earthquakes show a power-law depenence with slip u which can be summarised as $G0 \propto u\gamma$ where γ is a positive real slightly larger than one. For cracks with sliding friction, fracture energy can be equated to Gf the post failure integral of the dynamic weakening curve. If the dominant dissipative process in earthquakes is friction, G0 and Gf should be comparable and show a similar scaling with slip. We test this hypothesis by analyzing experiments performed on various cohesive and non-cohesive rock types, under deformation conditions typical of seismic slip (normal stress of tens of MPa, target slip velocity >1m/s and fast accelerations ≈6.5 m/s^2). Despite a great variability observed in the details of the weakening transient, a substantial decay in sliding friction is systematically observed, due to the activation of lubrication processes under high frictional power dissipation. The weakening part of the sliding friction curve is generally well matched by a power-law of slip u in the form $\tau = u{-}\alpha$ (with $0.35 < \alpha < 0.6$), tapered at the beginning and the end by the peak shear stress τp and the steady-state the residual shear stress τss, respectively (Fig. 1). The resulting fracture energy $Gf \propto u1{-}\alpha$ is similar to the seismological estimates, with Gf and G0 being comparable over most of the slip range. However, in most of the reported earthquake sequences $\gamma > 1{-}\alpha$ and, while Gf appears to saturate at u ≈ 1–10 m, G0 appears to increase further and surpasses Gf at large magnitudes. We analyses several possible causes of such discrepancy, in particular, additional off-fault damage in large natural earthquakes.

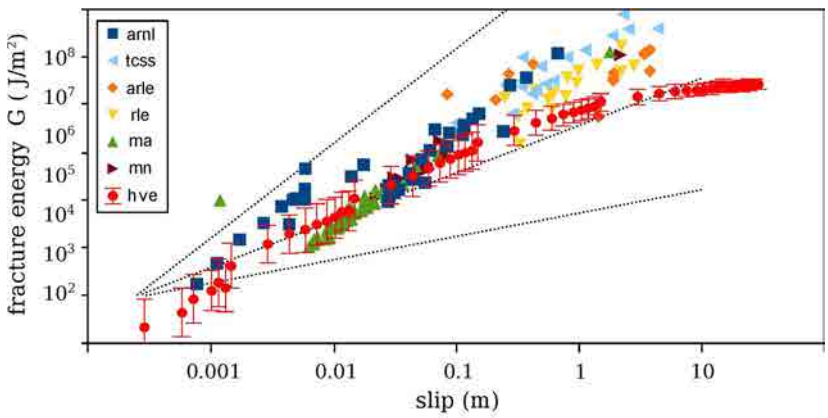

Fig. 1 | Laboratory (Gf, in red) and seismological (G0, other colours) estimates of fracture energy under coseismic slip conditions. Red disks correspond to the average Gf for 28 high velocity experiments (hve, this study), shown at various slip amounts; the standard deviations (vertical bars) indicate the scatter due to the variety of lithologies and experimental conditions. Squares, triangles and diamonds correspond to seosmological estimates G0. arnl: Northridge aftershocks (Abercrombie and Rice, 2005); arle: large earthquakes (Abercrombie and Rice, 2005); tcss: numerical simulations (Tinti et al., 2005); rle: large earthquakes (Rice, 2006); ma: L'Aquila (Malagnini et al., 2013); mn: Northridge sequence (Malagnini et al., 2013). Dashed lines indicate exponent 0.5, 1 and 2 for reference.

Improvements on Ultrasonic Waves velocity measurement with BRAVA

G. Di Stefano, M. M. Scuderi, C. Collettini

Research Line T4

To estimate the flight time and propagation velocity of P-type ultrasonic vibrations crossing a rock samples during a stick-slip experiments, electronics instruments are been integrated to the BRAVA electronic basic apparatus. Improvements on the new hardware and control process have given back high quality results on the continuous ultrasonic wave emissions. The block diagram (Fig. 1) shows the new devices connected to the BRAVA basic control system (RT-Controller and HOST-PC) used generally only for mono/bi/tri axial rock mechanics experiments.

Two granular rock layers 50x50 mm^2 are sandwiched between two side forcing steel block and one central block for biaxial double-direct-shear configuration. An elastic element is been inserted between the piston and the central block to reduce the stiffness of the vertical loading segment than the rock stiffness kc. Two LVDT transducers (A e B) are installed to measure the rock deformation during the shear and normal stress. Two barium-titanate P type cylinder piezoelectric transducers are used as ultrasonic source (Tx) and receiver (Rx); they are embedded inside a cavity on each side forcing block of the double direct shear assembly, at 7mm distance from the rock sample. The transducers are broadband type with thickness of 2m and diameter of 20mm, and central frequency of 1MHz (PI Sensor PIC255) without con-

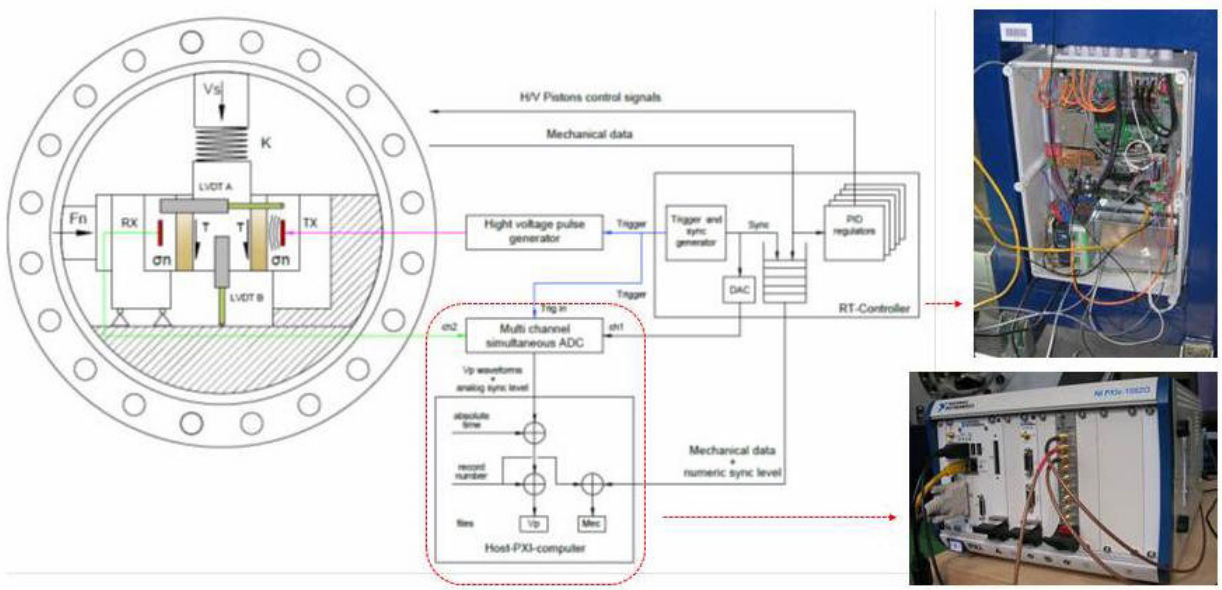

Fig. 1 I The block diagram of the BRAVA basic electronic control system (RT-Controller and Host-PXI-PC) and the new devices: high voltage generator and the multichannel simultaneous ADC board installed on the Host.

strain. The mechanical signals are digitalized by the base control system, at sampling rate of 10KHz by the low level RT controller and transmitted to the Host computer in a FIFO queue. Mechanical data records are produced by the high level Host-computer through the elaboration with average processing with variable rate depending of the experiment speed.

The single data record is marked by a progressive record number and stored on the Mec text file. The Tx is polarized by a high (300 – 900 Volt) and very short (≅800µs) voltage pulses supplied by a pulses generator triggered by an external signal (trigger), coming from a counter implemented on FPGA in the low level real time (RT) control system. The trigger frequency is changeable by command located on the system so the ultrasonic pulse wave occurrence can change every 0.01, 0.1, 1, 10, 50 and 100 Wave/s during an experiment.

The ultrasonic signals are acquired by an 8-channel 14-bit simultaneous sampling ADC board (ADLink PXIe-9848) with a sampling rate up to 100MS/s per channel, installed on the Host-PXI-computer; here we configure the board for finite acquisition with a time slot of 200µs @50MHz sampling frequency (10000 points per signals). The synchronize algorithm is been performed to eliminate the time delay for the matching post process. When a trigger signal happens a numeric counter increases a numeric variable (Sync), as showed in figure 2a, and one-shot finite acquisition starts; the new sync numeric value is added in to the FIFO queue, while the analog sync signal level is acquired simultaneously with the ultrasonic signal detected on the Rx. For each trigger a new ultrasonic waveform (UW) is stored in a second Vp binary format file; the data record contains ultrasonic waveform and markers (absolute system time, mechanical data record number and Sync signal amplitude) for a coarse and fine synchronization between each UE wave and the mechanical data record (Fig. 2b). The first time arrivals is been extract for each UW to calculate the crossing time (flight time) over the assembly blocks and rock layers and their propagation velocity. The figure 2b shows the matching of UW generated @10Wave/sec and the shear stress profile during a slow stick slip event. The red dots indicate the points where the UWs are generated.

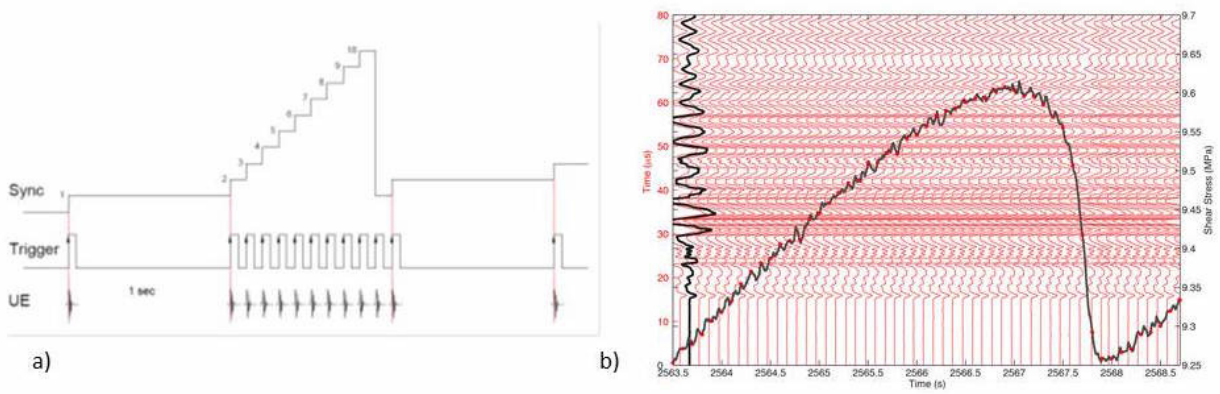

Fig. 2 I a) On trigger rising the analog sync increasing the level and starts the recording of 200µs ultrasonic signal, detected by Rx. b) Example of waveform records during a slow-slip event. Waveforms here are recorded at 10Hz.

Looking for seismites in the Fucino basin

A. Smedile, R. Civico, P. Del Carlo, V. Sapia, P. M. De Martini, D. Pantosti, C. Brunori, S. Orefice, S. Pinzi, S. Pucci

Research Line T2

The Fucino Plain is an extensional intramountain basin filled by Pliocene to Quaternary continental alluvial and lacustrine deposits. It was the site of Lake Fucino, a large endorheic lake drained at the end of the 19th century. Our research was focused close to its central part that apparently displays the longest lacustrine sedimentary sequence and where several coseismic effects of the 1915 Avezzano earthquake were reported and studied.

In spring 2014, a field survey was performed on the Fucino Plain and several 5m long engine cores (Figure 1 left side) were collected both in the present-day depocenter of the Fucino Plain (named "Bacinetto") and close to that area where the longest lacustrine sedimentation record exists. On each PVC core a Computed Axial Tomography (CAT) was performed in order to identify peculiar intervals or sudden changes in the sedimentation otherwise not easily identifiable through a normal visual inspection. After the CAT inspection, only selected cores were opened, photographed, logged and sampled for sedimentological, paleonvironmental (ostracods fauna), tephrostratigraphical and radiocarbon analyses.

From a selected core (FUC-S4) a sequence of ca. 5 m was analysed and subdivided in three main units. Starting from the bottom ca. 3 m thick of laminated gray to green-gray, organic rich silty clay is found (unit A). Moving up along the core, the following unit B, represented by a gray to hazel oxidized clayey silt rich in manganese nodules, is present between -2.65 and -1.40 m of depth.

The uppermost 20 cm of unit B shows an infill of gray silt that continues also in the uppermost third unit. In fact, the latter unit C, composed mainly by silt and clayey silt, shows in the lower 0.50 m both lithologies upside down and with vertical contacts.

Preliminary micropaleontological analyses on some selected samples showed a deep lacustrine ostracods assemblage for the unit A as indicated by the presence of Amnicythere fallax (DEVOTO), Candona neglecta SARS, Cypria ophtalmica (JURINE), Cytherissa lacustris (SARS).

The acquisition of FE-SEM images from selected ostracoda specimens has been also performed to better classify some species (Fig. 1 right side) and to get a high magnification of some shell details needed for their identification at specific level otherwise not clearly visible through the optical microscope analysis.

This research is developed within the framework of a national project focused on the seismic risk of the Abruzzo region (FIRB Abruzzo project, "High-resolution analyses for assessing the seismic hazard and risk of the areas affected by the 6 April 2009 earthquake"; http://progettoabruzzo.rm.ingv.it).

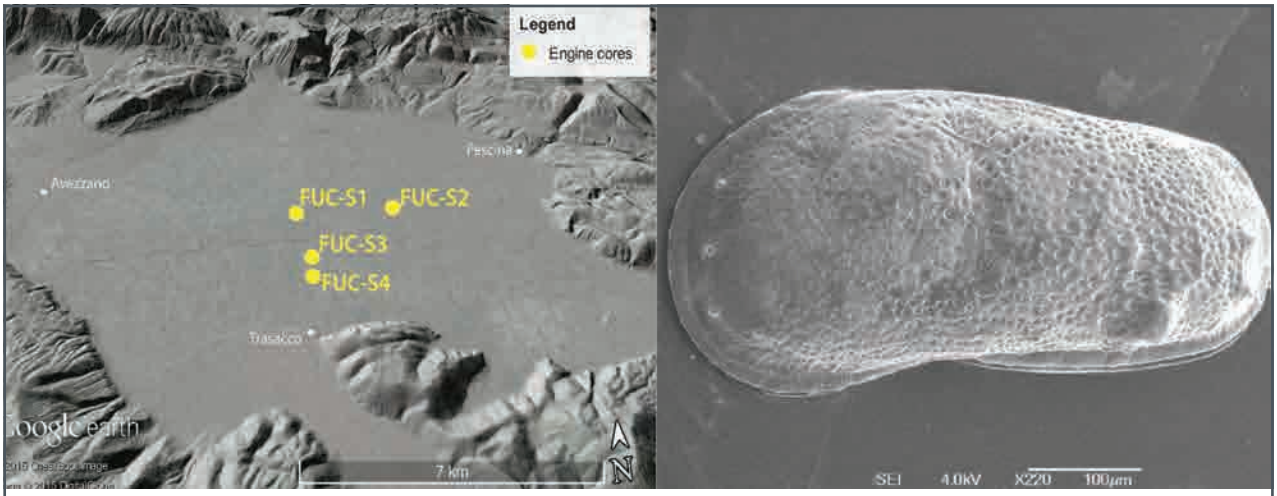

Fig. 1 | 1 On the left five meters Digital Elevation Model (DEM) draped over a Google Earth bird's eye view of the Fucino Plain. Yellow pins locate all the engine cores. On the right FE-SEM picture of the ostracod species Amnicythere fallax (DEVOTO).

Static versus dynamic fracturing in shallow carbonate fault zones

M. Fondriest, M. L. Doan, F. Aben, F. Fusseis, T. Mitchell, G. Di Toro

Research Line T4

Moderate to large earthquakes often nucleate within and propagate through carbonates in the shallow crust, therefore several field and experimental studies were recently aimed to constrain earthquake-related deformation processes within carbonate fault rocks.

In particular, the occurrence of thick belts (10-100s m) of low-strain fault-related breccias (average size of rock fragments >1 cm), which is relatively common within carbonate damage zones, was generally interpreted as resulting from the quasi-static growth of fault zones rather than from the cumulative effect of multiple earthquake ruptures.

Here we report the occurrence of up to hundreds of meters thick belts of intensely fragmented dolostones along the major transpressive Foiana Fault Zone (Italian Southern Alps) which was exhumed from <2 km depth. Such dolostones are reduced into fragments ranging from few centimeters down to few millimeters in size with ultrafine-grained layers in proximity to the principal slip zones. Preservation of the original bedding indicates a lack of signi-

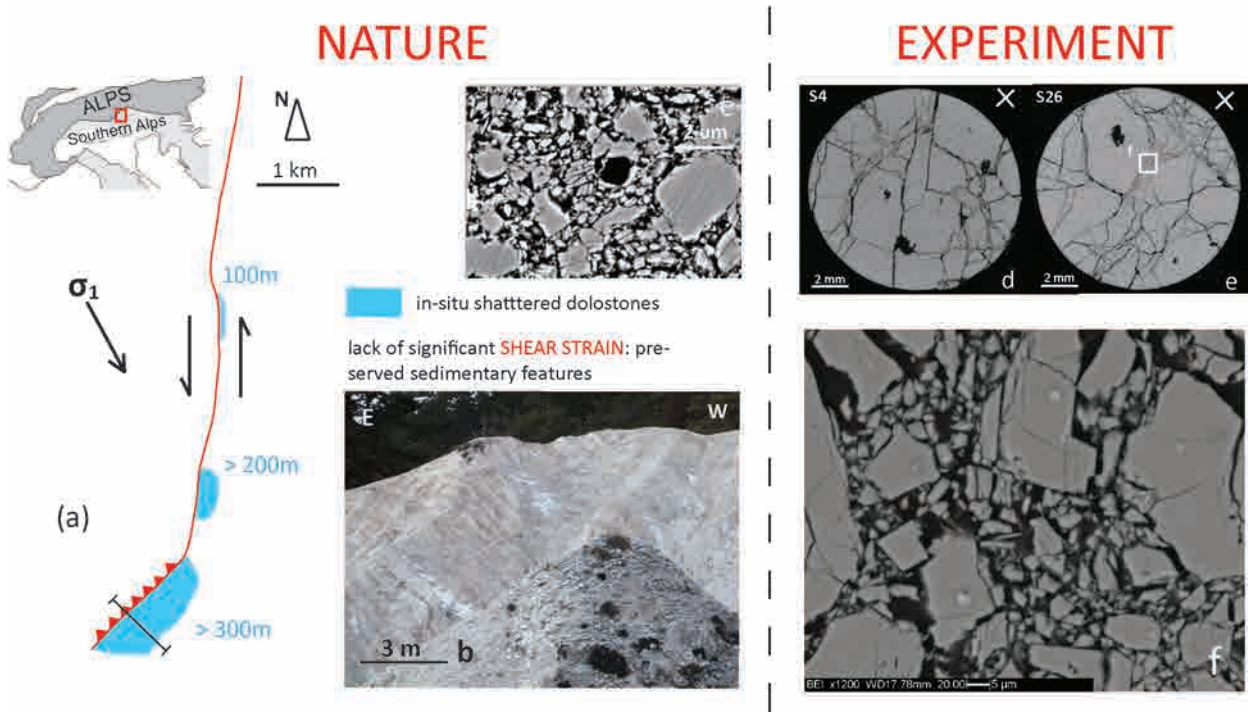

Fig. 1 | (a) Map view of the Foiana Fault Zone (Italian Southern Alps) and spatial distribution of in-situ shattered dolostones (light blue). (b) Studied section of the fault zone (trace of the section is indicated in a). In-situ shattered dolostones at the mesoscale are affected by intense fragmentation and lack of significant shear strain. (c) In-situ shattered dolostones at the microscale (BSE-SEM image) are characterized by splitting of clasts down to the micrometer scale. (d-e) Experimental in-situ shattered doostones produced at high-strain rate loading. Dolostones are affected by intense distributed fragmentation (fragment size mostly of few millimeters). (f) Experimental in-situ shattered dolostones are affected by local microfracuring with the presence of exploded clasts and splitting down to the micrometer scale. These microstructures are similar to the natural ones.

ficant shear strain in the fragmented dolostones which seem to have been shattered in situ (Fig. 1a-c).

To investigate the origin of the in-situ shattered rocks, the host dolostones were deformed in uniaxial compression both under quasi-static loading (strain rate ~10^{-3} s^{-1}) and dynamic loading (strain rate >50 s^{-1}). Dolostones deformed up to failure under low-strain rate were affected by single to multiple discrete (i.e. not interconnected) extensional fractures sub-parallel to the loading direction. Dolostones deformed under high-strain rate were shattered above a strain rate threshold of ~120 s^{-1} (strain >1.2%) while they were split in few fragments or were macroscopically intact for lower strain rates. Experimentally shattered dolostones were reduced into a non-cohesive material with most rock fragments a few millimeters in size and elongated parallel to the loading direction (Fig. 1d-f).

Fracture networks were investigated by X-ray microtomography showing that low- and high-strain rate damage patterns are different with the latter being similar to that of natural in-situ shattered dolostones. In-situ shattered dolostones are thus interpreted as the product of off-fault dynamic stress wave loading and can potentially be used to constrain coseismic energy release in fault zones.

Frictional Behavior of Talc-Calcite Mixtures

C. Giorgetti, B.M. Carpenter, C. Collettini

Research Line T4

Faults involving phyllosilicates appear weak when compared to the laboratory-derived strength of most crustal rocks. Amongst phyllosilicates, talc, with very low friction, is one of the weakest minerals involved in various tectonic settings. As the presence of talc has been recently documented in carbonate faults, we performed laboratory friction experiments to better constrain how various amounts of talc could alter these fault's frictional properties. We used a biaxial apparatus to systematically shear different mixtures of talc and calcite as powdered gouge at room temperature, normal stresses up to 50 MPa and under different pore fluid saturated conditions, i.e. $CaCO_3$-equilibrated water and silicone oil. We performed slide-hold-slide tests, 1-3000 seconds, to measure the amount of frictional healing and velocity-stepping tests, 0.1-1000 µm/s, to evaluate frictional stability. We then analyzed microstructures developed during our experiments. Our results show that with the addition of 20% talc the calcite gouge undergoes a 70% reduction in steady-state frictional strength (Fig. 1a), a complete reduction of frictional healing (Fig. 1b) and a transition from velocity-weakening to velocity-strengthening

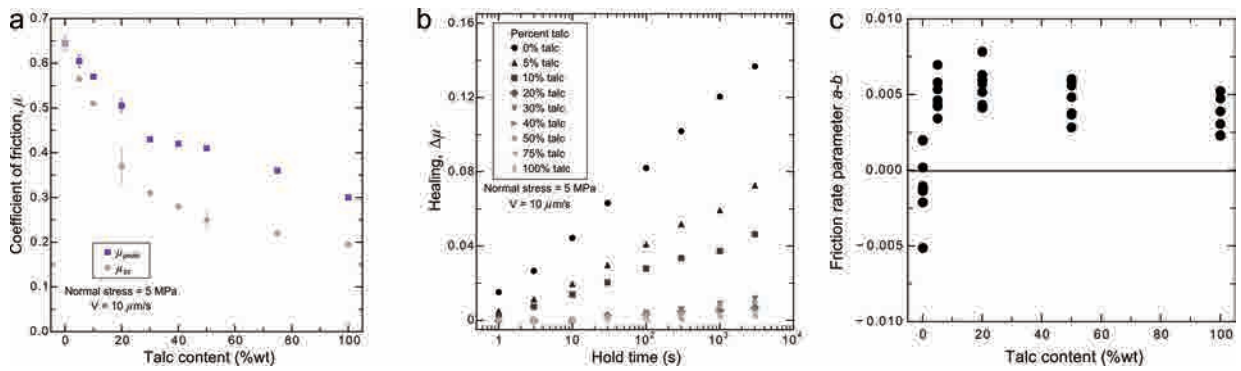

Fig. 1 | Frictional properties of talc/calcite binary mixtures. a) Friction of talc/calcite binary mixtures as function of talc content at 5 MPa normal stress. Friction systematically decreases with increasing talc content. b) Frictional healing as function of hold time for different talc contents at 5 MPa normal stress. A small amount of talc strongly reduces frictional healing. c) Friction rate parameters as function of talc content at 5 MPa normal stress. Talc/calcite mixtures are characterized by velocity-strengthening frictional behavior, i.e. positive (a-b).

behavior (Fig. 1c). Microstructural analysis shows that with increasing talc content, deformation mechanisms evolve from distributed cataclastic flow of the granular calcite to localized sliding along talc-rich shear planes, resulting in a fully interconnected network of talc lamellae from 20% talc onwards. We propose that the change in the mechanical properties of talc/calcite mixture occurring by about 20% talc content results from this switch in the deformation mechanism. Our observations indicate that, in faults where talc and calcite are present, a low concentration of talc is enough to strongly modify the gouge's frictional properties and specifically to weaken the fault, reduce its ability to sustain future stress drops and stabilize slip.

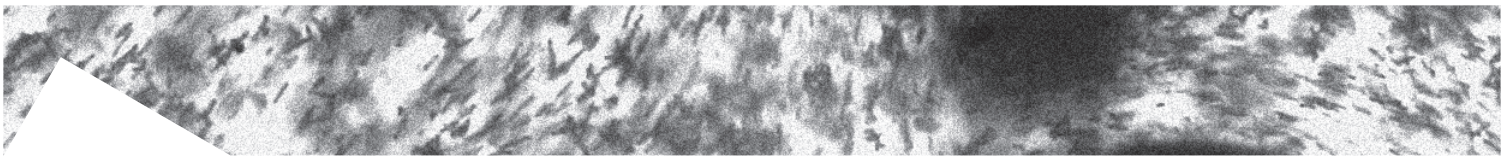

The role of fluid pressure in earthquake triggering: insights from an experimental study of frictional stability of carbonates

M. M. Scuderi, C. Collettini

Research Line T4

Fluid overpressure has been proposed as one of the primary mechanisms that facilitate earthquake slip along faults. However, elastic dislocation theory combined with rate- and state- friction laws suggests that fluid overpressure may inhibit the dynamic instabilities that result in earthquakes, by reducing the critical rheological fault stiffness, kc. This controversy poses a serious problem in our understanding of earthquake physics, with severe implications for seismic hazard and human-induced seismicity. Nevertheless, currently, there are only a few systematic studies on the role of fluid pressure under controlled, laboratory conditions for which the evolution of friction parameters and slip stability can be measured (Fig. 1, 2 and 3).

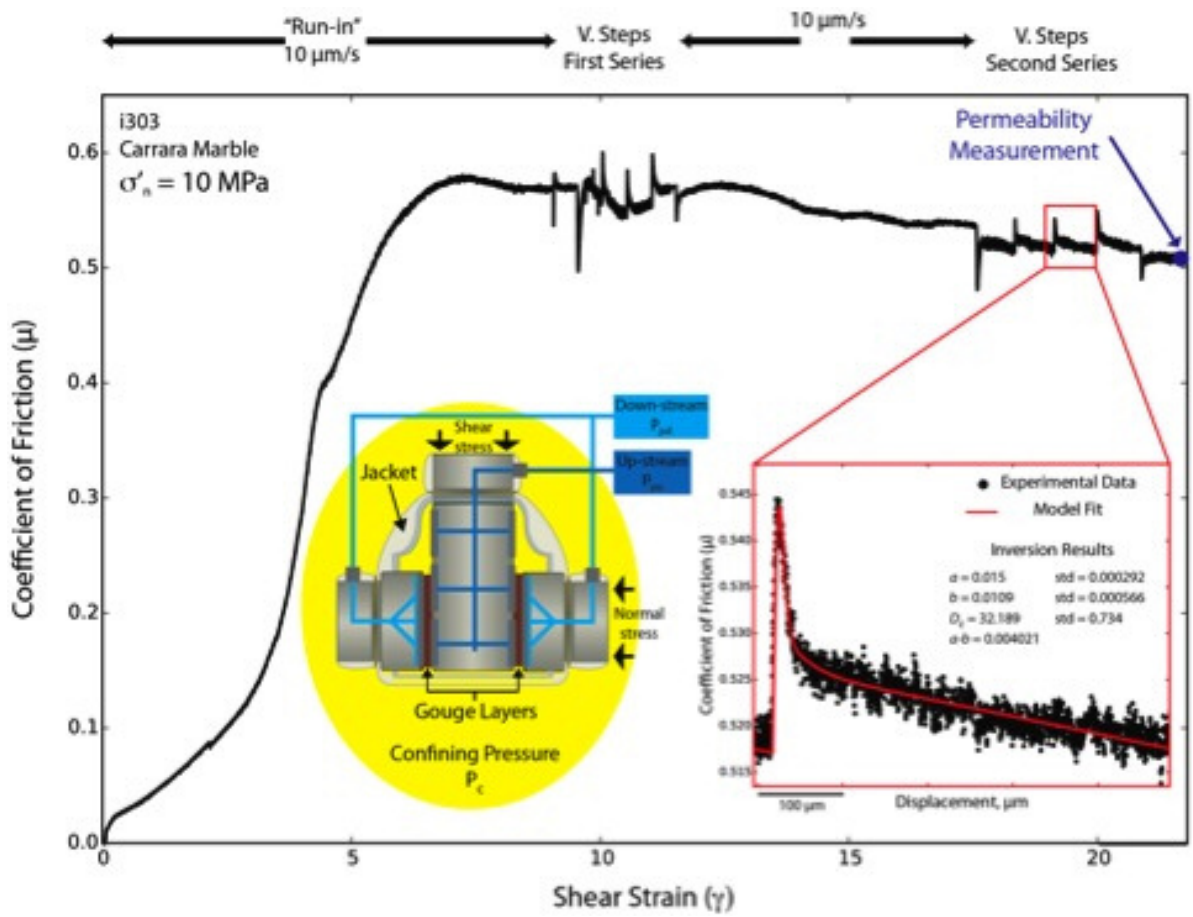

Fig. 1 I Friction experiments. Coefficient of friction vs. shear strain, γ, for one representative experiment on Carrara marble gouge. Velocity steps, for the characterization of the rate and state friction parameters, are conducted after about 7-10 γ (i.e 1 cm of shear displacement) and 17-21 γ (i.e. 2.5 cm of displacement). Permeability measurements are performed at the end of shearing. The inset in red shows the detail of one velocity step with the comparison between experimental data (black) and the result from the inversion model (red) used to obtain the (a, b) and Dc values. The yellow inset shows a schematic representation of the double direct shear configuration with forcing blocks equipped with fluid pressure conduits and the jacket to separate fluid pressurized gouge layers from the confining medium (details in the method).

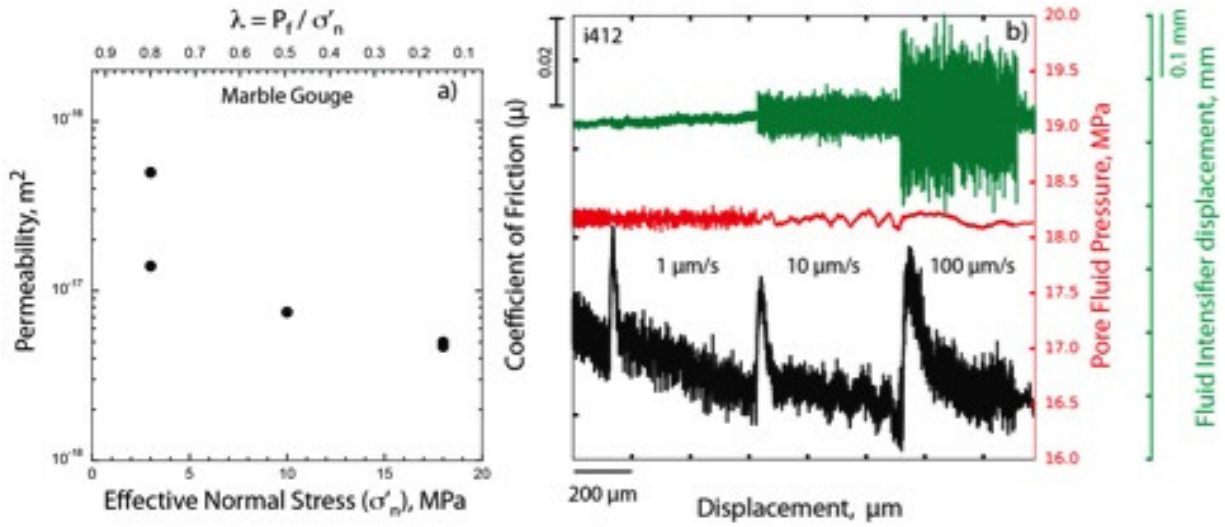

Fig. 2 I Fluid flow properties. a) Permeability measurements on Carrara marble gouge at constant applied normal stress (σn = 21 MPa) and different values of pore fluids pressure, Pf, resulting in different effective normal stresses, σn, and pore fluid factor λ = Pf/σn. b) During velocity steps, the fluid pressure (Ppd) and the upstream intensifier displacement remain constant, indicating fully drained boundary conditions.

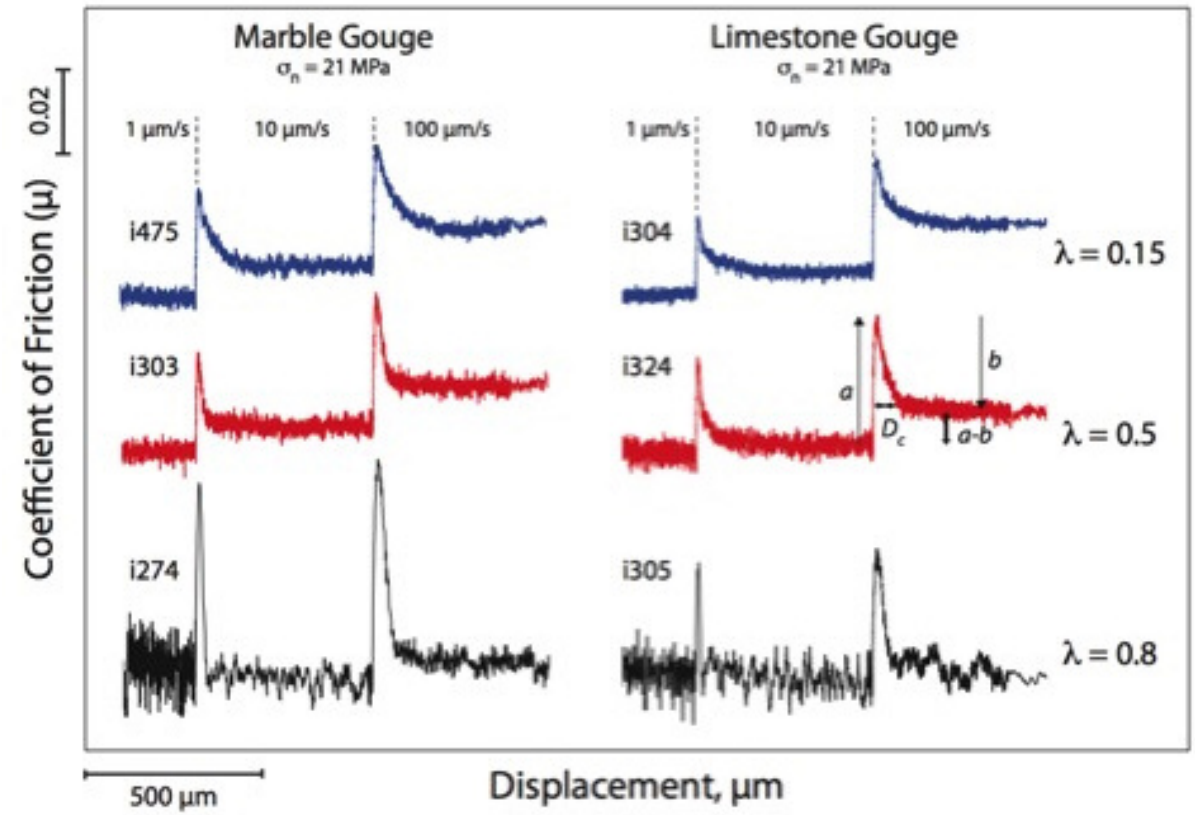

Fig. 3 I Fluid flow properties. Fluid pressure and rate and state friction parameters. Raw data of experiments conducted on Carrara marble (left column) and limestone gouge (right column) at constant normal stress, σ_n = 21 MPa and different levels of fluid pressure: sub-hydrostatic, λ = 0.15, supra-hydrostatic λ = 0.5, near lithostatic, λ = 0.8. Note the transition from velocity strengthening (a>b) to velocity neutral (a≈b) and the reduction of D_c with increasing fluid pressure.

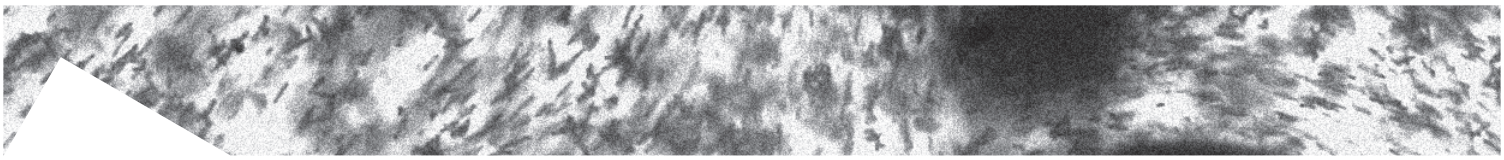

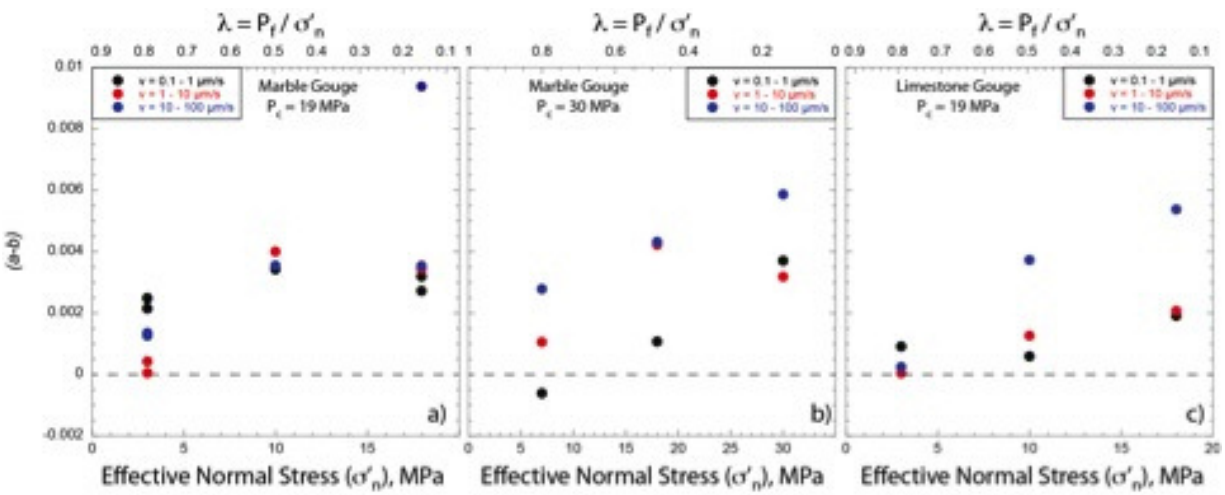

Fig. 4 I (a-b) vs. pore fluid pressure. Evolution of the (a-b) friction parameter as a function of the effective normal stress, σ_n, and pore fluid factor λ. Marble gouge at 19 MPa (a) and 30 MPa (b) of confining pressure, Pc. Limestone gouge at 19 MPa (c) of confining pressure.

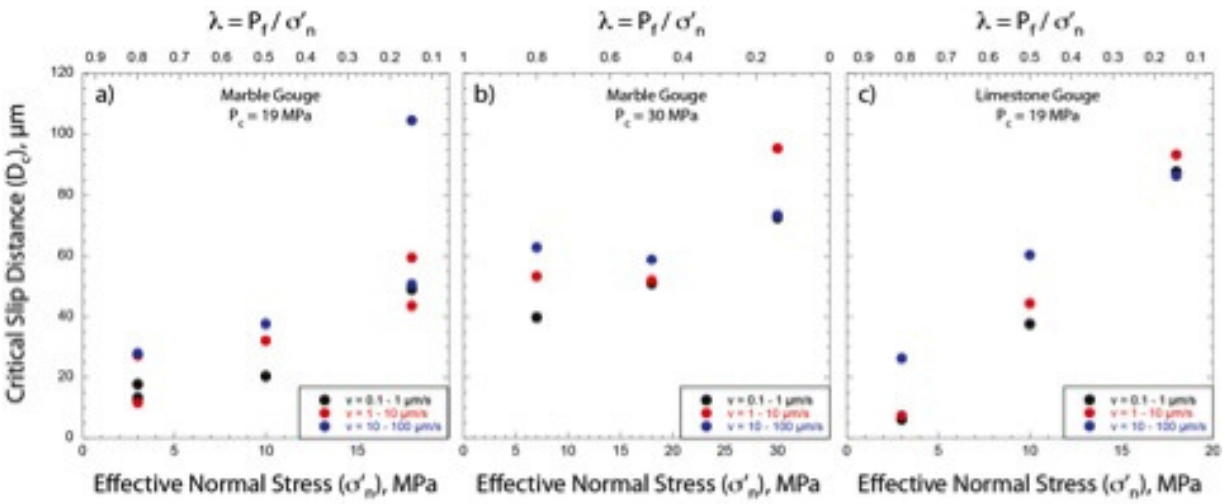

Fig. 5 I Critical slip distance, Dc, vs. pore fluid pressure. Evolution of Dc as a function of the effective normal stress, σ_n, and pore fluid factor λ. Marble gouge at 19 MPa (a) and 30 MPa (b) of confining pressure, Pc. Limestone gouge at 19 MPa (c) of confining pressure.

We have used a biaxial rock deformation apparatus within a pressure vessel, in order to allow a true triaxial stress field, in a double direct shear configuration. We tested carbonate fault gouge, Carrara marble, sieved to a grain size of 125 μm. Normal stresses and confining pressure were held constant throughout the experiment at values of 5 to 40 MPa, and the pore fluid pressure was varied from hydrostatic up to near lithostatic values. Shear stress was induced by a constant displacement rate and sliding velocities varied from 0.1-1000 microns/s, in order to evaluate slip stability via rate- and state- dependent frictional parameters, such as (a-b, Fig. 4), Dc. With increasing fluid pressure we observe an evolution

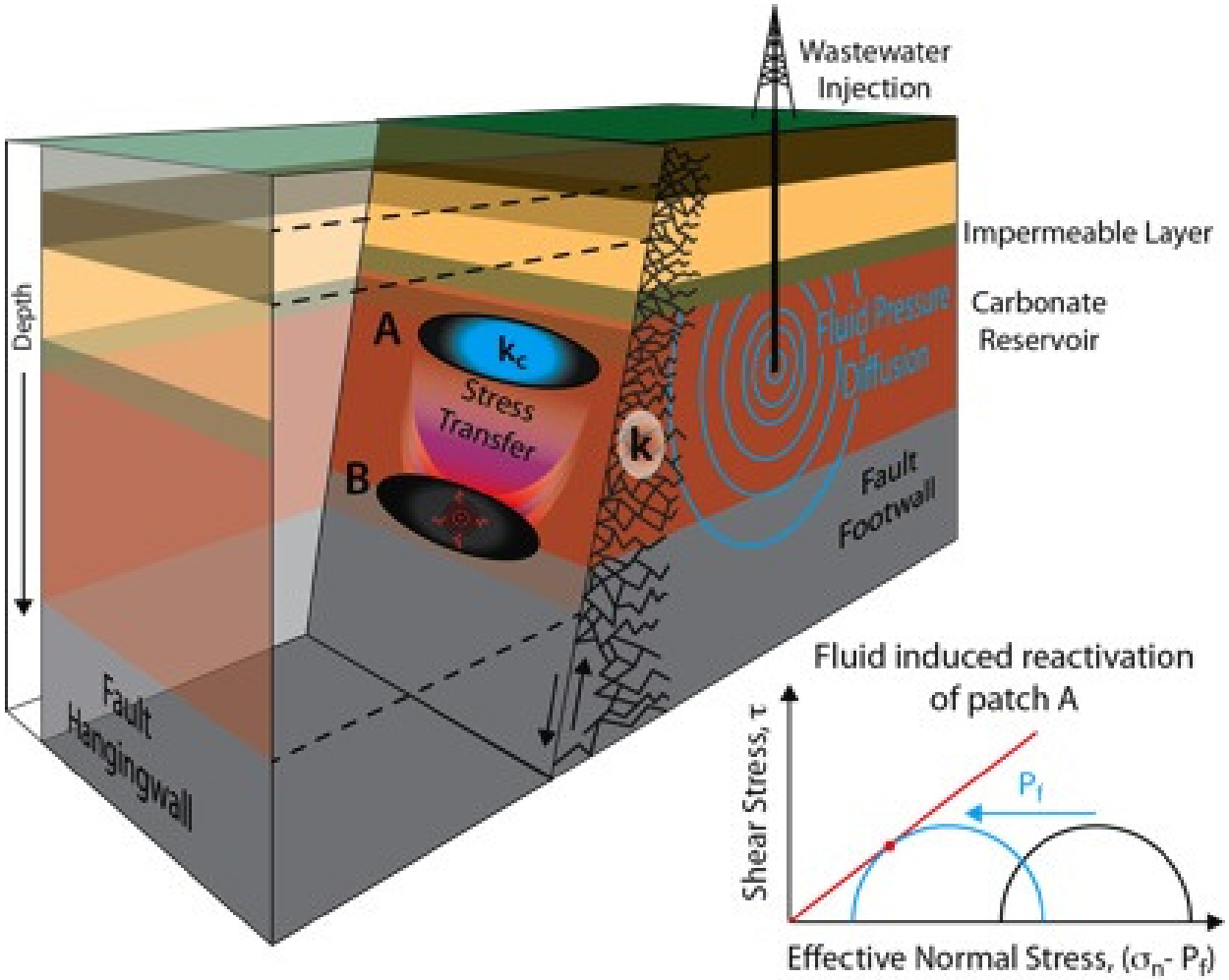

Fig. 6 | Schematic representation of fault reactivation due to fluid overpressure. Two end-members of fault slip behavior promoted by fluid assisted fault reactivation of patch A. Case 1) aseismic reactivation of patch A (slightly velocity strengthening) causes stress transfer and earthquake triggering on patch B (velocity weakening). Case 2) induced seismicity on patch A that due to fluid overpressure has a small Dc and a velocity neutral behavior.

of (a-b) from slightly velocity strengthening to velocity neutral and a reduction in Dc from about 100 to 20 microns. Our analysis on carbonate fault gouges indicates that the increase in fluid pressure not only favour fault reactivation but it also makes the fault more prone to generate earthquake instabilities (Fig. 5, 6 and 7).

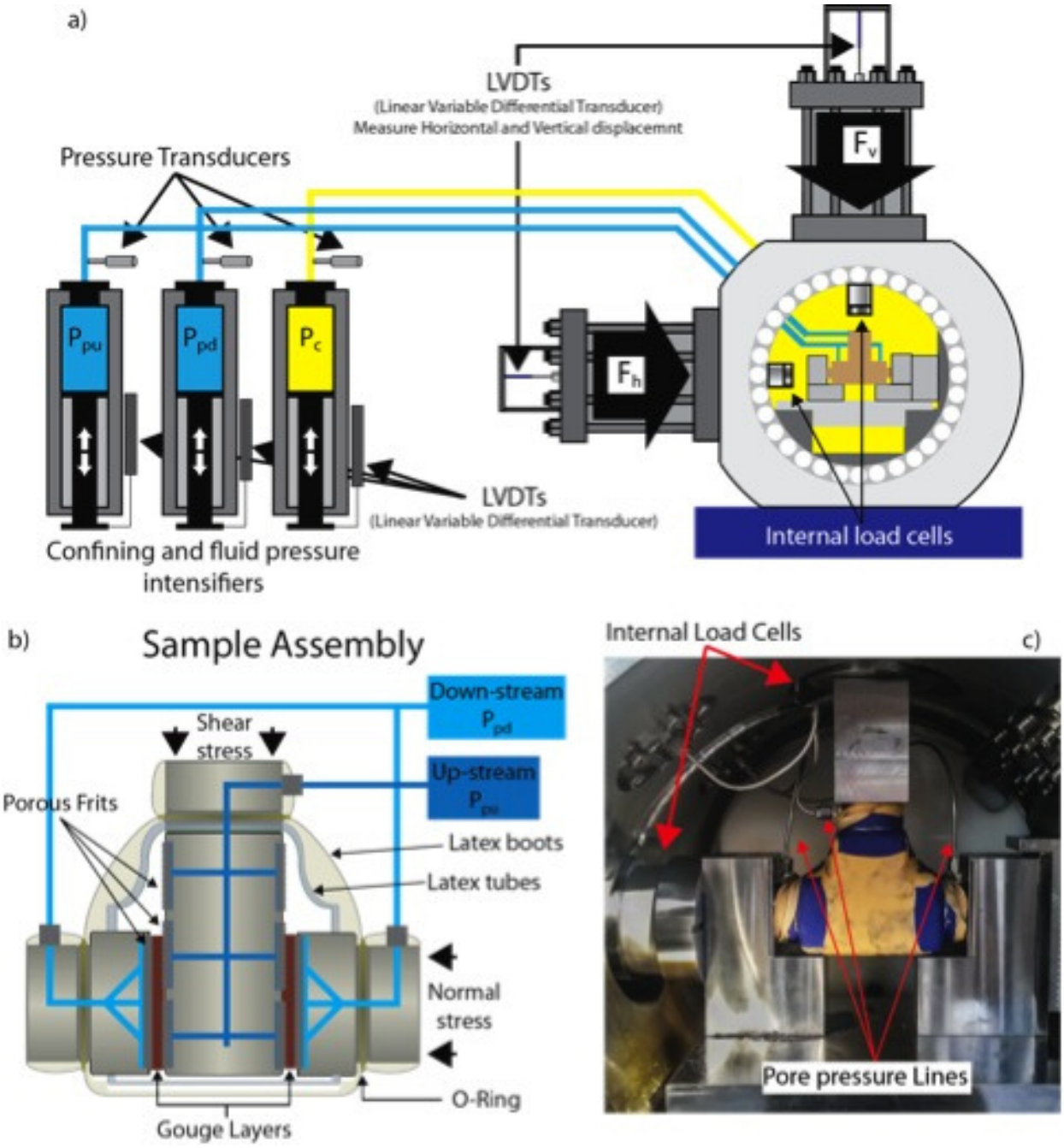

Fig. 7 I Experimental configuration. **(a)** BRAVA apparatus showing the double direct shear configuration within the pressure vessel and the intensifiers used to pressurize pore fluid (Ppu, Ppd) and confining pressure (Pc). **(b)** Details of the sample assembly in the double direct shear configuration for vessel experiments. **(c)** Initial set-up showing the jacketed sample assembly with pore fluid pressure tubing and the internal load cells within the pressure vessel.

Seismic Velocity Changes Across the Transition from Slow- to Fast- Frictional Sliding in Earthquake-Like Laboratory Experiments

M.M. Scuderi, C. Marone, E. Tinti, G. Di Stefano, L. Scognamiglio, J. Leeman, D. Saffer, C. Collettini

Research Line T4

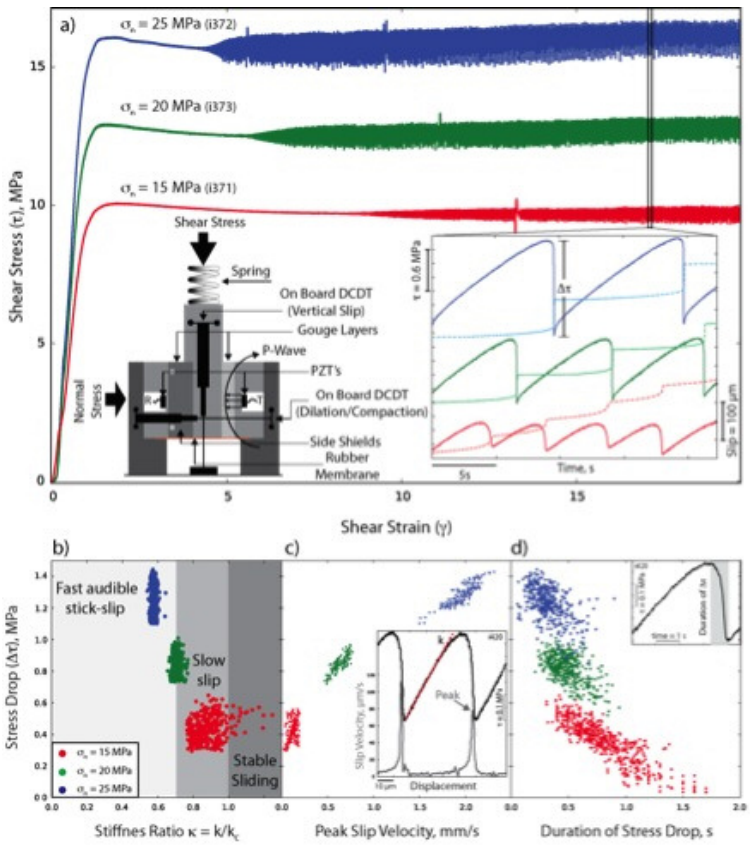

Fig. 1 I The spectrum of fault slip behaviour along experimental faults. (a) Records of shear stress as a function of shear strain for representative experiments at three normal stresses, σn, and a constant shearing rate of 10μm/s. In each case, shear is initially stable and transitions to unstable stick-slip spontaneously. Lower right inset shows detail of slip events (solid line is stress) and the corresponding fault slip (dashed lines) across the transition from slow to fast stick-slip. Lower left inset shows the double direct shear configuration with on-board displacement transducers and PZTs for elastic wave speed measurements. **(b)** Data show the transition from slow to fast stick-slip as mapped in the stability phase diagram. The stiffness ratio, K, controls the magnitude of the stress drop, the peak slip velocity **(c)**, and the slip event duration **(d)**. In panel **(b)** and **(c)** we report data from the 20-30 mm displacement window (see Fig. S1), whereas panel **(d)** shows data from the entire experiment. Inset in panel **(c)** shows the linear fit (red dashed line) to the shear stress curves (black) used to obtain k, along with the record of slip velocity (grey). Inset in panel **(d)** shows a typical failure event and the duration of the stress drop.

Geological and geophysical evidence shows that active tectonic faults slip at different velocities ranging from slow aseismic creep (mm/y) to fast dynamic slip during earthquakes (m/s). Quasi-dynamic slip behaviors have been observed in a wide range of geologic settings, including subduction zone megathrusts and faults within accretionary prisms, continental transforms, in sedimentary basins during fault reactivation induced by hydraulic fracturing, and in non tectonic environments such as landslides and beneath glaciers. Although seismic transients are overwhelming, and may load the locked portion of faults, the underlying mechanism(s) that limit slip velocity evolution is still enigmatic. Here, we describe laboratory shearing experiments designed to investigate stick-slip frictional sliding on experimental faults that undergo a full spectrum of slip behavior ranging from fast stick-slip, to slow slip, to stable sliding. We dictate the stick-slip properties by controlling the stiffness of the testing machine and matching it with the fault frictional rheology (Fig. 1).

We observe systematic variations of the physical properties of experimental faults across the transition from stable sliding to fast, earthquake-like stick-slip. We report continuous measurements of acoustic properties and frictional strength during the complete seismic cycle of loading and stick-slip (Fig. 2). In the initial phase of the seismic cycle, when the slip velocity is near zero, both slow and fast earthquakes exhibit a common evolution characterized by

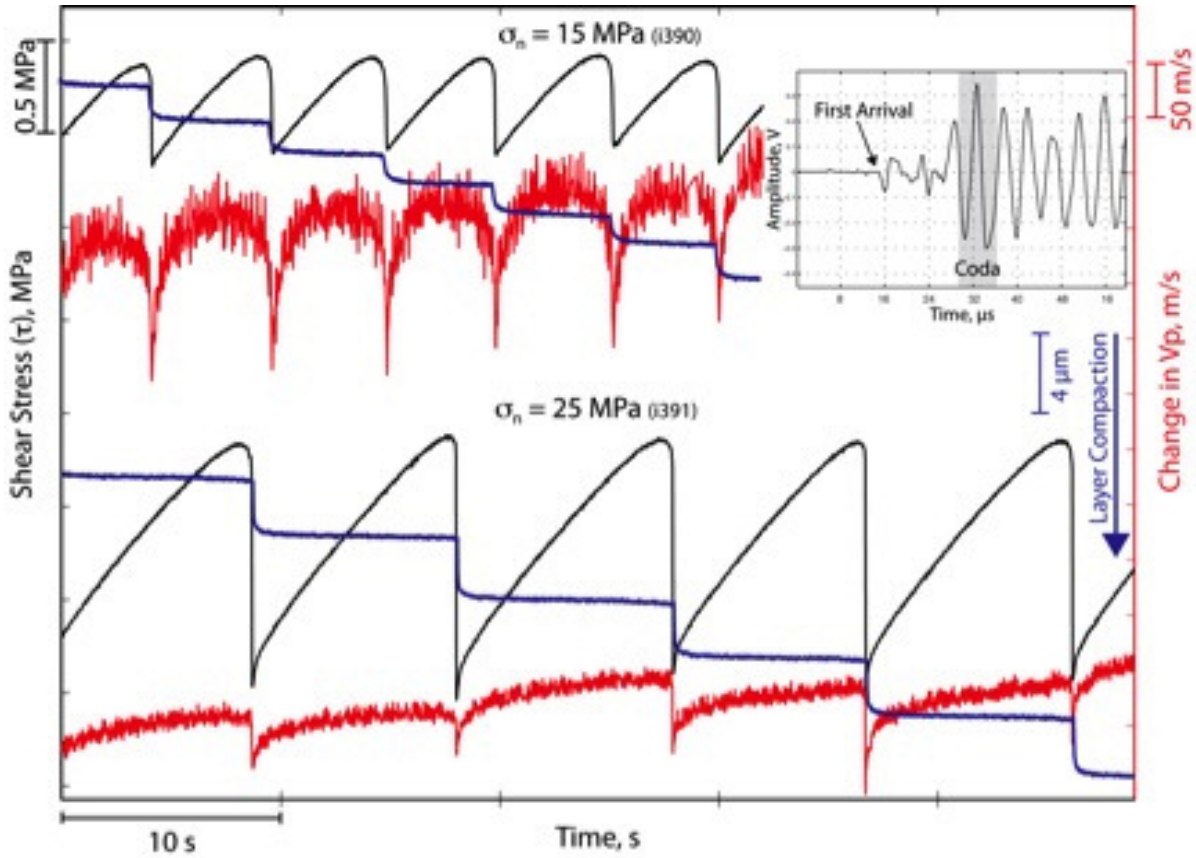

Fig. 2 | Mechanical and P-wave velocity measurements during slow-slip (top) and fast-slip cycles (lower curves). Data show the evolution of shear stress (black), layer thickness (blue) and changes in P-wave velocity (Vp) (red) during the seismic cycle. Inset shows a typical waveform with the P-wave first arrival and the P-coda used to calculate Vp (see Fig. S3 and methods for additional details). Note the consistency in the Vp evolution during the slow and fast stick-slip cycles, mimicking the evolution of shear stress.

increasing P-wave speed and quasi-linear elastic loading. After that, slow earthquakes show marked pre-seismic creep linked to an evident precursory decrease in wave speed that coincides with a deviation of the shear stress from the quasi-linear loading trend. This behavior, which we attribute to the small force imbalance between loading stiffness and fault rheology, promotes low slip velocity and small stress drop during the subsequent stick-slip event. In contrast, fast (earthquake-like) stick-slip events exhibit limited pre-seismic creep and nearly constant wave speed preceding failure. This evolution, coupled with a large force imbalance, favors rapid slip and larger stress drop; in these experiments we measure peak slip velocities of several mm/s. Our observations point to a continuum in fault slip behavior with the evolution from slow to fast earthquake controlled by the fault frictional properties and

the state of stress of both fault and loading medium. Our results also indicate that pre-seismic fault creep favors seismic velocity reduction, suggesting that real time monitoring of active faults may be a powerful tool to detect earthquake precursors (Fig. 3).

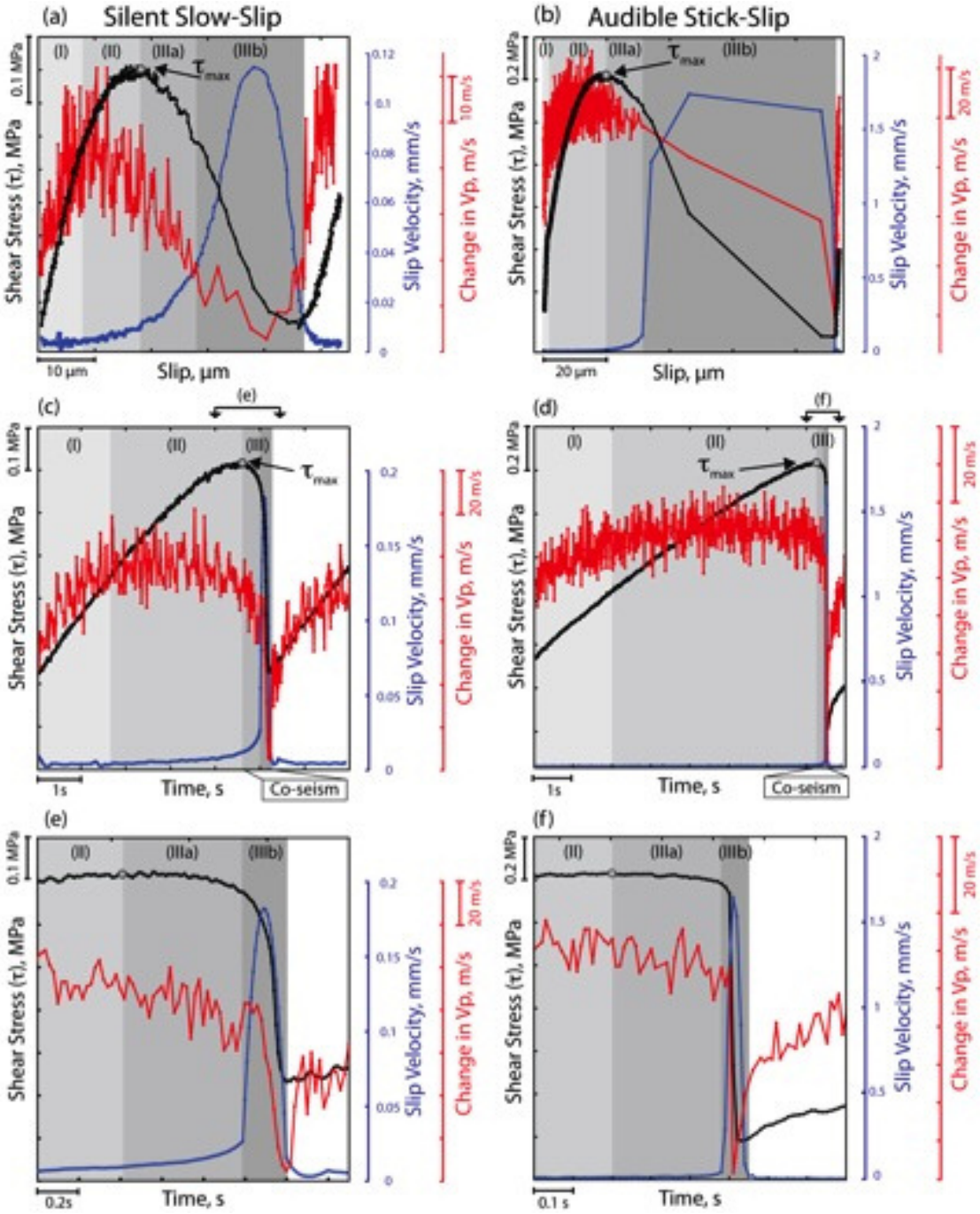

Fig. 3 I Detailed comparison between slow slip and fast stick-slip cycles. Left column in each panel shows silent slow-slip events; right column shows audible stick-slip events. **(a, b)** Events taken at shear displacement of 25 mm, and **(c, d, e, f)** at displacement of 30 mm. The evolution of shear stress (black), slip velocity (blue) and P-wave velocity (red) is shown as a function of: **(a, b)** fault slip and **(c, d, e, f)** time. The grey shaded boxes indicate the three phases of the seismic cycle: (I) inter-seismic, (II) pre-seismic and (III) co-seismic, as described in the text.

Structure of a seismogenic normal fault zone in carbonates: Campo Imperatore, Central Apennines (Italy)

M. Demurtas, M. Fondriest, L. Clemenzi, F. Balsamo, F. Storti, A. Bistacchi, G. Di Toro

Research Line T4

Fault zones cutting carbonate sequences represent significant seismogenic sources worldwide. Most of the earthquakes associated to the L'Aquila 2009 extensional seismic sequence (main shock MW 6.1), probably nucleated and surely propagated through carbonate-bearing rocks. Though seismological and geophysical techniques (e.g., double differences method, trapped waves) allow us to investigate down to the decametric scale the structure of active fault zones, further geological field surveys and microstructural studies of exhumed seismogenic fault zones are required to support interpretation of geophysical data, quantify the geometry of fault zones and identify fault processes active during the seismic cycle. Here we describe the fault geometry and fault zone rock distribution of the footwall-block of the active Campo Imperatore Fault Zone (CIFZ). The CIFZ was exhumed from 2-3 km depth and accommodated a normal throw of 1-2 km since Early-Pleistocene. In the studied area, the CIFZ dips N210/60° and puts in contact Quaternary colluvial deposits in the hangingwall with dolomitized Jurassic platform carbonates in the footwall.

The following structural units were distinguished within the ~300 m thick CIFZ footwall-block, based on density of the fracture/fault network, clast/matrix proportion, preservation of sedimentary features and relative abundance and geometry of veins:

- "cataclastic unit",
- "breccia unit",
- "low-strain damage zone" (mean fracture spacing ~10 cm),
- "high-strain damage zone" (mean fracture spacing <2-3 cm).

The "cataclastic unit" is up to 40 m thick and associated to the master and major faults. Fault rocks are ultra- to cataclasites derived from the progressive deformation of adjacent structural units; shear strain is partitioned among multiple sub-parallel normal faults. Slipping zones include microstructures suggestive of coseismic deformation such as mirror-like slip surfaces with truncated clasts, highly localized sheared calcite veins (Fig. 1), mixed calcite-dolomite foliated cataclasites, fluidized granular layers. The "breccia unit" includes low angle normal faults re-activating pre-existing reverse faults and consists of mosaic-crackle breccias cut by dolomite veins.

The (1) overall distribution of the structural units, (2) the attitude of newly-formed faults and joints, (3) the re-activation of reverse faults inherited from the Miocene-Pliocene compressional phase, are kinematically consistent with the post-Pliocene extensional activity of the CIFZ. The depicted structures compare well with the fault network highlighted by hypocentre relocation of the L'Aquila 2009 seismic sequence.

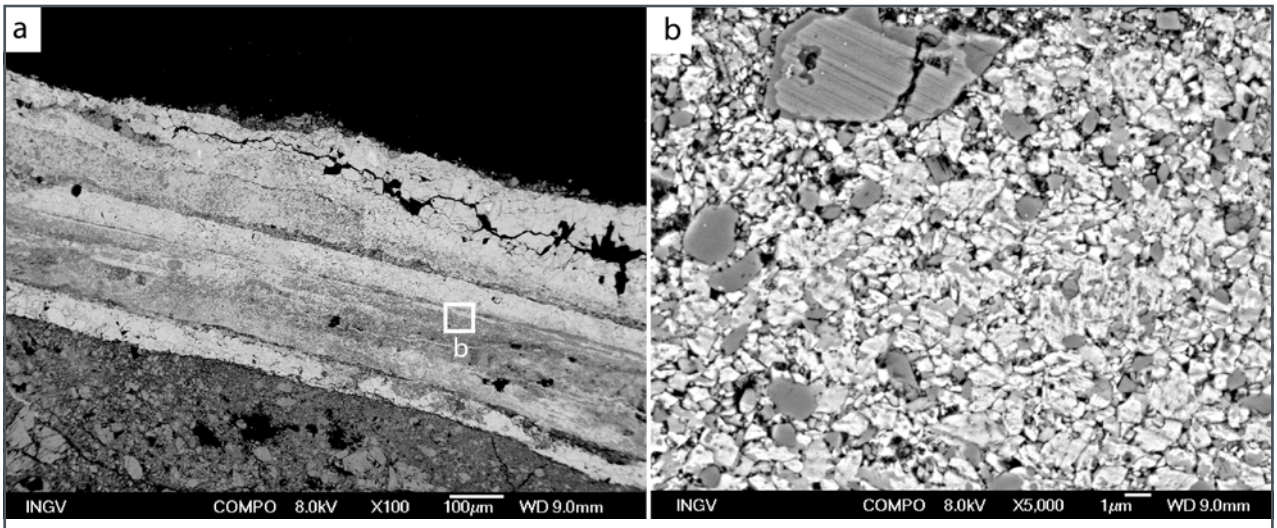

Fig. 1 I Microstructure of the highly localized sheared calcite veins. (a) The slipping zone records succession of multiple vein deposition and then shearing testified by calcite levels accommodating different strain. Here, the last vein precipitation event is preserved and characterized by polygonal calcite crystals up to 150 μm in size and the presence of cavities. (b) Fine grained calcite crystals (typical size of 1 μm) surround rounded micrometric dolomite clasts in high strain domains within calcite sheared veins.

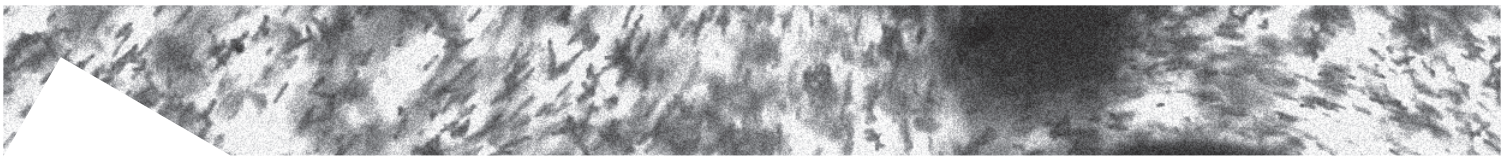

Amorphization and frictional processes in smectite-quartz gouge mixtures sheared from sub-seismic to seismic slip rates

S. Aretusini, S. Mittempergher, E. Spagnuolo, A. Gualtieri, G. Di Toro

Research Line T4

Slipping zones in shallow sections of megathrusts and large landslides are often gouge mixtures of quartz and smectite. Experiments aimed at investigating the frictional processes operating at high slip rates (>1 m s^{-1}) may unravel the mechanics of these natural phenomena. Here we present a new dataset obtained with two rotary shear apparatus (ROSA, Padua University; SHIVA, INGV-Rome). Experiments were performed at room humidity and temperature on four gouge mixtures of Ca-Montmorillonite (Ca-Mnt) and quartz with 60, 50, 25, 0 wt% Ca-Mnt. The gouges were sheared at normal stress of 5 MPa, slip rates 0.0003≤V≤1.5 m s^{-1} and total slip of 3 m. Temperature during the experiments was monitored with four thermocouples and modeled with COMSOL Multiphysics. Deformed gouges were analyzed with quantitative X-ray powder diffraction (Rietveld method) and Scanning Electron Microscopy (FEG-SEM). The resume of all frictional data is presented in (Fig. 1a). For 60 and 50 wt% Ca-Mnt, the friction coefficient μ evolved with slip according to three slip rate regimes: in regime 1 (V<0.1 m/s) initial slip-weakening was followed by slip-strengthening; in regime 2 (0.1<V≤0.3 m s^{-1}) μ was slip-independent; in regime (V>0.3 m/s) μ had strong slip-weakening behavior. Instead, for 25 wt% Ca-Mnt and pure quartz the gouge had a monotonic slip-weakening behavior. Rietveld analysis showed that the production of amorphous material from smectite increased with frictional work and is marked for Ca-Mnt ≥ 50 wt% (Fig. 1b). Microstructural analysis showed for V≤0.3 m s^{-1} and Ca-Mnt ≥ 50 wt% that strain was distributed and the gouge layer pervasively comminuted below 1μm grain sizes (Fig. 1c) while

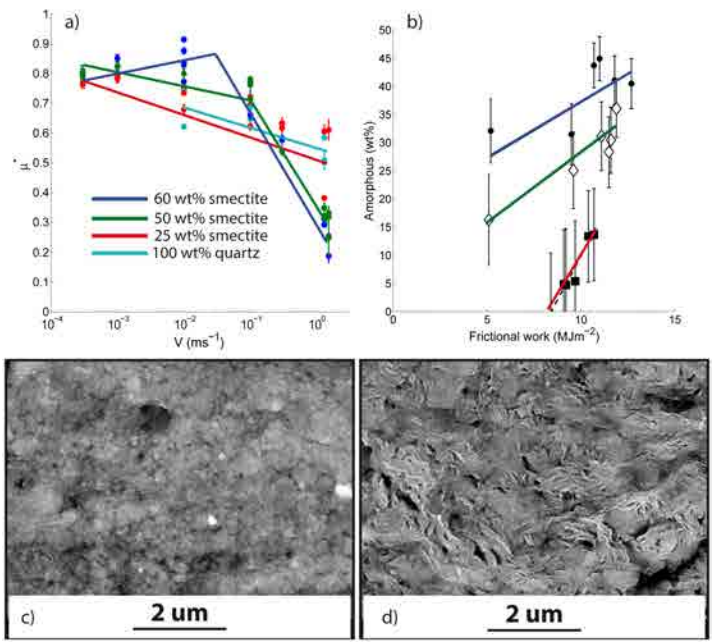

Fig. 1 I Resume of all mechanical data obtained with ROSA and SHIVA experiments. Friction coefficient is plotted as function of the sliding velocity for each of the four gouge tested. (b) The diagram of amorphous content versus frictional work (or the total energy available during the experiments) shows that the quantity of amorphous carbon produced in the experiments increases with mechanical work for all gouges with Ca-Mnt ≥ 25 wt%. Error bar represent amorphous estimate uncertainty.(c) FEG-SEM image of the ultracomminuted/amorphous material, grain sizes are <0.5 μm. d) FEG-SEM image of the dehydrated smectites, evidencing porosity development and elongated crystal shapes.

for $V > 0.3\ ms^{-1}$ strain localization and dehydrated clays occur with frictional heating above 200 °C (Fig. 1d). In conclusion, amorphization process of extreme mechanical comminution of the sheared gouges was not responsible of the measured frictional weakening but is instead work hardening and strain de-localization. On the other hand, frictional weakening is concomitant to strain localization, resulting in frictional heating, dehydration of clays and possible vaporization of water expelled from clays interlayers (thermochemical crystallization and vaporization).

Fault processes in carbonate-bearing rocks at seismic deformation conditions

G. Di Toro, E. Spagnuolo, M. Violay, M. Rempe, S. Smith, S. Nielsen, M. Fondriest, O. Plumper

Research Line T4

Moderate to large earthquakes often rupture and propagate along faults in carbonate-bearing rocks (dolostones, limestones, marbles, etc.). Compared to silicate-bearing rocks, which melt, weaken and wear when sheared at seismic slip rates (ca. 1 m/s), carbonate-bearing rocks do not melt, the minimum friction coefficient can be much lower (down to 5% of static friction) and the wear rate is negligible at seismic slip rates. In cohesive carbonate-bearing rocks, experiments simulating seismic deformation conditions and stopped at slip initiation (<5mm) suggest that initial frictional decay down to 50% of static friction is associated with CO_2 emission plus formation of nanograins and amorphous carbon. Experiments stopped at larger slips (<5 mm) show that the slipping zone consists of a foam-like sintered surface overlying a microporous fabric made of calcite and lime (plus periclase in the case of dolomite) nanograins. In non-cohesive rocks (e.g. gouges) a similar evolution is observed after an initial period of strengthening and strain localization. Experiments with pressurized H_2O show that the contribution of thermal and thermochemical pressurization is negligible in cohesive and questionable in non-cohesive carbonate-bearing rocks. We propose that initial frictional weakening is due to the formation of patches of amorphous carbon (solid lubricant) at asperity contacts. With progressive slip and bulk temperature increase, nanograins accommodate large

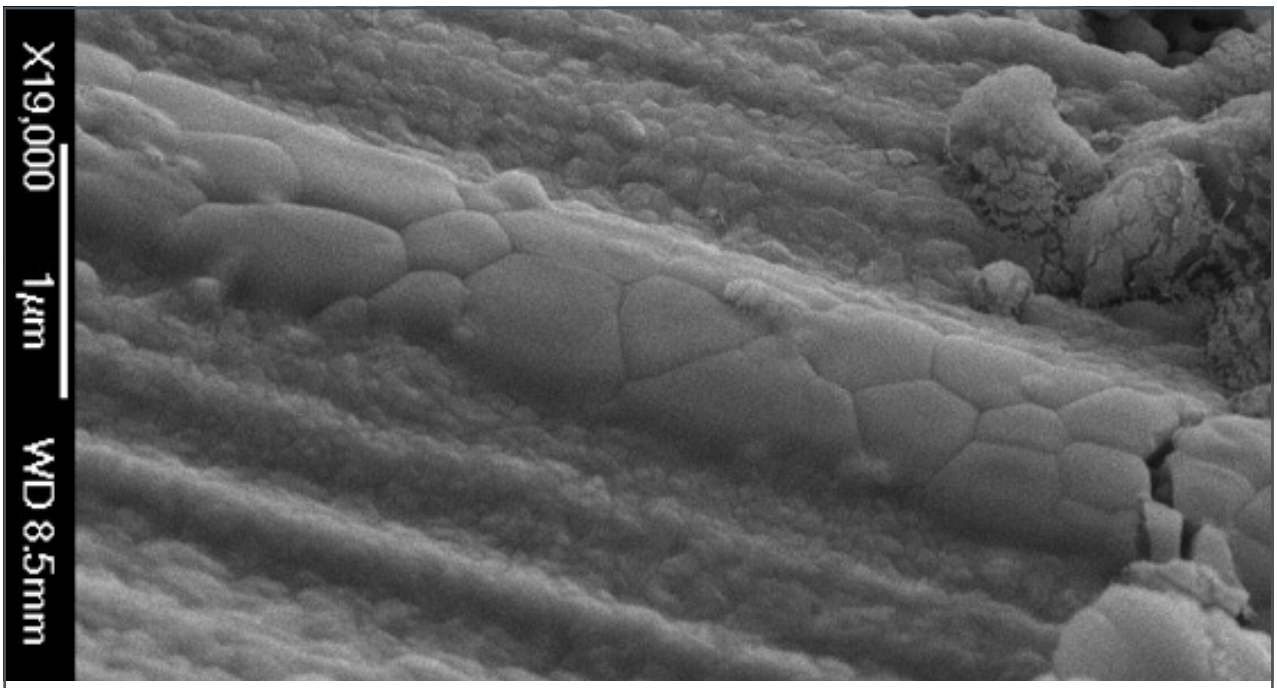

Fig. 1 | Slip surface in Carrara marble produced with the rotary shear machine SHIVA installed at the HT-HP laboratories at INGV-Rome. The calcitic marble was slid for 5 meters at seismic slip rates of 3 m/s under a normal stress of 20 MPa. The foam-like pavement made of plates about 1-2 micrometer in size and covering the slip surface is interpreted as due to sintering of calcite and lime nanograins during fast cooling at the end of slip. Similar features have been found in natural mirror fault surfaces cutting limestones and dolostones in the Southern Alps and in the Apennines.

strain rates (ca. 104 s^{-1}) by grain boundary sliding as suggested by several authors. The presence of a microporous fabric boosts pore-controlled diffusive process propelled by CO_2 gas exhaust due to decarbonation. Enhanced pore-controlled diffusive processes allow (1) efficient mass transfer during grain boundary sliding and (2) sintering of the nanograins into a foam-like slip surface at the end of the experiment (Fig. 1).

Frictional instabilities and mineral carbonation of basalts triggered by injection of pressurized H_2O - and CO_2- rich fluids

P. Giacomel, E. Spagnuolo, A. Marzoli, M. Nazzari, N. Youbi, G. Di Toro

Research Line T4

Mineral carbonation of continental flood basalts by underground injection is a technique proposed for long-term storage of anthropogenic CO_2. But the injection of pressurized fluids may result in induced seismicity. Here we discuss the effects of the injection of pure CO_2, distilled H_2O and H_2O+CO_2 fluid mixtures on basalt-built experimental faults. The experiments reproduced the stress conditions (normal stress <15 MPa) of the pilot projects for CO_2 storage that exploit natural reservoirs located at few hundreds of meters depth. Since mineral carbonation requires the injection of H_2O+CO_2 fluid mixtures (or of pure CO_2 in water reservoirs), the efficiency of the storage technique is limited by the low solubility of CO_2 in H_2O (30-70 g of CO_2 per kg of H_2O at the reservoir temperatures and depths).

We performed 10 friction experiments at room temperature on pre-cut basalts samples (50/30 mm external/internal diameter) with the rotary shear apparatus SHIVA. The basalts had a different degree of alteration determined with optical microscope, X-ray fluorescence and diffraction analysis. Samples were first pre-loaded to 15 MPa normal stress and to 5 MPa shear stress at an initial fluid pressure of 2.5 MPa; then, fluid pressure was increased of 0.1 MPa every 100 s to induce fault instability. The "main" fault instability corresponded to the slip episode with slip rate V > 0.3 m/s. The instability resulted from the unbalance between the imposed shear stress (5 MPa) and the time-dependent fault shear strength. The latter decreased with time because of (1) the step-increase of the fluid pressure and, (2) the chemical evolution of the sliding surface. In experiments performed with distilled H_2O and H_2O+CO_2 fluids and, to a less extent, with pure CO_2, the main instability

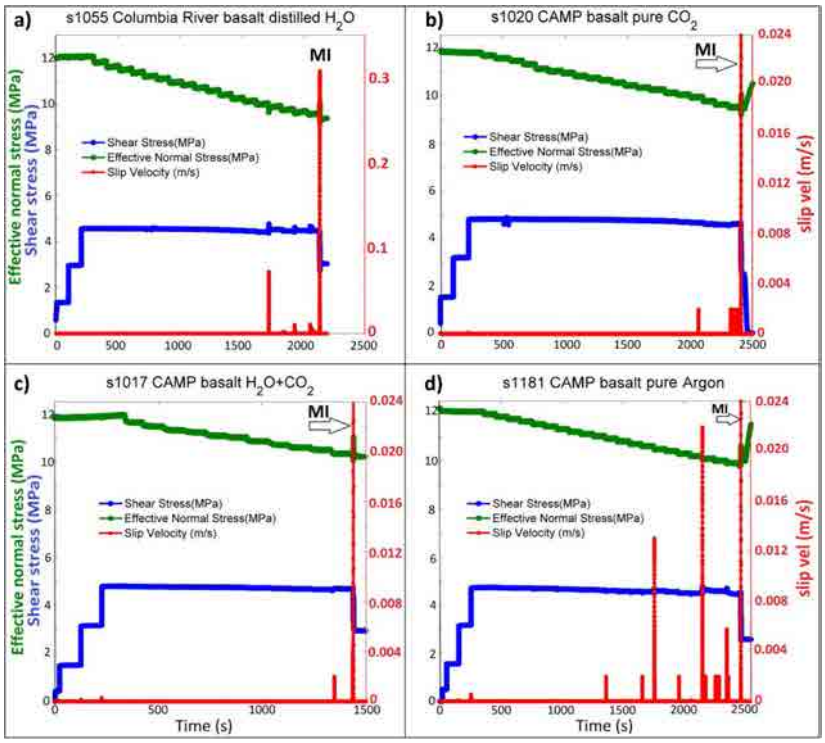

Fig. 1 I Typical experiments conducted under fluid pressure control at constant τ (blue in color curve) and σn (not shown) in the case of: (a) distilled H_2O, (b) pure CO_2, (c) H_2O+CO_2 mixture and (d)pure Argon. In all the experiments Pf was increased stepwise resulting in a decreasing σneff (green curve) to trigger the main instability MI. Short living slip bursts (red curve), emphasized by the increased scale of the ordinate axis in Figs. (b) to (d), were recorded before the onset of the MI. At MI the slip velocity was limited to 0.3 m/s.

was preceded by creep and short living slip bursts with 0.001< V <0.3 m/s. The main instability occurred at higher fluid pressures (1) in less altered basalts (regardless of the fluid composition) and, (2) in pure CO_2 fluids given the same degree of alteration of the basalts.

Fluids collected after the experiments were analysed with ion-chromatography and the sliding surfaces investigated with Micro-Raman spectroscopy. The fluids recovered from the experiments with H_2O+CO_2 mixtures had a 2- and 5-fold increase of Mg^{2+} and Ca^{2+} concentration, respectively, with respect to those performed with distilled H_2O. Only in the case of the H_2O+CO_2 fluid mixture experiments, the release of Mg^{2+} and Ca^{2+} resulted in the precipitation of dolomite and calcite grains (i.e., mineral carbonation).

Our experimental dataset suggests that fault instability is controlled both by the chemical composition of the fluid and the state of alteration of the basalt. The precipitation of calcite and dolomite in our short-in-duration experiments implies that mineral carbonation is an efficient mechanism for CO_2 long-term underground storage. However, the low solubility of CO_2 in water requires the injection of large quantities of fluid to store a significant amount of CO_2, increasing the hazard associated to induced seismicity (Fig. 1).

Influence of calcite decarbonation on the frictional behavior of carbonate-bearing gouge: Implications for the instability of volcanic flanks and fault slip

B.M. Carpenter, S. Mollo, C. Viti, C. Collettini

Research Line T4

The impact of heat, readily provided by magma, circulating hot fluids, or rapid fault slip on carbonate substrata is an important factor in determining the flank stability of volcanoes and the mechanical behavior of faults in areas where carbonate lithologies are prevalent. The mineralogy and mechanical properties of carbonate rocks are demonstrably altered by thermally induced decarbonation. While previous studies have considered the role of decarbonation in bulk strength loss at subvolcanic conditions and dynamic weakening during coseismic fault slip, little is known about the effects of decarbonation on the frictional properties of carbonate rocks during both the nucleation and inter-seismic phases. Here, we present results from experiments performed on a portlandite-rich material, a typical hydrous product of the decarbonation reaction. To evaluate frictional strength, stability, and healing at shallow crustal conditions, we sheared gouge layers of this material under saturated conditions at room temperature and at velocities comparable to those involved in earthquake nucleation. Our data indicate that the reaction of calcite to portlandite results in a distinct change in the mechanical behaviour of the gouge. Decarbonated shear zones are (1) frictionally weaker at higher normal stresses, (2) more frictionally unstable, and (3) likely to regain their frictional strength more quickly than unaltered calcite-rich zones. The occurrence of portlandite could be key for interpreting the stability of volcanic flanks that root into carbonate substrata and for seismogenic normal faults located within thick sedimentary sequences, and thus provide a better understanding of the hazards they pose (Fig. 1).

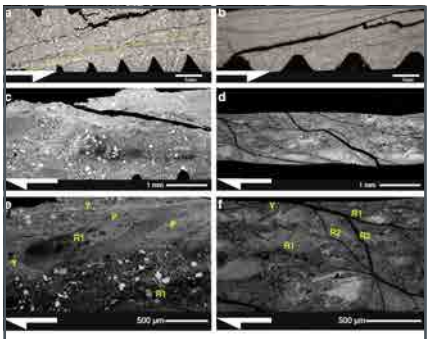

Fig. 1 I Backscattered electron (BSE) SEM images of our experimental samples, calcite (a) and portlandite (b, c), at 1 MPa. Yellow line in (a) traces interpreted R1 shear plane. Portlandite images, (b, c), show fine-ultrafine portlandite-rich shear zones (pale grey), and relic calcite grains (white). SEM/BSE images of our experimental samples, calcite (d) and portlandite (e, f), at 50 MPa. On all images, arrows show shear direction along bottom of the sample.

Real-time setup to measure radon emission during rock deformation: implications for geochemical surveillance

P. Tuccimei, S. Mollo, M. Soligo, P. Scarlato, M. Castelluccio

Research Line T4

Laboratory experiments can represent a valid approach to unravel the complex interplay between the geochemical behaviour of radon and rock deformation mechanisms. In light of this, we present a new real-time experimental setup for analysing in continuum the alpha-emitting ^{222}Rn and ^{220}Rn daughters over variable stress–strain regimes (Fig. 1). The most innovative segment of this setup consists of the radon accumulation chamber obtained from a tough and durable material that can host large cylindrical rock samples. The accumulation chamber is connected, in a closed-loop configuration, to a gas-drying unit and to a RAD7 radon monitor. A recirculating pump moves the gas from the rock sample to a solid-state detector for alpha counting of radon and thoron progeny. The measured radon signal is enhanced by surrounding the accumulation chamber with a digitally controlled heating belt. As the temperature is increased, the number of effective collisions of radon atoms increases favouring the diffusion of radon through the material and reducing the analytical uncertainty. The accumulation chamber containing the sample is then placed into a uniaxial testing apparatus where the axial deformation is measured throughout a linear variable displacement transducer. A dedicated software allows obtaining a variety of stress–strain regimes from fast deformation rates to long-term creep tests. Experiments conducted with this new real-time setup have important ramifications for the interpretation of geochemical anomalies recorded prior to volcanic eruptions or earthquakes.

Fig. 1 | Experimental setup for the detection of ^{222}Rn and ^{220}Rn activity concentrations from rocks under uniaxial deformation. The system consists of: rock sample (1), DryPack accumulation chamber (2), digitally controlled heating belt (3), desiccant (4), RAD 7 radon monitor (5), uniaxial press (6), and vinyl tubing (8). Arrows connect the different sections of the experimental system to give a complete view of it.

Pressure solution inhibition in a limestone–chert composite multilayer: Implications for the seismic cycle and fluid flow

L. Petracchini, M. Antonellini, A. Billi, D. Scrocca, F. Trippetta, S. Mollo

Research Line T4

Pressure solution seams (PSSs) are frequent features in carbonate rocks undergoing tectonic shortening. In particular, pervasive, anticline-axis-parallel, bed-normal PSSs are known to develop during layer-parallel shortening of (marly) carbonate rocks in fold-thrust belts. These pressure solution features can impact subsequent fracture development, fluid circulation, and strain localization including the seismic cycle. It is here demonstrated that the occurrence of frequent and continuous chert layers may strengthen a limestone sequence and inhibit pressure solution under layer-parallel-shortening. Field observations and laboratory determinations are reported from marly limestone with continuous chert layers of the Scaglia Fm. (Cingoli anticline, northern Apennines, Italy) exhumed from a depth of c. 1 km. In these outcrops, bed-normal solution seams do not occur or they occur only where infrequent chert layers have been shortened by small thrusts. In analogy with laminae-reinforced composite materials, a model is developed explaining the field observations with the strengthening effect of chert in the chert–limestone composite multilayer. During layer-parallel-shortening, the composite multilayer deforms under equal strain boundary conditions. In this situation, the tectonic load is mostly supported by the stiff and frequent chert layers and the strain of the whole chert–limestone composite remains in the elastic field, so that pressure solution seam development is prevented in the limestone beds. Our model may be applied down to a depth of a few kilometers in the upper crust that is relevant for the seismic cycle and fluid flow (Fig.1).

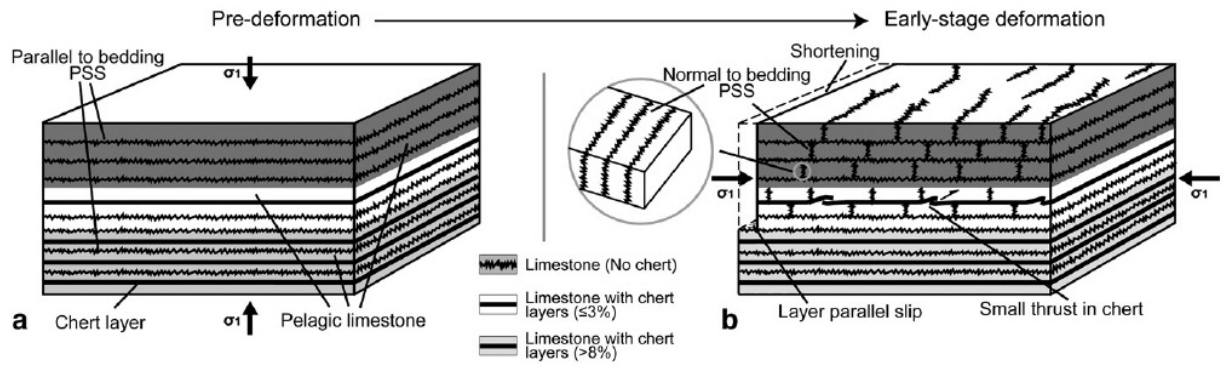

Fig. 1 I Conceptual model. (a) Bed-parallel stylolite formation during syn-sedimentary burial of the Scaglia Fm. (with and without chert layers). (b) Bed-normal PSSs formation vs. during layer-parallel-shortening depending on the absence vs. presence of chert layers, respectively, in the Scaglia Fm.

Study of the characteristic behaviour of active/exhumed faults Vs large scale gravitative movements sliding planes in central Italy

M. Moro, M. Nazzari, E. Spagnolo, A. Cavallo, F. Doumaz, E. Falcucci, S. Gori, M. Saroli, L. Lo Sardo, T. Tesei, P. Scarlato

Research Line T2

The aim of the project points to understand the specific behaviour, "by analysing the microstructures" using the scanning electron microscope, on samples collected on various displacement planes. Faults/sliding planes in bedrock attributed to active and capable faults or deep-seated gravitational slope deformations in central Italy are the considered deformation structures in our analysis phase of this project.

In many European active zones, destructive earthquakes nucleate and propagate affecting thick sequences of carbonate-bearing rocks. The active normal faults of the central Apennines are commonly divided into two parallel sets, a western set and an eastern one. Some of the strongest historical earthquakes have been attributed to the rupture of the western set of normal faults in the central Apennines, such as the 1349 (Mw 6.6), 1703 (Jan. 14; Mw 6.7), 1703 (Feb. 2; Mw 6.7) and 1915 (Mw 7.0) events, by comparing the pattern of the active faults, the damage distribution related to these seismic events and paleoseismologically-inferred data. In contrast, the eastern active normal faults have not been activated in historical times and are therefore considered to be probable seismic gaps.

Some of the fault planes recognized in central Apennines are attributed to inactive structures, exhumed by erosion whereas other planes in bedrock are due to the presence of deep-seated gravitational slope deformations. To discriminate the relative geological processes associated to rock fault/sliding planes we will study the information coming out from the observed microstructures in order to detect any signature showing a systematic deformation family style.

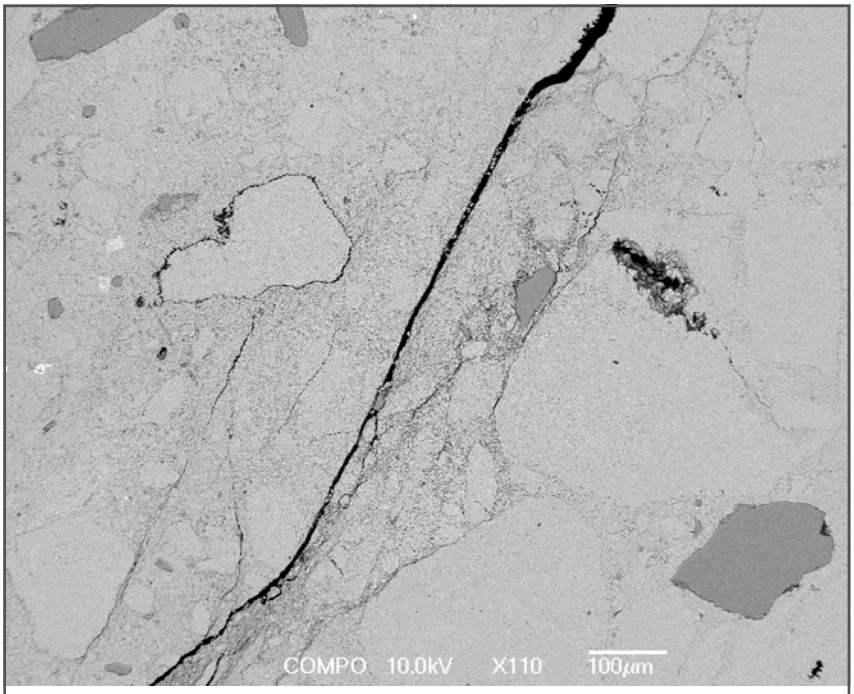

Fig. 1 I FESEM image of the "Alto di Cacchia" DGSD sliding plane.

The microstructural features of the gouge layers on natural and experimental samples will be investiga-

ted using FESEM as image analysis techniques, and by electron microprobe for chemical mapping analysis. As a first case study analysed during 2015 we selected the DGSD of the "Alto di Cacchia" structure (Fig. 1), that will be compared with the other case studies.

Fault strength in thin-skinned tectonic wedges across the smectite-illite transition: Constrains from friction experiments and critical tapers

T. Tesei, B. Lacroix, C. Collettini

Research Line T4

The strength, shape and ultimately seismic behavior of many thin-skinned fold-and-thrust belts, including marine accretionary wedges, are strongly controlled by large-scale faults that develop from weak, clay-rich sedimentary horizons (décollements). The increase of temperature with depth along clay-rich faults promotes the so-called smectite-illite transition that may influence the fault strength, fluid distribution and possibly the onset of seismicity. Here we report on the frictional properties of intact fault rocks retrieved from two large décollements, which have been exhumed from depths above and below the smectite-illite transition. We find that all tested rocks are characterized by very low friction (μ=0.17-0.26), velocity-strengthening behavior and low rates of frictional healing suggesting long-term fault weakness. Combining our experimental results to the Critical Taper theory we computed the effective friction F of megathrusts beneath several accretionary wedges around the world, which result extremely low (0.03< F <0.14) and in agreement with other independent estimates. Our analysis indicates a long-term weakness that can explain the shape of several tectonic wedges worldwide without invoking diffuse near-lithostatic fluid overpressures (Fig. 1).

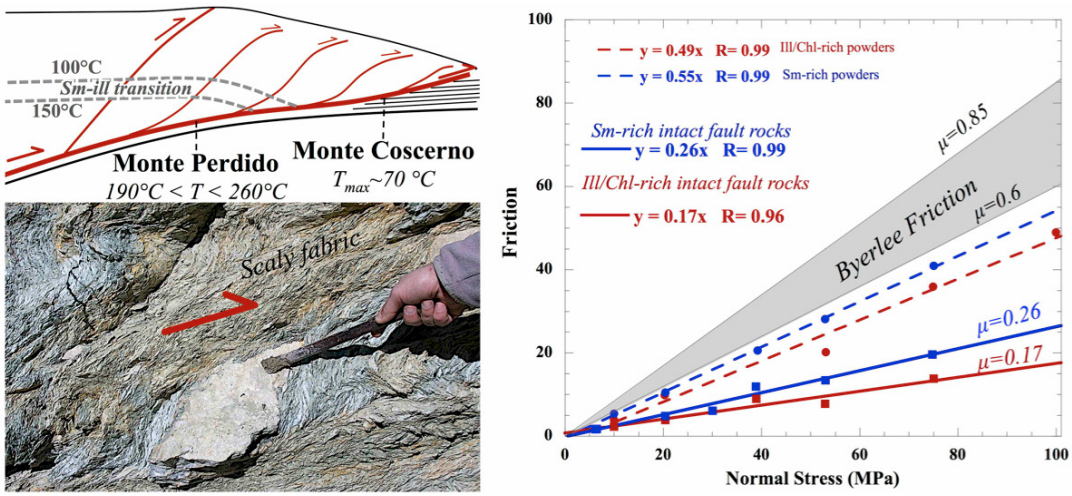

Fig. 1 | The Monte Coscerno and Monte Perdido thrusts represent fault zones in weak horizons exhumed from above and below the Smectite-Illite transition. These rocks are characterized by pervasive and interconnected clay-rich foliation defining a typical scaly fabric. Friction of intact fault rock wafers is remarkably low and weakness is maintained across the Smectite-Illite transition..

Early weakening processes inside thrust fault

B. Lacroix, T. Tesei, E. Oliot, A. Lahfid, C. Collettini

Research Line T4

Observations from deep boreholes at several locations worldwide, laboratory measurements of frictional strength on quartzo-feldspathic materials and earthquake focal mechanisms indicate that crustal faults are strong (apparent friction $\mu \geq 0.6$). However, friction experiments on phyllosilicate-rich rocks and some geophysical data have demonstrated that some major faults are considerably weaker. This weakness is commonly considered to be characteristic of mature faults in which rocks are altered by prolonged deformation and fluid-rock interaction (i.e. San Andreas, Zuccale, and Nankai faults). In contrast, in this study we document fault weakening occurring along a marly shear zone in its infancy (<30 m displacement). Geochemical mass balance calculation and microstructural data show that a massive calcite departure (up to 50 vol%) from the fault rocks facilitated the concentration and reorganization of weak phyllosilicate minerals along the shear surfaces. Friction experiments carried out on intact foliated samples of host marls and fault rocks demonstrated that this structural reorganization lead to a significant fault weakening and that the incipient structure has strength and slip behavior comparable to that of the major weak faults previously documented. These results indicate that some faults, especially those nucleating in lithologies rich of both clays and high-solubility minerals (such as calcite) might experience rapid mineralogical and structural alteration and become weak even in the early stages of their activity (Fig. 1).

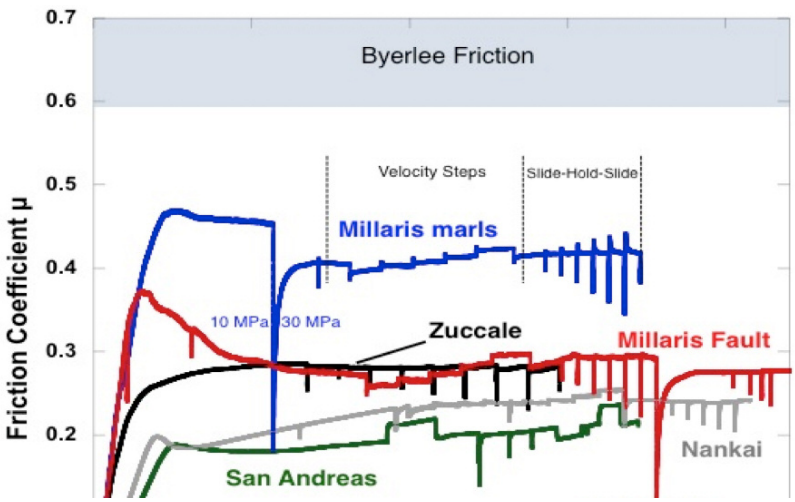

Fig. 1 I Friction of an low-displacement thrust (Millaris Fault) is similar to the friction of large-displacement weak faults (San Andreas fault, Zuccale low-angle normal fault, Nankai thrust).

8.3 TECHOLOGY

Airborne payloads

G. Romeo, A. Iarocci, G. Di Stefano, G. Caramelli, A. Sciarra, F. Di Felice

Research Line IT2, A6, A7

In the frame work of the LusiLab project LNTS developed some payloads suitable for drone use. These payload have been designed to explore the huge hydrothermal manifestation in East Java, who affected 7.5 square Km, causing the evacuation of more than 40000 persons. An easy cost effective and safe way to explore the crater is by using a specially equipped drone. LNTS developed the following instruments:

- Multiple bottle gas sampler
- Gas analyzer
- Mud sampler
- parachutable buoy with releaser
- automatic winch with mud sampler

all these devices use the same mechanical and electrical interfaces for easy field operations. The electrical interface provides the power supply, derived from the drone main battery, and the connection to the autopilot and to the radio. This allows all the devices to be operated manually, by the ground station operator, or automatically, associating the operation to a waypoint.

Multiple bottle gas sampler

This device (Fig. 1) is based on the well known Isotube® bottles, especially designed for gas sampling. The device, depicted in picture, allows 6 pre-evacuated bottles to be opened sequentially during a flight. A microcontroller receives the signal from the drone autopilot and operates a servomotor (the device has 3 servos for 6 bottles) to open the bottle valve for 2 seconds, enough to fill the bottle with the atmosphere. 6 LEDs (one for bottle) indicate the exposed bottles. The processor avoids multiple exposures until reset. The bottle replacement is quite easy: just unscrewing the exposed bottles, screwing in the empty ones and reset the processor. A successfully reset is indicated by the LEDs blinking.

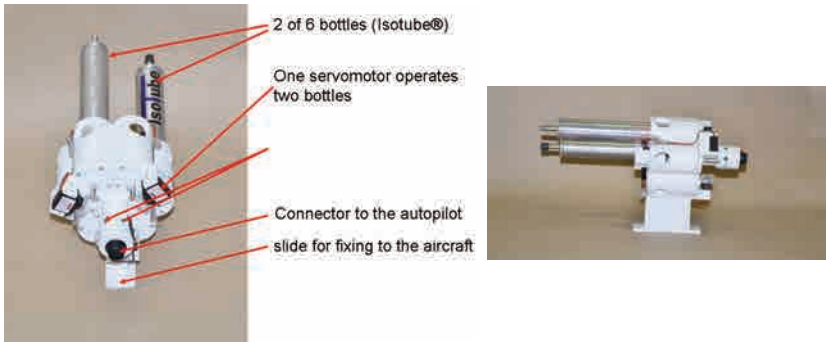

Fig. 1 I Two images of the Isotube® based 6 bottles gas sampler.

Radio thermometer buoy

This devices has been thought and built to measure the temperature and track the movement of the mud near the LuSi crater. The buoy, a waterproof cylinder containing a thermometer, a GPS and a radio transceiver continuously sends the temperature and GPS position using a radio link. The builtin battery pack can power the system for one day. Figure 2 shows the external aspect of the buoy.

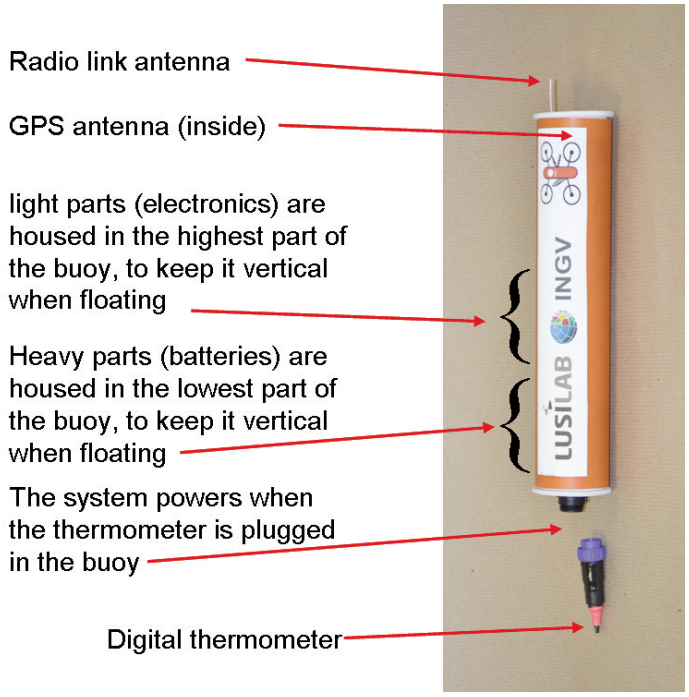

Fig. 2 I The radio thermometer buoy.

The buoy is deployed by a drone, using a releaser designed on purpose. The releaser is a box, containing the folded parachute and a servomotor operated by a built in processor. This processor communicates with the drone remote control or with the autopilot to release the buoy over the desired target.

The releaser is depicted in Figure 3. Figure 4 shows the test, conducted in the INGV backyard.

The LusiDrone (a commercial s800 equipped with the required electrical and mechanical interfaces) releases the buoy, and the sequence of 3 snapshots shows the parachute opening.

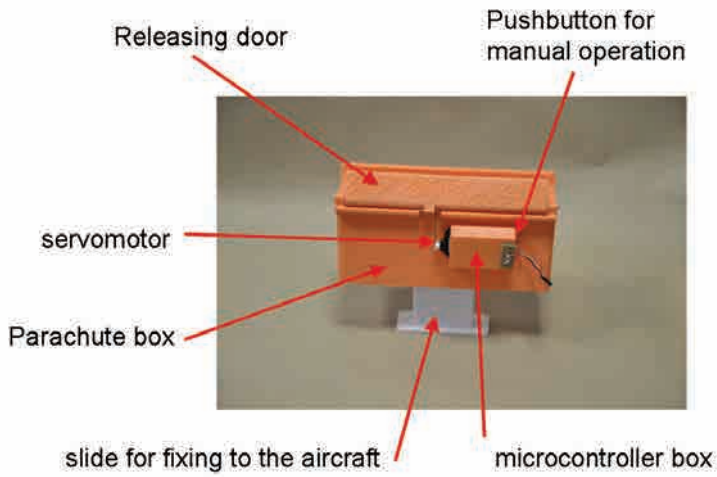

Fig. 3 I The buoy releasing device. It is essentially a box containing the parachute and the buoy, that can be released operating a door through a servomotor. A microprocessor interfaces the servomotor to the drone radio or to the autopilot.

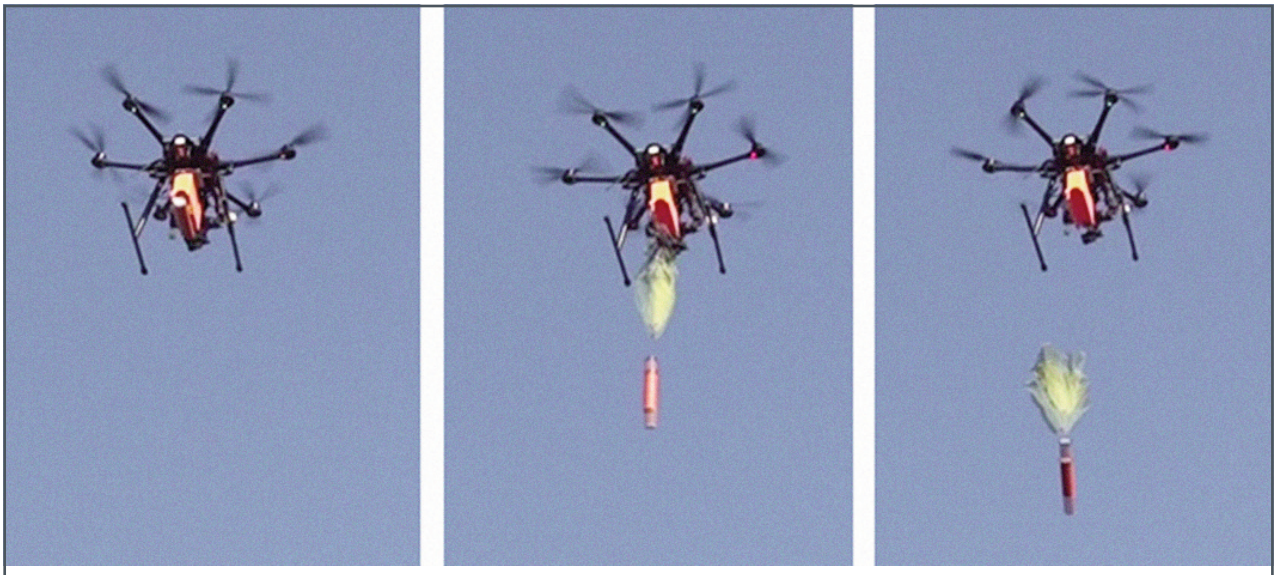

Fig. 4 I Buoy release operation. The three snapshots show the drone hovering over the target and releasing the parachute. The parachute deployment is extremely fast, because it is only lightly folded in the large box provided on purpose, an requires less than two meters. The impact speed is less than 5 m/s.

Automatic winch with sampler

Ground sampling may be a dangerous task for an aerial drone. To allow ground sampling LNTS developed a automatic winch which allows the drone just to hover while the winch performs the task.

A built-in microprocessor operates a the winch motor by monitor and controlling torque and speed. In this way the

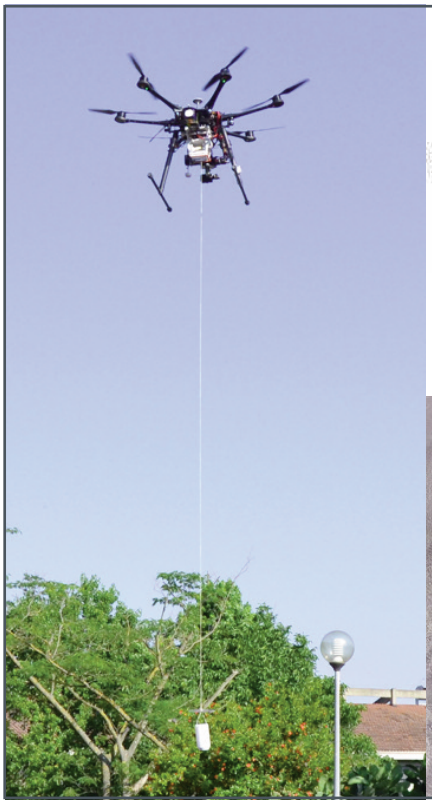

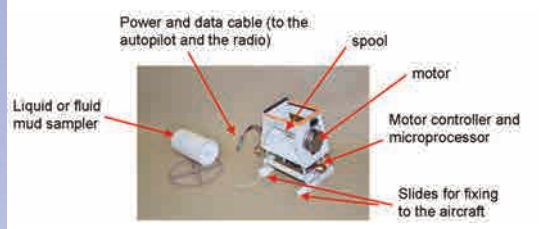

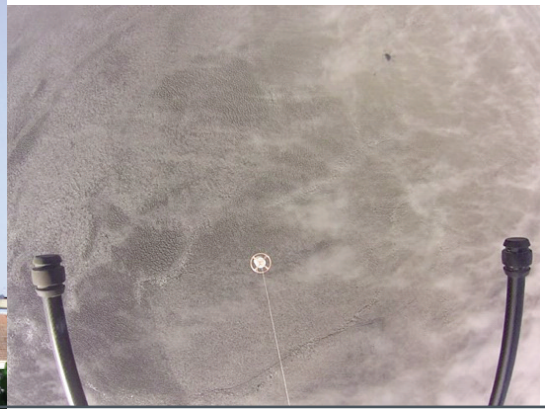

Fig. 5 I The automatic winch. Connected to the drone autopilot this device allows the automatic sampling of liquid and mud, while the drone just hovers over the target (upper photo). Left photo: testing the sampler connected to the drone in the INGV's backyard. Bottom photo: a photograph of the winch operation, taken by the drone built-in camera, during the operation over LuSi.

winch can deploy the sampler until it touches the surface, but, at same time keeping the rope taut to avoid interferences with the drone flight. After sampling the rope is recovered and the drone brings back the sample. In case the sampler gets entangled to the ground, the operator can release the entire spool (a disposable part) saving the drone. Figure 5 (bottom) shows the winch during a test in the INGV backyard.

Geiger counter

The Geiger counter use the Townsend avalanche phenomenon to produce an electronic pulse from even a single ionising event in a gas discharge chamber. It can be used for the detection of gamma radiation, X-rays, and alpha and beta particles.

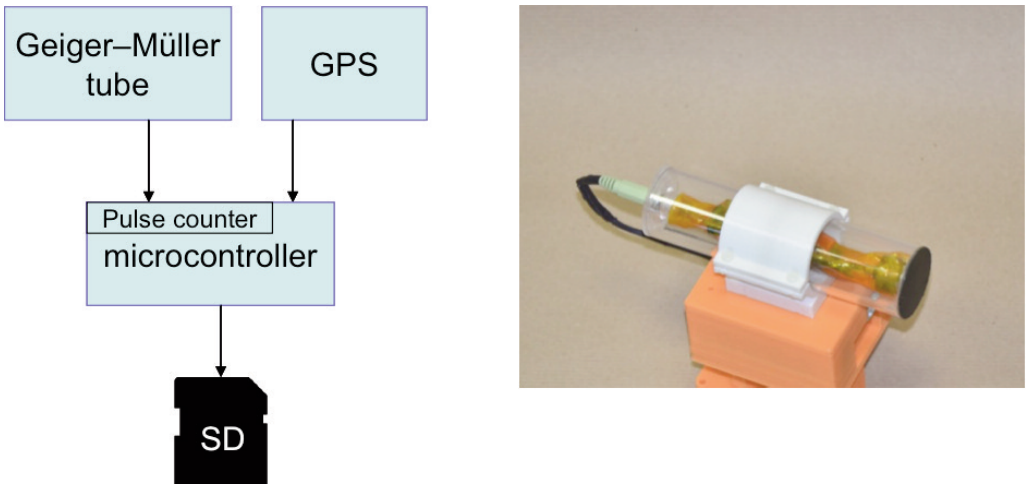

Fig. 6 I Geiger counter. This autonomous device records the number of tube discharge for every position and stores them in a SD card

The device described is a lightweight counter, powered by the drone battery, designed to count the number of discharges in the Geiger-Müller tube and store them in a SD memory card, tagging them with position ad time information from a GPS receiver (Fig. 6).

Gas Sensor

This device (Fig. 7) uses an electrochemical sensor and a NDIR sensor to detect CH_4 and CO_2. A built-in GPS and a recording system allow recording gas concentration during the flight. Every measurement is tagged with GPS time and position. The gas is forced into the detector by a fan.

Data are stored in plain text into a SD memory card. Figure 8 shows the calibration curves, obtained comparing the device with a reference instrument.

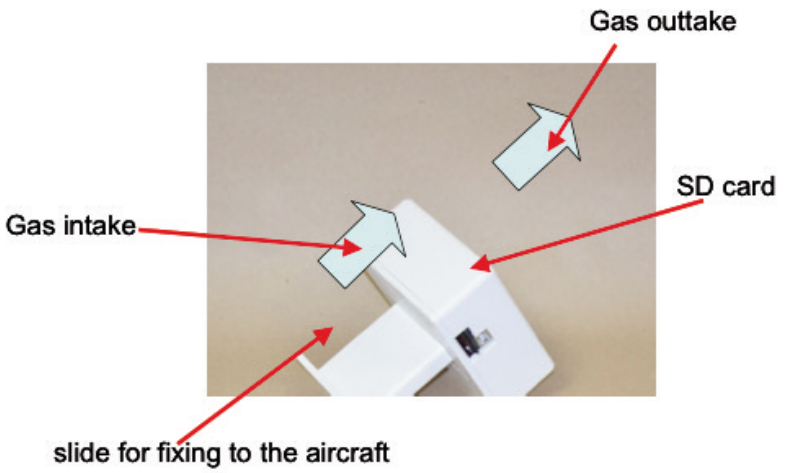

Fig. 7 I The airborne gas meter. The device requires only the power to start operating. It continuously appends measurements to the SD card, tagging them with time and position.

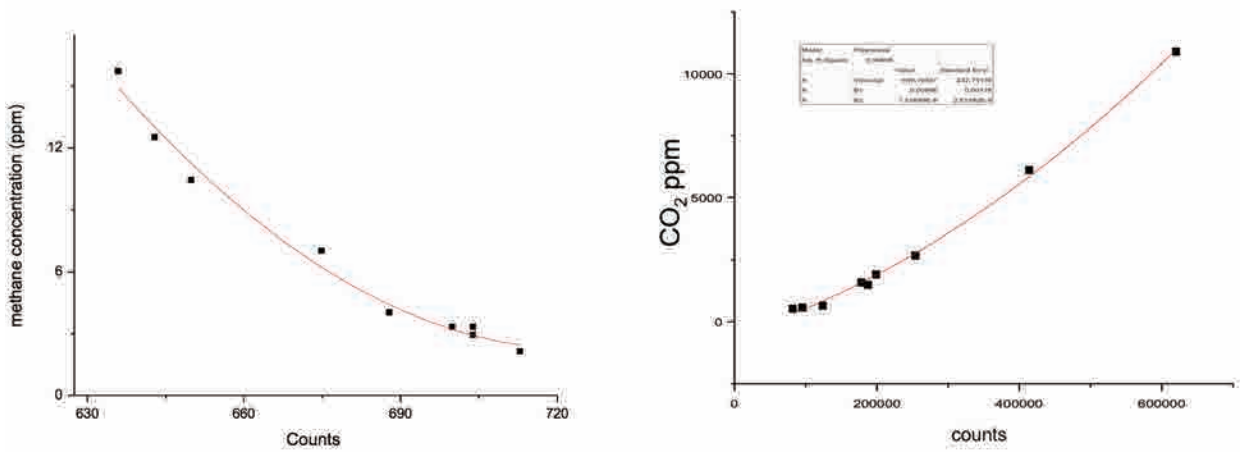

Fig. 8 I Calibration curves obtained camparing the device with a reference instrument.

Lusi survey by drone

All the equipment developed for drone use have been used in Indonesia, in the framework of Lusi Lab project (ERC grant n_ 308126), to explore the huge hydrothermal manifestation in East Java, Sidoarjo district, roughly 30 km South Surabaya. The mud emission started in 2006 and caused the evacuation of over 40000 people.

In this mission (May 2015) the LNTS personnel performed photogrammetry, gas and mud sampling, gas concentration measurements and infrared aero photography.

Comparative photogrammetry may be a good tool for estimating the rapid evolution of Lusi Area. Although an extensive set of flight planes was made, (Fig. 9) only one of them has been accomplished because of lack of logistics. Figure 10 shows the orthophoto of the NortEast area. 2500 12 Mpixels photographe have been merged to make this picture.

A thermal survey has also been realized, aimed to study the crater temperature. Unfortunately the high water vapour content makes the radiometric data interpretation very difficult, and the estimated temperature results

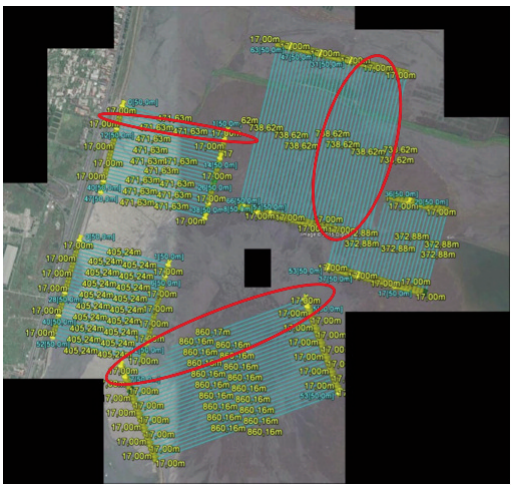

Fig. 9 I The planned photogrammetric missions. Only the circled parts have been performed, and only the photographs of the northern part have been traited

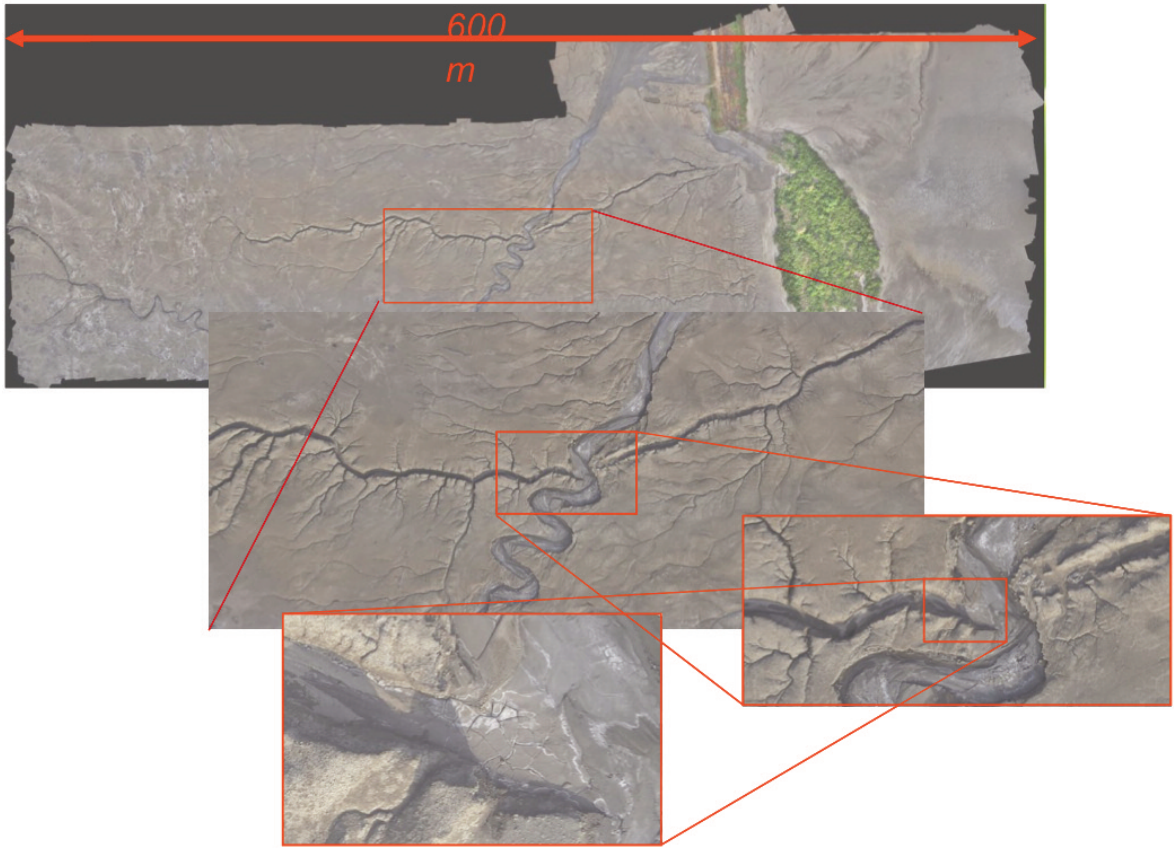

Fig. 10 I A large Lusi orthophoto with a sequence of zoom. This technique allows to see details of a few centimetres on the views of hundreds of meters. This image required 2500 photographs.

lower than the real one. Some contact measurement have been performed using a standard thermometer with built-in datalogger, in the crater proximity, using the automatic winch.

Figure 11 shows a contact temperature diagram (the measured temperature is 91.36°C) and a thermal mosaic of the crater, obtained using a Flir I7 camera flying at 100 m altitude.

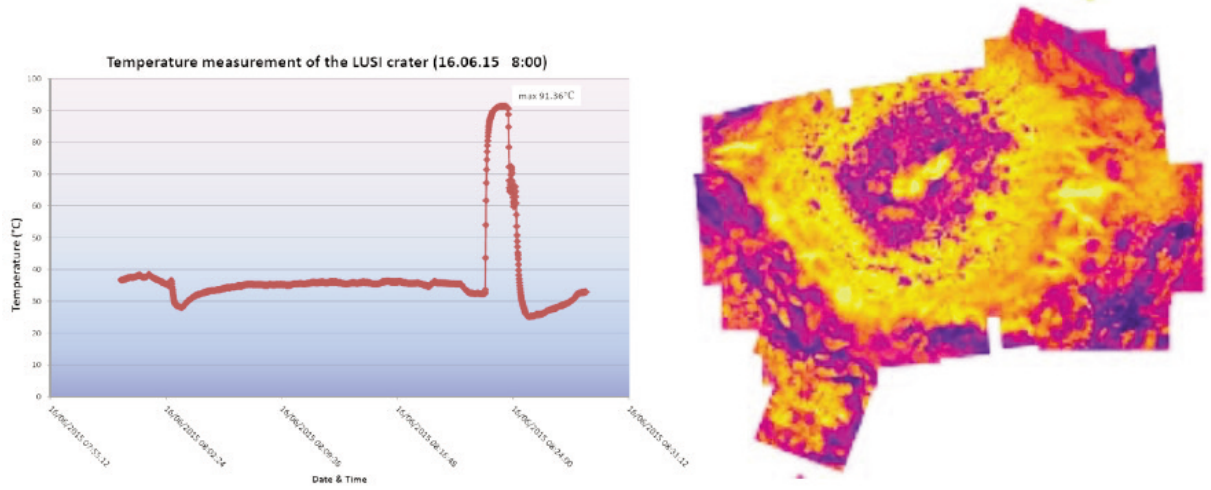

Fig. 11 I Thermal measurement on Lusi. On the left, the result of a measurement using a contact thermometer. During the measurement the drone hovers over the point of interest, operates the automatic winch, and waits for the thermometer to thermalize. Then returns to the base station. On the right, a beautiful thermal view of the crater. Although it is possible to associate a temperature to every pixel, the high water vapour content introduces an error that cannot be compensated using the contact temperature measurements, because of the quick time variation of the temperature concentration.

Multiparametric portable instrument

G. Caramelli

Research Line IT2

This multiparameter portable equipment, is designed to measure and store on a memory SD card the observables listed below :

- Acceleration on three axes (from 3 MEMS capacitive accelerometers);
- Coordinates (from GPS);
- Pressure, pressure variation and infrasound (Resolution 0.012 mbar in the range of 10 to 1200 mbar);
- Magnetic field on three axes (Resolution of 5 milli-gauss in +/- 8 Gauss field);
- Electric field variations;
- Temperature.

All data are tagged with GPS time.

Although the system is not completely assembled yet, every module is working properly, waiting for the definitive assembly. All the components will be included in a single cylindrical container (30 cm height and 13 cm diameter) and powered by Li-ion rechargeable battery. The system can be operated continuously for 5 days.

Fig. 1 I The instrument case, without the electrometer. The electrometer antenna will be installed over the keyboard cover that will be provided for protection in field operation.

The instrument has a modular configuration. Each module by using a microcontroller, receives and processes signals from sensors, and, when required, send measures to Master Board using serial IIC multi-master, multi-slave single-ended protocol (Fig. 2).

The Master Board, placed on the top of the cylinder (Fig. 1), collects data from the ancillary boards, manages the communication with the operators and stores the data on the SD card.

The firmware installed on each board performs linearization and temperature compensation.

The acceleration sensors (Colibrys MS9002) are located on the faces of an aluminum cube in the bottom of the cylinder; the analog signal from sensors is 24 bits digitized and sent to the Master Board.

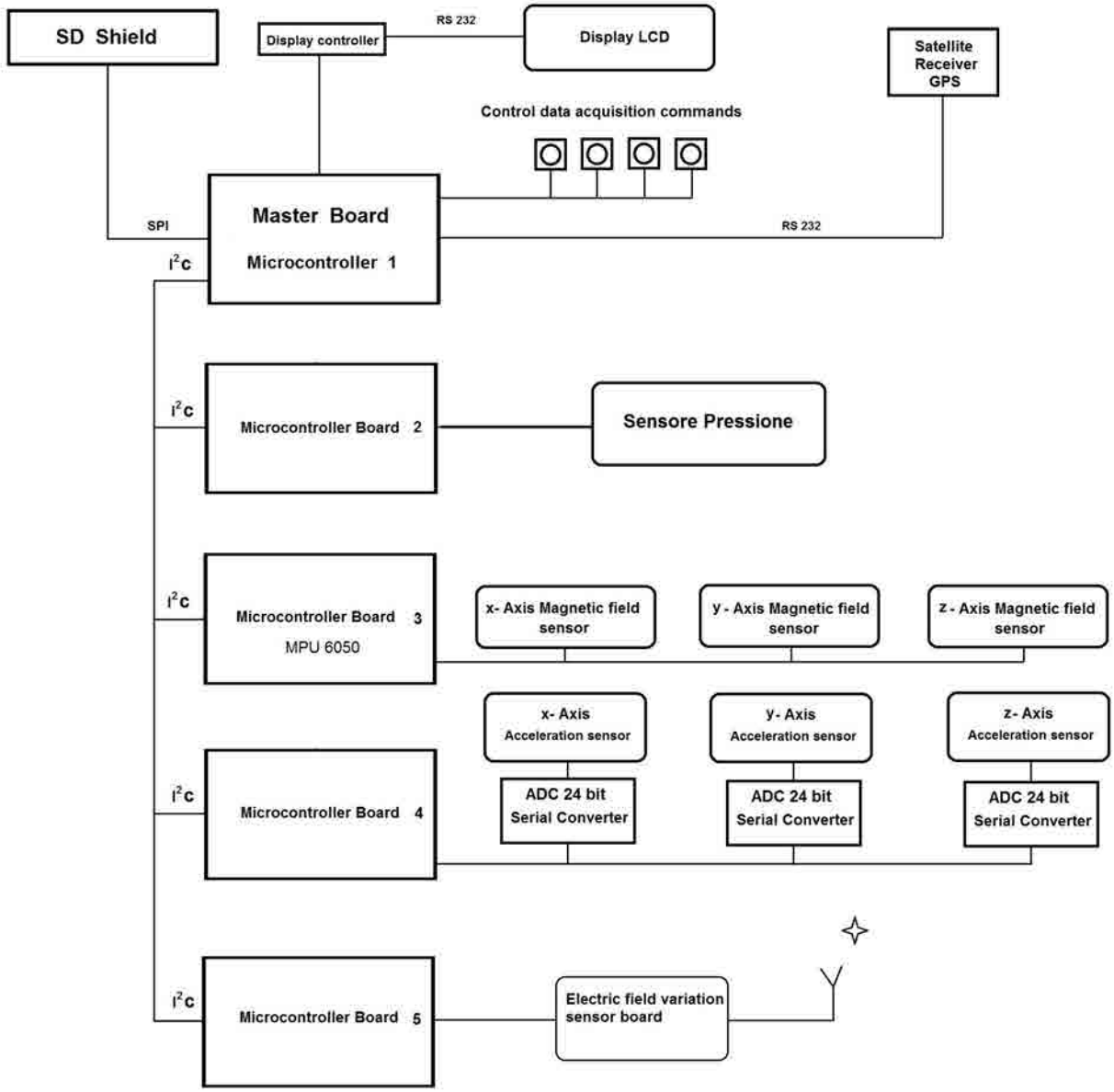

Fig. 2 I Multiparametric instrument block diagram.

Machine shop activity

M. Mari

Research Line IT2

Although it can not be counted as research work, the machine shop work is essential to the conduct of all experimental investigations. Moreover the machine shop is the reference facility for the whole INGV Rome site, and performs several machining on request. Usually the machining average is of 1000 machining per year (from consumable for physics rocks experiments to more complex dedicated parts). Figures 1, 2 and 3 show some realizations of 2015.

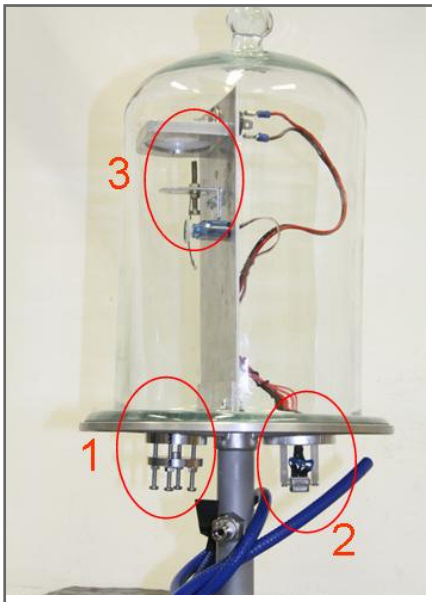

Fig. 1 I Optical thermometer experimental assembly. (1) Optical fiber pass-through. (2) Electrical pass-through. (3) Optical fiber feeding mechanism.

Fig. 2 I Rheometer parts.

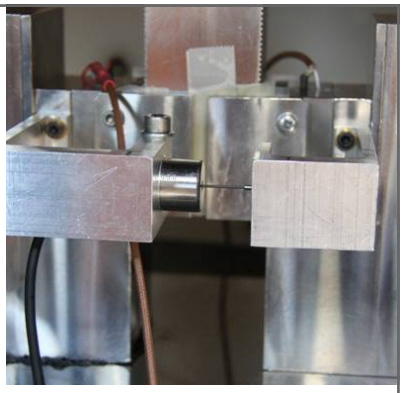

Fig. 3 I BRAVA LVDT assembly.

Realization of an prototype system for the detection of gaseous phases inside to the FESEM specimen chamber

A. Cavallo, M. Nazzari, G. Etiope

Research Line A7

The realization of a prototype system for qualitative and semi-quantitative analysis of the gases produced by the interaction between the electron beam and the sample directly into the specimen chamber of a Scanning Electron Microscope (SEM) has been investigated. In this way in fact a chemical mapping of volatile substances from a sample electronically scanned, would be obtained, integrating the information related to the electronic microanalysis with a chemical mapping of volatile substances. This analysis could be applied to the study of the gases contained in both clathrate form and melt inclusions in rocks or generally solid materials where the combined electronic and heat effect would be able to release them.

The RGA system has been directly installed with flanged coupling on a microscope open port and since the RGA must operate under high vacuum conditions the upgrade of the SEM vacuum system has been performed, replacing two existing diffusive pumps (DPs) with a Turbo Molecular Pump (TMP) and the old rotary pump (RP) necessary for the pre-vacuum with a more powerful dry RP. Moreover, in order to dampen and isolate the mechanical vibrations of TMP a damper was installed. The upgraded vacuum system, in addition to being as mentioned cleaner elimina-

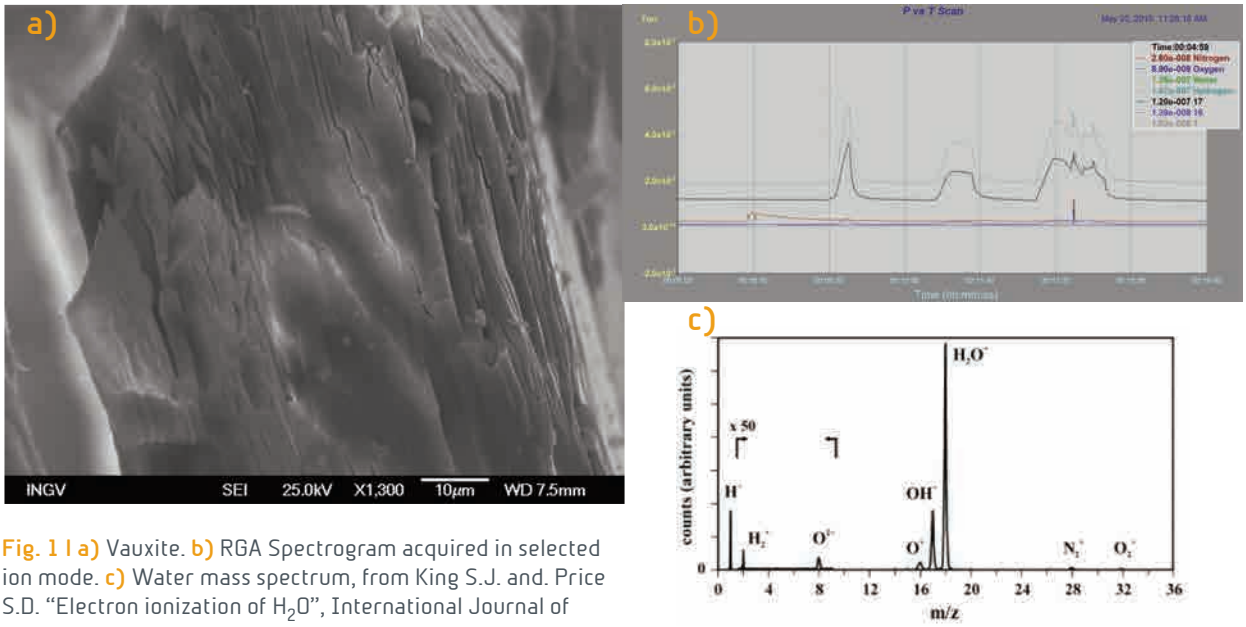

Fig. 1 I a) Vauxite. b) RGA Spectrogram acquired in selected ion mode. c) Water mass spectrum, from King S.J. and. Price S.D. "Electron ionization of H_2O", International Journal of Mass Spectrometry, Volume 277, Issues 1–3, 2008, 84 - 90.

ting possible contaminants during the partial pressure analyses, is much more efficient than the previous one, since it allows the achievement of high values of vacuum in the chamber in times significantly lower.

The RGA volatile analysis system was effectively tested on a vauxite sample, an iron and aluminum phosphate with high water content (28%). Hitting in fact the crystal with the electronic beam, in particular in the mineral discontinuity points (fractures, Fig. 1a) and in conditions of high current (about 130 nA), an instantaneous volatilization of water molecules contained in the mineral was obtained (Fig. 1b), with a sudden increase of the 18, 17, 2 and 1 m/z ratios, all characteristic of the water spectrum (Fig. 1c). The water emission is most likely produced by the heating of the sample induced by the absorbed current, and not due to the sample cracking followed by the liberation of the water molecules, there are not in fact evidence of mineral surface damage.

The system was also tested on rocks (serpentinite and chromites) that showed a good methane content (almost 1% by means of grinding experiments). In this case, however, no evidence of methane release by means of the mass spectrometer has been shown, probably because the thermal effect, tunable through the beam current density (diameter and Ampere) and also depending on the electrical and thermal conductivity of the analyzed sample, is not enough to liberate methane from rocks.

Audio amplifier

G. Romeo

Research Line IT2

An audio amplifier may appear atypical in the LNTS activity. Let's explain why LNTS built and patented (Italian patent application n. 102015000071865) an audio amplifier. LNTS has an active cooperation with the cosmology group of La Sapienza (G31) , and is effective in realizing attitude control systems prototypes and teaching the principles of them. The actuator of an ACS is usually a brushed motor, and its best control may be obtained operating on a well known motor model, that allows a sensorless evaluation of the motor position. If we consider a loudspeaker as a linear motor we may use the same technique developed for controlling the ACS motors to control a loudspeaker. Obviously this requires to specialize the amplifier to match the chosen loudspeaker. The amplifier we patented provides a simple way to tune the amplifier to the chosen loudspeaker using only two parameters. The organoleptic test of the amplifier demonstrated the goodness of the principle. Fig. 1 shows the effect of the changing in the loudspeaker's membrane position when the tuning parameters change.

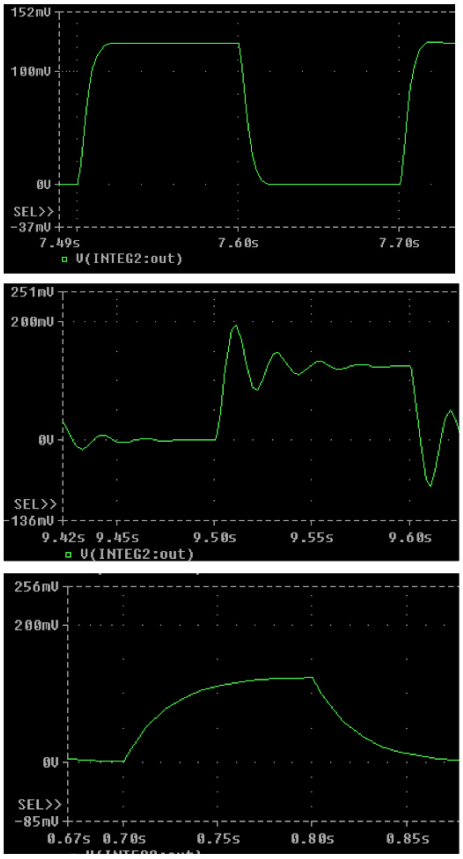

Perfectly matched loudspeaker

Unmatched loudspeaker. Overshoots are caused by the free oscillation of the loudspeaker membrane

Unmatched loudspeaker. The low-pass effect is caused by the excessive damping operated mechanically by the membrane and electrically by the voice coil.

Fig. 1 I Effect of the amplifier's matching parameter on the loudspeaker's membrane position (squarewave stimulus). It exist a value that allows (upper diagram) the best response, overshooting (middle diagram) or overdamping (lower diagram).

Airborne multi-gas analyzer

G. Spinelli, G. Romeo

Research Line A7

A gas sensor is used to detect the presence of a specific gas in an area. It can be used as the main part of a control system within a safety system to detect a gas leak (that can even be harmful to organic life) and automatically shut down the process. A gas sensor can also be used to simply measure the concentration of a substance in the air. In this case it is also possible make use of more sensors together in order to get a detailed analysis of the air.

INGV makes use of unmanned aerial vehicles, commonly known as drones, to perform its public activities, among which we mention volcanic, risk areas and natural disaster monitoring. For analyzing the air during these activities we have assembled a board (Fig. 1) with sensors for the detection of hydrogen, ammonia, hydrogen sulfide, sulfur dioxide, carbon monoxide, carbon dioxide, methane, isobutene, propane, butane, volatile organic compound, vapors of organic solvents and volatile vapors. The raw values measured by the above sensors are read by a microcontroller board (Arduino Mega) and stored on a SD Card. These measurements are saved together with the temperature

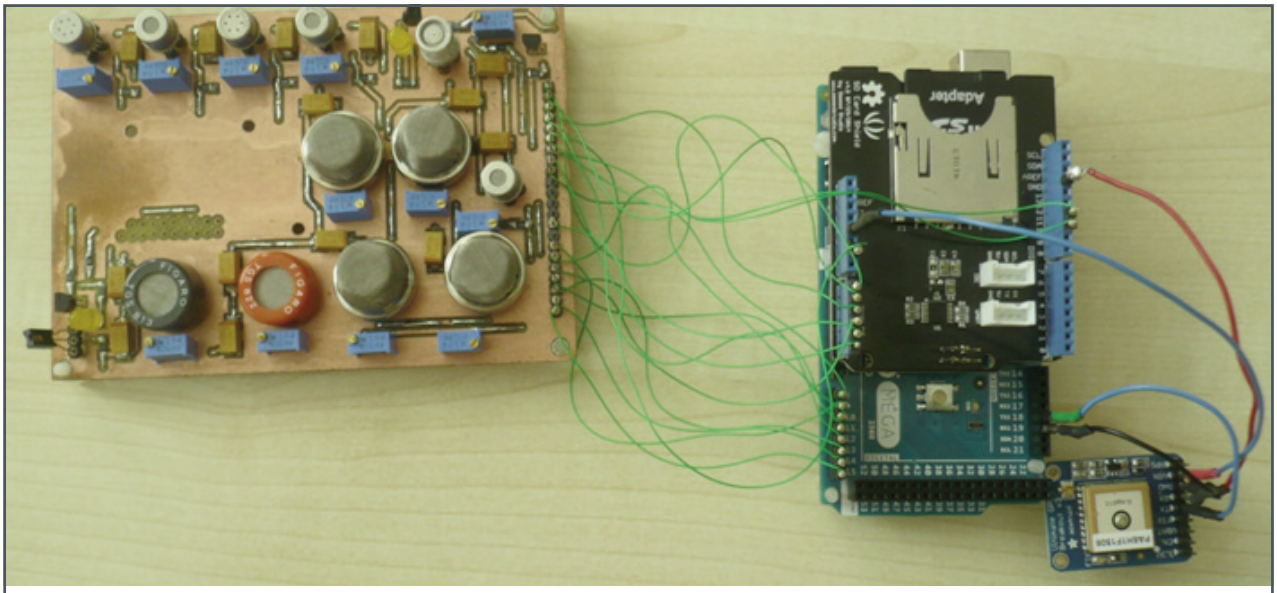

Fig. 1 I On the left: the board with the sensors. On the right: the datalogging board with GPS

and the pressure given by a barometric pressure sensor, with the humidity given by a related sensor and with the position given by a GPS module.

The main challange of our airborne multi-gas analyzer is to combine several different sensors in order to provide a sufficiently accurate measurement. It will be achieved by using the artificial neural networks. ANNs are a family of models inspired by biological neural networks and are used to estimate or approximate functions that can depend

on a large number of inputs and are generally unknown. ANNs are generally presented as a system of interconnected "neurons" which exchange messages between each other. The connections have numeric weights that can be tuned based on the experience, we refer to this as calibration phase, making neural nets adaptive to inputs and capable of learnig. The figure 2 shows the board inside a glass jar during the calibration phase.

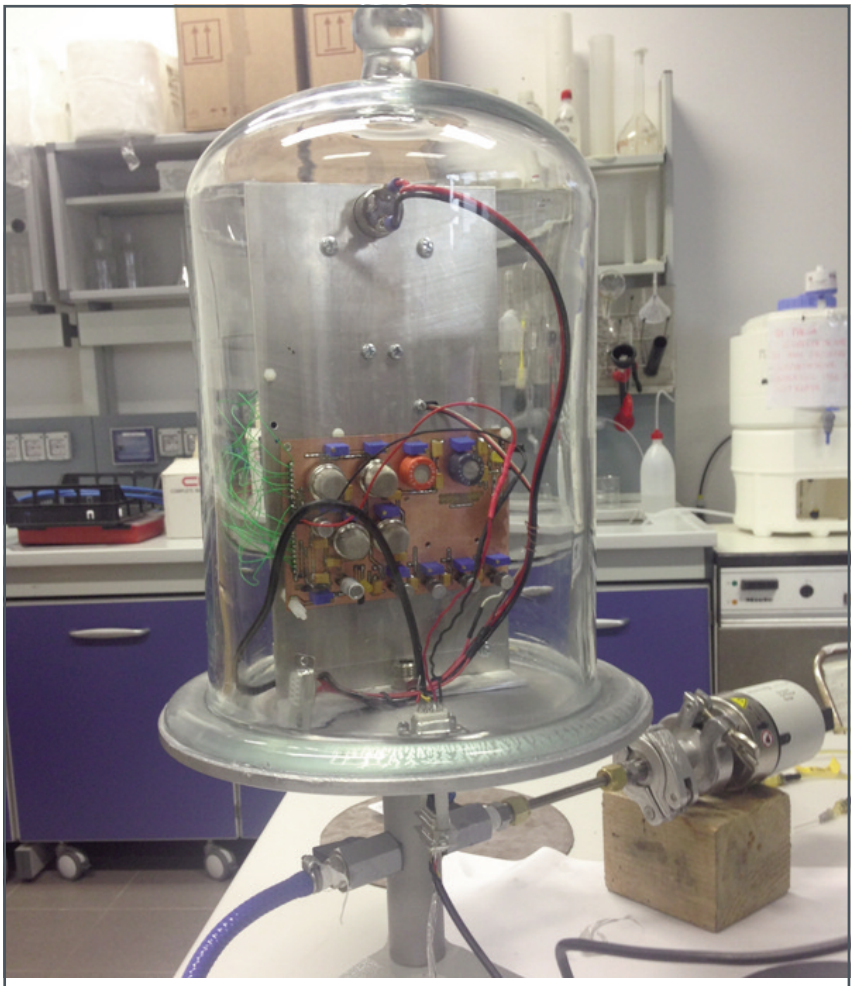

Fig. 2 I The board inside a glass jar provided for sensor calibration.

Optical fiber interferometer

G. Urbini, A. Zirizzotti

Research Line IT2

This work is based on the controversial research of Prof. Reginald Cahill, regarding the gravitational waves detected by means of optical-fiber interferometers (http://www.flinders.edu.au/) (Cahill R., 2006; Cahill R. & Stokes F., 2008), we are trying to reproduce his experimental results. At INGV of Rome (LNTS and Environmental Geophysics Laboratory), we assembled two optical-fiber interferometers, Michelson and Morley type.

In September 2015, one of the two interferometers was installed in Preturo (L'Aquila), the other one remained in Rome. We can reach both the interferometers through internet connection to display data or transfer files.

Of the outmost importance is the synchronization of the two time-bases (GPS time) to search forcoincident signals.

In figure 1 you can see two graphs of the photodiode amplifier output voltage for a period of 24 hours.

The data are acquired at ten samples per second. In 19 February, the interferometer was in the air as the day 27 the interferometer was immersed in water for a passive, short-time, thermostabilization. From the temperature graph (blue line) you notice, actually, a temperature range drop for that day.

From the graph of the interferometer amplitude signal (red line), you notice immediately different behaviors during the day, with oscillations at different frequencies that we will try to investigate in the time with spectral techniques, single station noise analysis and temporal correlations to search concurrence between the two stations.

As regards vibration sensitivity, we haven't tried to cushion the interferometer with mechanical filters because we will try to inquire into correlations with various intensity seismic events, making use of the interferometer as a seismograph.

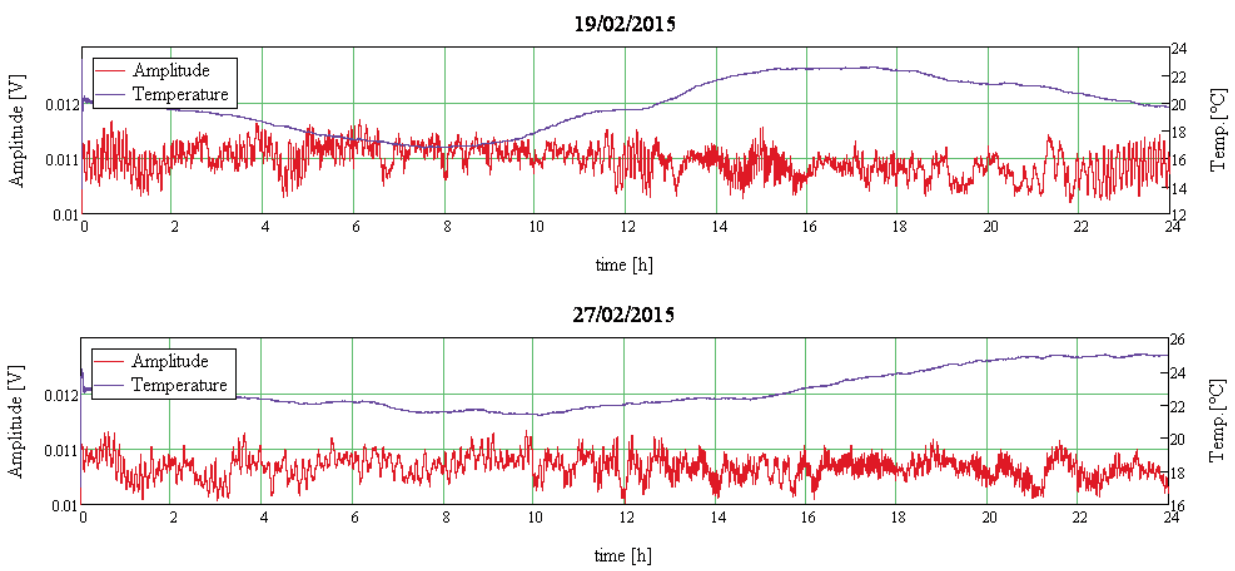

Fig. 1 I Two days of data from the interferometer.

A peculiarity of this interferometer would be its capability to detect gravitational waves (the A. Einstein Relativity Theory pointed out the existence of these waves).

In this way, any signal that can produce gravitational waves will be detected in both the devices at the same time and it will be able to be pointed out through the research of coincident events.

On the contrary, local noises not-correlated in the two sites won't be take into account. After the realization and characterization phases of the instruments, there will be a long period of data acquisition and analysis in the two selected sites (Roma and L'Aquila). It will be very important the instrument operation continuity. It will be guaranteed from the INGV laboratory staff. Data analysis will allow to check the instrument operation, and, if necessary, make improvements. They will be detected and tested all possible new uses of this very sensitive instrument, in parallel with the data analysis phase.

9I SEMINARS and TEACHING

Seminars

Collettini C. I Using BRAVA for the rock physics course at the master of Geo-resources in Sapienza University I **Sapienza Università di Roma** I Roma, Italy I Second semester 2015

Di Toro G. I A close look at the earthquake engine I School of Earth and Environmental Sciences I **Leeds University** I Leeds, UK I 4 Dicembre 2015

Di Toro G. I Il motore dei terremoti visto da vicino I Distinguished Lectures della Società Geologica Italiana, Ciclo di seminari 2015-2016 I **Università di Perugia** I Perugia, Italia I 25 Novembre 2015

Di Toro G. I A close look at the earthquake engine I Keynote Lecture, 2015 Centre of Research in Earth Sciences post-graduate meeting I **Plymouth University** I Plymouth, UK I 18 Novembre 2015

Di Toro G. I Il motore dei terremoti visto da vicino I Distinguished Lectures della Società Geologica Italiana, Ciclo di seminari 2015-2016 I **Università di Torino** I Torino, Italia I 28 Ottobre 2015

Gaudin D. I High speed imaging of Stromboli activity: implications for the mechanism of explosions and vent conditions I **USGS Hawaiian Volcano Observatory (HVO)** I Hawaii, USA I 6 December 2015

Mollo S. I La petrologia sperimentale al servizio dello studio dei vulcani attivi italiani I **Università degli Studi di Ferrara** I Ferrara, Italia I 28 Maggio 2015

Mollo S. I Mineral-melt disequilibrium during rapid cooling and crystal growth: Implications for magma dynamics I **University of Vienna** I Vienna, Austria I 23 Marzo 2015

Romeo G. I Controllo di assetto per payload stratosferici I **Sapienza Università di Roma** I Roma, Italia I 24-26 Novembre 2015

Taddeucci J. I Volcanic eruption styles: lights and shadows; Eruption forces and dynamics; Integrated approaches to an eruption; Eruption experiments I **Short Course on Magmas, Eruptions and Risks, Università degli Studi di Perugia** I Perugia, Italia I 25 Marzo 2015

Taddeucci J. I Volcano in Slo-mo: What High Speed Cameras tell us about Lava Lakes and Explosions I **Hawaii Volcanoes National Park** I Hawaii, USA I 8 December 2015

Taddeucci J. I Fine analysis of fines: a closer look at volcanic ash particles I **1st VERTIGO ITN Summer School, Tenerife** I Tenerife I 12 Marzo 2015

Training

1. **Aretusini S.** I Frictional processes of clay-rich gouges in megathrust and landslide decollement environments I **Supervisors:** Di Toro G. - University of Manchester, Manchester, UK I Spagnuolo E. - INGV Roma1
2. **Demurtas M.** I Quantification of the geometrical complexity of seismogenic fault zones I **Supervisors:** Di Toro G. - University of Manchester, Manchester, UK I Massironi M. - Università degli Studi di Padova, Padova, Italy I Storti F. - Università degli Studi di Parma, Parma, Italy
3. **Di Stefano G.** I PhD I Sviluppo di un prototipo di macchina per lo studio della meccanica delle rocce e caratterizzazione delle proprietà fisiche di faglie sperimentali mediante onde I **Supervisors:** Collettini C., - Sapienza Università di Roma I Romeo, G. - INGV Roma1 I Scarlato, P. - INGV Roma1
4. **Forni F.** I PhD I Caldera collapses and evolutionary trends: the case of Phlegraean Fields volcanic system I **Supervisors:** Bachman O. – ETH Zurigo I De Astis G. - INGV Roma1

5. **Giorgetti C.** | **PhD** | Caratterizzazione strutturale e meccanica in faglie in misture di carbonati e fillosilicati | **Supervisors:** Collettini C. - Sapienza Università di Roma

6. **Salvatore V.** | **PhD** | Dinamiche di eruzioni stromboliane attraverso modellazione analogica, video di monitoraggio e immagini ad alta velocità | **Supervisors:** Palladino D.M. - Sapienza Universita di Roma | Taddeucci J. - INGV – Roma1

7. **Tecchiato V.** | **PhD** | Il ruolo dei mush cristallini nei processi di differenziazione dei magmi calcalcalini: caratteri giaciturali, petrografici, geochimici e modellistica sperimentale | **Supervisors:** Gaeta M. - Sapienza Università di Roma | Mollo S. - INGV Roma1

8. **Tournigand P. Y.** | **PhD** | Field-based study of volcanic ash via visible and thermal high-speed imaging of explosive eruptions | **Supervisors:** Palladino D.M. - Sapienza Universita di Roma | Taddeucci J. - INGV – Roma1

Graduate Thesis

1. **Bardelli L.** | Master Thesis: The role of talc in the frictional properties of carbonate-bearing faults | **Supervisors:** Collettini C. – Sapienza Università di Roma | Carpenter B.M. – INGV Roma1

2. **D'Alessandro A.** | BsC Thesis: Caratterizzazione di rocce di faglia sperimentali in calcite ad alta deformazione | **Supervisors:** Collettini C. – Sapienza Università di Roma | Tesei T. – INGV Roma1

3. **Diamanti J.** | Master Thesis: Sistema di controllo d'assetto per palloni stratosferici | **Supervisors:** Masi S. Sapienza Università di Roma | Romeo G. - INGV Roma1

4. **Dominijanni S.** | Grauate Thesis: Parametrization of Strombolian eruptions via video analysis | **Supervisors:** Palladino D.M. - Sapienza Università di Roma | Taddeucci J. - INGV Roma1

5. **Edwards M.** | Master Thesis: Bubble bursts in mud: White Island observations and insights from laboratory experiments | **Supervisors:** Kennedy B. – University of Canterbury | Taddeucci J. - INGV Roma1

6. **Giacomel P.** | Master Thesis: Frictional instabilities of basalts and calcite-built marbles in the presence of pressurized H_2O and CO_2 fluids | **Supervisors:** Di Toro G. - University of Manchester, Manchester, UK | Marzoli A. - Università degli Studi di Padova, Padova, Italy | Spagnuolo E., - INGV Roma1

7. **Loemba Bouity T.** | Stage: Video analysis for the reconstruction of bomb trajectory | **Supervisors:** Palladino D.M. - Sapienza Università di Roma | Taddeucci J. - INGV Roma1

8. **Manniello M.A** | Master Thesis: Studio sperimentale dell'emissione radon da materiali geologici a temperature subvulcaniche | **Supervisors:** Tuccimei P. – Università degli Studi di Roma Tre | Mollo S. – INGV Roma1

9. **Mounombo Koumba J.R.G.** | Stage: Video analysis for the reconstruction of bomb trajectory | **Supervisors:** Palladino D.M. - Sapienza Università di Roma | Taddeucci J. - INGV Roma1

10. **Spurio A.** | Stage: 3-D reconstruction of bomb trajectory from video analysis | **Supervisors:** Palladino D.M. - Sapienza Università di Roma | Taddeucci J. - INGV Roma1

10| VISITING SCIENTISTS

Deegan F.M. | **University of Uppsala, Sweden** | November, December

Becchio R. | **Università di Salta – Argentina** | September

Li-W. Kuo | **National Central University | Taoyuan City (Taiwan)** | January-May

Vannucchi P. | **Royal Holloway, London** | July

Cappa F. | **University of Nice Sophia Antipolis, France** | November

Marone C. | **Penn State University, USA** | January-June

Violay M. | **Swiss Institute of Technology, Lausanne** | October

Seminars

Giacomoni P.P. | Università degli Studi di Ferrara, Ferrara, Italy | **Reconstruction of magmatic conditions driving eruptions at Mt. Etna** | 24 November

Research activity

Lipparini L. | **Università Sapienza, Roma, Italy** | September

Rizzo M. | **Università degli Studi di Ferrara, Ferrara, Italy** | September

European Geoscience Union (EGU) | Vienna, Austria | 12 -15 April 2015

Allard P., Aiuppa A., Beauducel F., Calabrese S., Di Napoli R., Crispi O., Gaudin D., Parello F., Hammouya G., Tamburello G.
Steam and gas emission rates from La Soufrière of Guadeloupe (Antilles arc): implications for the magmatic supply degassing during unrest

Aretusini S., Mittempergher S., Gualtieri A., Di Toro G.
Frictional processes in smectite-rich gouges sheared at slow to high slip rates

Bistacchi A., Mittempergher S., Di Toro G., Garofalo P.
Fault zone hydraulic properties provide an independent estimate of coseismic fracturing at 8 km depth (Gole Larghe Fault Zone, Italian Southern Alps)

Carpenter B.M., Di Stefano G., Collettini C.
The Influence of Calcite on The Mechanical Behavior of Quartz-Bearing Gouge

Collettini C., Scuderi M.M.
The role of fluid pressure in frictional stability and earthquake triggering: insights from laboratory experiments

Del Bello E., Andronico D., Vu Duc A., Cristaldi A., Kueppers U., Ricci T., Scarlato P., Scollo S., Taddeucci J.
Settling dynamics of basaltic (Etna) and trachytic (Laacher See) ash particles: insight from laboratory high speed imaging

Demurtas M., Fondriest M., Clemenzi L., Balsamo F., Storti F., Di Toro G.,
Architectural and microstructural characterization of a seismogenic normal fault in dolostones (Central Apennines, Italy)

Edwards M., Kennedy B., Jolly A., Scheu B., Taddeucci J., Jousset P., Schmid D.
Temporal evolution of micro-eruptions within the crater lake of White Island (Whakaari) during January/February 2013

Fondriest M., Doan M.L., Di Toro, G., Fusseis F.
Experimental constraints on the origin of in-situ shattered dolostones

Marone C., Scuderi M.M., Leeman J., Saffer D., Collettini C., Johnson. P.
Slow Earthquakes and the Mechanics of Slow Stick-Slip

Mitchell T., Smith S.A.F., Anders M., Di Toro G., Nielsen S., Cavallo A., Beard D.A.
Catastrophic emplacement of giant landslides aided by thermal decomposition: Heart Mountain, Wyoming

Platt J., Proctor B., Mitchell T.M., Hirth G., Goldsby D.L., Di Toro G., Beeler N.M., Tullis T.E.
The role of gouge and temperature on flash heating and its hysteresis

Scuderi M.M., Marone C., Tinti E., Scognamiglio L., Di Stefano G., Collettini C.
Mechanical heterogeneity and its transient evolution along fault zones

Taddeucci J., Scarlato P., Del Bello E., Gaudin D
A kilohertz approach to Strombolian-style eruptions

Tournigand P. Y., Taddeucci J., Scarlato P., Gaudin D., Del Bello E.
Field-based study of volcanic ash via visible and thermal high-speed imaging of explosive eruptions

Trippetta F., Mollo S., Carpenter B.M., Collettini C.
Physical and Transport Properties of the carbonate-bearing faults: experimental insights from the Monte Maggio Fault zone (Central Italy)

Violay M., Di Toro G., Spagnuolo E., Nielsen S., Burg J-P.
INVITED Experimental evidence of thermo-mechanical pressurization of faults during earthquakes

35th EARSeL Symposium – European Remote Sensing: Progress, Challenges and Opportunities | Stockholm, Sweden | June 15-18, 2015

Amici S., Pieri D., Husein A., Mazzini A., Romeo G.
Application of thermal remote sensing to the Indonesian Lusi eruption

26th International Union of Geodesy and Geophysics (IUGG) | Prague, Czech Republic | 22 June – 2 July

Del Bello E., Vu Duc A., Cristaldi A., Andronico D.,Kueppers U., Ricci T., Scarlato P., Scollo S., Taddeucci J.
Settling dynamics of basaltic (Etna) and trachytic (Laacher See) ash particles: insight from laboratory high speed imaging

de' Michieli Vitturi M., Neri A., Del Bello E., Scarlato P., Taddeucci J.
PlumeMoM: A moments-based computational plume model with ash aggregation

Gaudin D., Taddeucci J., Scarlato P.
The precursors of Strombolian explosions and how they betray the shallow conduit characteristics

Giacomoni P.P., Coltorti M., Ferlito C., Mollo S.
Thermobarometric constraints of clinopyroxene and plagioclase textural and chemical zoning: A tool to investigate the feeding system of Mt. Etna volcano

Scarlato P., Del Bello E., Ricci T., Taddeucci J.
Dynamics of strombolian eruptions at Batu Tara volcano (Indonesia)

Scarlato P., Del Bello E., Ricci T., Taddeucci J.
The precursors of Strombolian explosions and how they betray the shallow conduit characteristics

Taddeucci J., Del Bello E., Scarlato P., Ricci T., Andronico D., Kueppers U., Cananta A., Sesterhenn J.
The hidden secrets of a Strombolian clockwork: coupled high speed imaging and seismoacoustic recordings of explosions at Etna

Tournigand P. Y., Taddeucci J., Scarlato P., Gaudin D., Del Bello E.
Characterization of volcanic plume dynamics using high-speed imagery

MED-SUV 2nd Year Meeting | Naples, Italy | 6-9 July

Del Bello E., Andronico D., Cristaldi A., Kueppers U., Ricci T., Scarlato P., Scollo S., Taddeucci J., Vu Duc A.
Settling dynamics of natural ash particles: insight from laboratory high speed imaging

Privitera E., Cannata A., Del Bello E., Pena Fernandez J.J., Ricci T., Scarlato P., Sciotto M., Sesterhenn J., Taddeucci J.
Multi-parametric characterization of multivent strombolian activity

Goldschmidt | Prague, Czech Republic | 16 -21 August

De Cristofaro S., Perinelli C., Gaeta M., Mollo S., Palladino D., Armienti P., Scarlato P.
The Control of Water on the Crystallization of Magmas at Mt. Etna Volcano (Sicily, Italy)

Giacomoni P.P., Coltorti M., Ferlito C., Mollo S.
Reconstructing the Magmatic Conditions Driving Eruptions at Mt. Etna

Laeger K., Andronico D., Scarlato P., Cimarelli C., Del Bello E., Freda C., Misiti V., Taddeucci J., Perugini D.
Determination of end-member proportions for syn-eruptive magma mixing of 2010 Eyjafjalljokull eruption by high resolution geochemical mapping of volcanic ash

Misiti V., Elbrecht A.L., Davis M., Iezzi G., Vetere F., Cavallo A., Mollo S.
Glass stability of natural silicate compounds from igneous rocks

Scolamacchia T., Misiti V., Del Gaudio P., Cavallo A., Scarlato P.
On the role of sulfur in explaining different degassing systems

Tecchiato V., Gaeta M., Mollo S., Perinelli C., Scarlato P.
High Porphyritic Calcalkaline Basalts from the Cenozoic Capo Marargiu Volcanic District (Sardinia, Italy)

SIMP-AIV-SoGeI-SGI | Firenze | 2-4 September

Del Vecchio A., Poe B.T., Misiti V., Cestelli Guidi M.
Hydrogen diffusion in nominally anhydrous minerals: implications for mass and charge transport

Workshop "Modeling Fault Friction" | Utrecht, The Netherlands | September

Di Toro G.
Fault processes in carbonate-bearing rocks at seismic deformation conditions

11th EURO-conference on Rock Physics and Geomechanics | Ambleside, UK | September

Giacomel P., Spagnuolo E., Marzoli A., Nazzari M., Youbi N., Di Toro G.
Frictional instabilities and mineral carbonation of basalts triggered by injection of pressurized H_2O- and CO_2-rich fluids

Marone C., Leeman J. R., Scuderi M. M., Saffer D. M., Collettini C., Johnson P.
Slow Earthquakes and The Spectrum of Fault Slip Behaviors

Nielsen S., Spagnuolo E., Violay M., Di Toro G.
Dynamic weakening and fracture energy in experiments at seismic conditions

Tesei T., Carpenter B.M., Amir S., Collettini C.
Friction of principal slip surfaces in limestone: preliminary data from large-scale biaxial experiments

FIST 2015 Meeting della Federazione Italiana di Scienze della Terra | Firenze, Italy | September

Aretusini S., Mittempergher S., Gualtieri A., Di Toro G.
Frictional processes in smectite-rich gouges sheared at low to high slip rates

The Geology of Geomechanics | Burlington House, London | October

Collettini C., Scuderi M.M.
The role of fluid pressure in frictional stability and earthquake triggering: insights from rock deformation experiments

Giorgetti C., Carpenter B.M., Scuderi M.M., Tesei T., Barchi M.R., Collettini C.
The role of mechanical anisotropy in controlling fault trajectories within multilayered carbonate and clay-rich rocks

FISMAT 2015 Italian Conference on Condensed Matter Physics | Palermo (Italy) | October

Di Toro G.
INVITED Friction, phase changes and earthquake physics

AGU Fall Meeting 2015 | San Francisco (USA) | 14-18 December 2015

Alder S., Smith S. A. F., Tesei T., Collettini C.
Frictional controls on high-angle reverse faulting during compressional basin inversion

Aretusini S., Mittempergher S., Spagnuolo E., Di Toro G., Gualtieri A., Plumper O.
Amorphization and Frictional Processes in Smectite-Quartz Gouge Mixtures Sheared from Sub-seismic to Seismic Slip Rates

Capponi A., Taddeucci J., Scarlato P., Palladino D.M.
A Mouthful of Dirt: Feedbacks Between the Presence and Nature of In-Vent Debris and the Dynamics of Strombolian Explosions

Carpenter B.M., Viti C., Collettini C.
Physicochemical processes and the evolution of strength in calcite fault gouge at room temperature

Collettini C., Scuderi M.M.
The Role of Fluid Pressure in Earthquake Triggering: Insights from an Experimental Study of Frictional Stability of Carbonates

De Astis G., Baez W., Bardelli L., Becchio R., Giordano G., Lucci F., Rossetti F., Viramonte J.
Genesis and Eruptive Dynamics of the Garnet-Bearing Rhyolites from the Ramadas Volcanic Centre (Altiplano-Puna Plateau, Central Andes, Argentina)

Del Bello E., Taddeucci J., De' Michieli Vitturi M., Scarlato P., Andronico D., Scollo S., Kueppers U.
Effect of particle volume fraction on the settling velocity of volcanic ash particles: implications for ash dispersion models

Di Toro, G., Spagnuolo E., Violay M., Rempe M., Smith S., Nielsen S., Fondriest M., Plumper O.
INVITED "Frictional processes" in carbonate-bearing rocks at seismic deformation conditions

Fondriest M., Doan M-L., Aben F., Fusseis F., Mitchell T., Di Toro G.
Static versus dynamic fracturing in shallow carbonate fault zones

Gaudin D., Taddeucci J., Scarlato P., Del Bello E., Houghton B., Orr T., Andronico D., Kueppers U.
Game of thrown bombs in 3D: using high speed cameras and photogrammetry techniques to reconstruct bomb trajectories at Stromboli (Italy)

Gaudin D., Taddeucci J., Scarlato P., Harris A., Bombrun M., Del Bello E., Orr T.
Precursors and transitions in explosive activity at Stromboli (Aeolian Islands) and implications for shallow vent processes

Houghton B., Orr T., Taddeucci J., Carey R., Del Bello E., Scarlato P., Patrick M.
Vesiculation Processes During Transient and Sustained Explosive Activity at Halema'uma'u Crater, Kīlauea in 2008-2013

Llewellin E.W., Del Bello E., Mathias S., Lane S., James M., Taddeucci J., Capponi A., Scarlato P.
Slugs and Plugs: the Role of Conduit Boundary Conditions in Shaping Strombolian Explosive Activity

Mitrovic I., Tesei T., Colletini C., Grasemann B., Plan B.
Microstructure and frictional properties of sheared calcite speleothems: natural vs. experimental investigation

Passelegue F., Di Toro G., Spagnuolo E., Violay M., Nielsen S., Schubnel A.
High-velocity frictional properties of Westerly granite and the role of thermal cracking on gouge production

Rabinowitz H.S., Savage H.M., Carpenter B.M., Collettini C.
Frictional behavior of carbonate-rich sediments in subduction zones

Rempe M., Mitchell T., Renner J., Smith S., Di Toro G.
The Damage Structure of the Gole Larghe Fault Zone Inferred From Laboratory Measurements and Modeling of Physical and Hydraulic Properties

Rowe C., Lamothe K., Rempe M., Andrews M., Mitchell T., Di Toro G., J. White
Earthquake lubrication and healing explained by amorphous nanosilica

Scarlato P., Del Bello E., Gaudin D., Taddeucci J., Ricci T., Cesaroni C.
Dynamics of Strombolian eruptions at Batu Tara volcano (Indonesia)

Scuderi M.M., Marone C., Tinti E., Di Stefano G., Collettini C.
The full spectrum of fault behavior from slow- to stick-slip: mechanical and acoustic insight on laboratory faults

Spagnuolo E., Nielsen S., Di Toro G., Violay M.
An Empirically-based Steady-state Friction Law and its Implications for Fault Stability

Taddeucci J., Del Bello E., Scarlato P., Ricci T., Andronico D., Kueppers U., Cannata A., Sesterhenn J., Spina L.
Coupled High Speed Imaging and Seismo-Acoustic Recordings of Strombolian Explosions at Etna, July 2014: Implications for Source Processes and Signal Inversions

Tinti E., Scuderi M.M., Scognamiglio L., Di Stefano G., Marone C., Collettini C.
Understanding Vp variation from p-wave coda during laboratory slow-slip

Valentine G., Sottili G., Palladino D., Taddeucci J.
Tephra ring interpretation in light of evolving maar-diatreme concepts: Stracciacappa maar (central Italy)

Vannucchi P., Spagnuolo E., Aretusini S., Di Toro G., Tsutsumi A., Ujiie K., Namiki Y.
INVITED Frictional properties of the biogenic oozes from the CRISP drilling project: possible evidence of past slip-to-the-trench

12| PUBLICATIONS

1. *Blythe L.S., Deegan F.M., Freda C., Jolis E.M., Masotta M., Misiti V., Taddeucci J., Troll V.R.*
CO_2 bubble generation and migration during magma-carbonate interaction
Contribution to Mineralogy and Petrology | 169, 42

2. *Carpenter B.M., Mollo S., Viti C., Collettini C.*
Influence of calcite decarbonation on the frictional behavior of carbonate-bearing gouge: Implications for the instability of volcanic flanks and fault slip
Tectonophysics | | 658, 128-136

3. *De Paola N., Holdsworth R. E., Viti C., Collettini C., Bullock R.*
Can grain size sensitive flow lubricate faults during the initial stages of earthquake propagation?
Earth and Planetary Science Letters | | 431, 48–58

4. *Del Bello E., Lane S., James M., Llewellin E.W., Taddeucci J., Scarlato P., Capponi A.*
Viscous plugging can enhance and modulate explosivity of strombolian eruptions
Earth and Planetary Science Letters | 423, 210-218

5. *Del Bello E., Taddeucci J., Scarlato P., Giacalone E., Cesaroni C.*
Experimental investigation of the aggregation-disaggregation of colliding volcanic ash particles in turbulent, low-humidity suspensions
Geophysical Research Letters | 42, 1068–1075

6. *Del Vecchio A., Poe B.T., Misiti V., Cestelli Guidi M.*
Hydrogen diffusion in nominally anhydrous minerals: implications for mass and charge transport
Rendiconti della Società Geologica Italiana | 35 (2), 254

7. *Fiege A., Vetere F., Iezzi G., Simon A., Holtz F.*
The roles of decompression rate and volatiles (H_2O+Cl±CO_2±S) on crystallization in (trachy-) basaltic magma
Chemical Geology | 411, 310-322

8. *Fondriest M., Aretusini S., Di Toro G., Smith S.A.F.*
Fracturing and rock pulverization along an exhumed seismogenic fault zone in dolostones: the Foiana Fault Zone (Southern Alps, Italy)
Tectonophysics | 654, 56-74

9. *Gaudin D., Finizola A., Delcher E., Beauducel F., Allemand P., Delacourt C., Brothelande E., Peltier A., Di Gangi F.*
Seasonal variations of the heat and steam fluxes in fumarolic zones: the example of the Ty Fault (Guadeloupe, Lesser Antilles)
Journal of Volcanology and Geothermal Research | 302, 273-285

10. *Giorgetti C., Carpenter B.M., Collettini C.*
Frictional behaviour of calcite-talc mixture
Journal of Geophysical Research: Solid Earth | doi. 10.1002/2015JB011970

11. *Gurioli L., Andronico D., Bachelery P., Balcone-Boissard H., Battaglia J., Boudon G., Burgisser A., Burton M.R., Cashman K., Cichy S., Cioni R., Di Muro A., Dominiguez L., Hort M., Kelfoun K., Komorowski J.C., Kueppers U., Le Pennec L., Menand T., Paris R., Pioli L., Pistolesi M., Polacci M., Pompilio M., Ripepe M., Roche O., Rose-Koga E., Rust A., Schiavi F., Scharff L., Sulpizio R., Taddeucci J., Thirdarson T.*
MeMoVolc consensual document: a review of cross-disciplinary approaches to characterizing small explosive magmatic eruptions
Bulletin of Volcanology | 77-,49

12. *Iarocci A., Romeo G., Benedetti P.*
Un sistema di telemetria real-time e di campionamento di gas come payload di un drone
Nota Tecnica INGV | 298

13. *Lacroix B., Tesei T., Collettini C., Oliot E.*
Weakening inside incipient thrust faults
Tectonics | 34, 1396–141, DOI: 10.1002/2014TC003716

14. *Mitchell M.T., Smith S.A.F., Anders M., Di Toro G., Nielsen S., Cavallo A., Beard D.A.*
Catastrophic emplacement of giant landslides aided by thermal decomposition: Heart Mountain, Wyoming
Earth and Planetary Science Letters | 411, 1-9

15. *Mollo S., Giacomoni P.P., Andronico D., Scarlato P.*
Clinopyroxene and titanomagnetite cation redistributions at Mt. Etna volcano (Sicily, Italy): Footprints of the final solidification history of lava fountains and lava flows
Chemical Geology | 406, 45-54

16. *Mollo S., Masotta M., Forni F., Bachmann O., De Astis G., Moore G., Scarlato P.*
A K-feldspar-liquid hygrometer specific to alkaline differentiated magmas
Chemical Geology | 392, 1-8

17. *Mollo S., Giacomoni P.P., Coltorti M., Ferlito C., Iezzi G., Scarlato P.*
Reconstruction of magmatic variables governing recent Etnean eruptions: constraints from mineral chemistry and P-T-fO_2-H_2O modelling
Lithos | 212-215, 311-320

18. *Palladino D.M., Valentine G.A., Sottili G., Taddeucci J.*
Maars to calderas: end-members on a spectrum of explosive volcanic depressions
Frontiers in Earth Sciences | 3: 36

19. *Petracchini L., Antonellini M., Billi A., Scrocca D., Trippetta F., Mollo S.*
Pressure solution inhibition in a limestone-chert composite multilayer: implications for the seismic cycle and fluid flow
Tectonophysics | 646, 96-105

20. *Remitti F., Smith S.A.F., Gualtieri A.F., Mittempergher S., Di Toro G.*
Frictional properties of fault zone gouges from the J-FAST drilling project (Mw 9.0 2011 Tohoku-Oki earthquake)
Geophysical Research Letters | 42, 1-9, doi:10.1002/2015GL063507

21. *Romeo G.*
Verso un multirotore a lunga durata
Nota Tecnica INGV | 307

22. *Smedile A., Civico R., Del Carlo P., Sapia V., De Martini P.M., Pantosti D., Brunori C., Orefice S., Pinzi S., Pucci S.*
Looking for seismites in the Fucino basin: preliminary results from a combined geological-geophysical approach
Proceedings of 6th INQUA-IGCP 567 International Workshop on Active Tectonics, Earthquake Geology and Archaeology, Miscellanea INGV | http://www.ingv.it/editoria/miscellanea/2015/miscellanea27/

23. *Smith S.A.F., Nielsen S., Di Toro G.*
Strain localization and the onset of dynamic weakening in calcite fault gouge
Earth and Planetary Science Letters | 413, 25-36

24. *Spagnuolo E., Plumper O., Violay M., Cavallo A., Di Toro G.*
Fast-moving dislocations trigger flash weakening in carbonates during earthquakes
Nature Scientific Reports | 5:16112, DOI: 10.1038/srep1611

25. *Spina L., Taddeucci J., Cannata A., Gresta S., Lodato L., Privitera E., Scarlato P., Gaeta M., Gaudin D., Palladino D.*
Explosive volcanic activity at Mt. Yasur: a characterization of the acoustic events (9-12th July 2011)
Journal of Volcanology and Geothermal Research | 302, 24-32

26. *Taddeucci J., Alatorre-Ibarguengoitia M.A., Palladino D.M., Scarlato P., Camaldo, C.*
High-speed imaging of Strombolian eruptions: Gas-pyroclast dynamics in initial volcanic jets
Geophysical Research Letters | 42, 6253–6260

27. *Tesei T., Lacroix B., Collettini C.*
Fault strength in thin-skinned tectonic wedges across the smectite-illite transition: Constraints from friction experiments and critical tapers
Geology 43 | 10, 923-926

28. *Tuccimei P., Mollo S., Soligo M., Scarlato P., Castelluccio M.*
Real-time setup to record radon emission during rock deformation: implications for geochemical surveillance
Geoscience Instruments Methods and Data Systems | 4, 111-119

29. *Urbini G.*
Criteri di progetto per la Compatibilità Elettromagnetica "Electromagnetic Compatibility, EMC", "grounding" e "bonding"
Nota Tecnica INGV | 306

30. *Urbini G., Zirizzotti A.*
Stazione interferometrica INGV
Nota Tecnica INGV | 308

31. *Valentine G.A., Sottili G., Palladino D.M., Taddeucci J.*
Tephra ring interpretation in light of evolving maar–diatreme concepts: Stracciacappa maar (central Italy)
Journal of Volcanology and Geothermal Research | 308, 19-29

32. *Vetere F., Iezzi G., Behrens H., Holtz F., Ventura G., Misiti V., Cavallo A., Mollo S., Marcel D.*
Glass forming ability and crystallization behaviour of sub-alkaline silicate melts
Earth Science Review | 150, 25-44

33. *Vetere F., Mollo S., Giacomoni P.P., Iezzi G., Coltorti M., Ferlito C., Holtz F., Perugini D., Scarlato P.*
Experimental constraints on the origin of pahoehoe "cicirara" lavas at Mt. Etna Volcano (Sicily, Italy)
Bulletin of Volcanology | 77, 44

34. *Violay M., Di Toro G., Nielsen S., Spagnuolo E., Burg J.P.*
Thermo-mechanical pressurization of experimental faults in cohesive rocks during seismic slip
Earth and Planetary Science Letters | 429, 1-10

In press

1. *Della Ventura G., Redhammer G.J., Robert J. L., Sergent J., Iezzi G., Cavallo A.*
Synthesis and crystal-chemistry of amphiboles along the join richterite – ferrorichterite: a combined spectroscopic (FTIR Mössbauer), XRPD and microchemical study
The Canadian Mineralogist, in press.

2. *Mollo S., Forni F., Bachmann O., Blundy J.D., De Astis G., Scarlato P.*
Trace element partitioning between clinopyroxene and trachyphonolitic melts: implications for the geochemical evolution of the Campanian Ignimbrite (Campi Flegrei, Italy)
Lithos.

3. *Smith S.A.F., Griffiths J.R., Fondriest M., Di Toro G.*
"Coseismic foliations" in gouge and cataclasite: experimental observations and consequences for interpreting the fault rock record.
Geophysical Monograph Series (American Geophysical Union Special Volume, Washington D.C., USA)

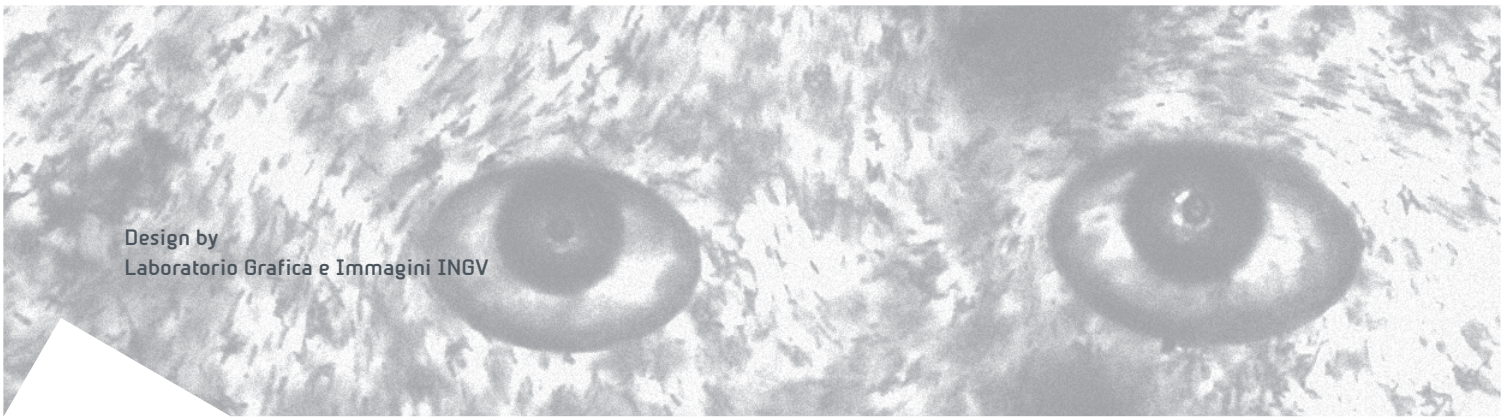

Design by
Laboratorio Grafica e Immagini INGV

Rome, 15 March 2016

Editing by **Valeria Misiti and Matteo Masotta**